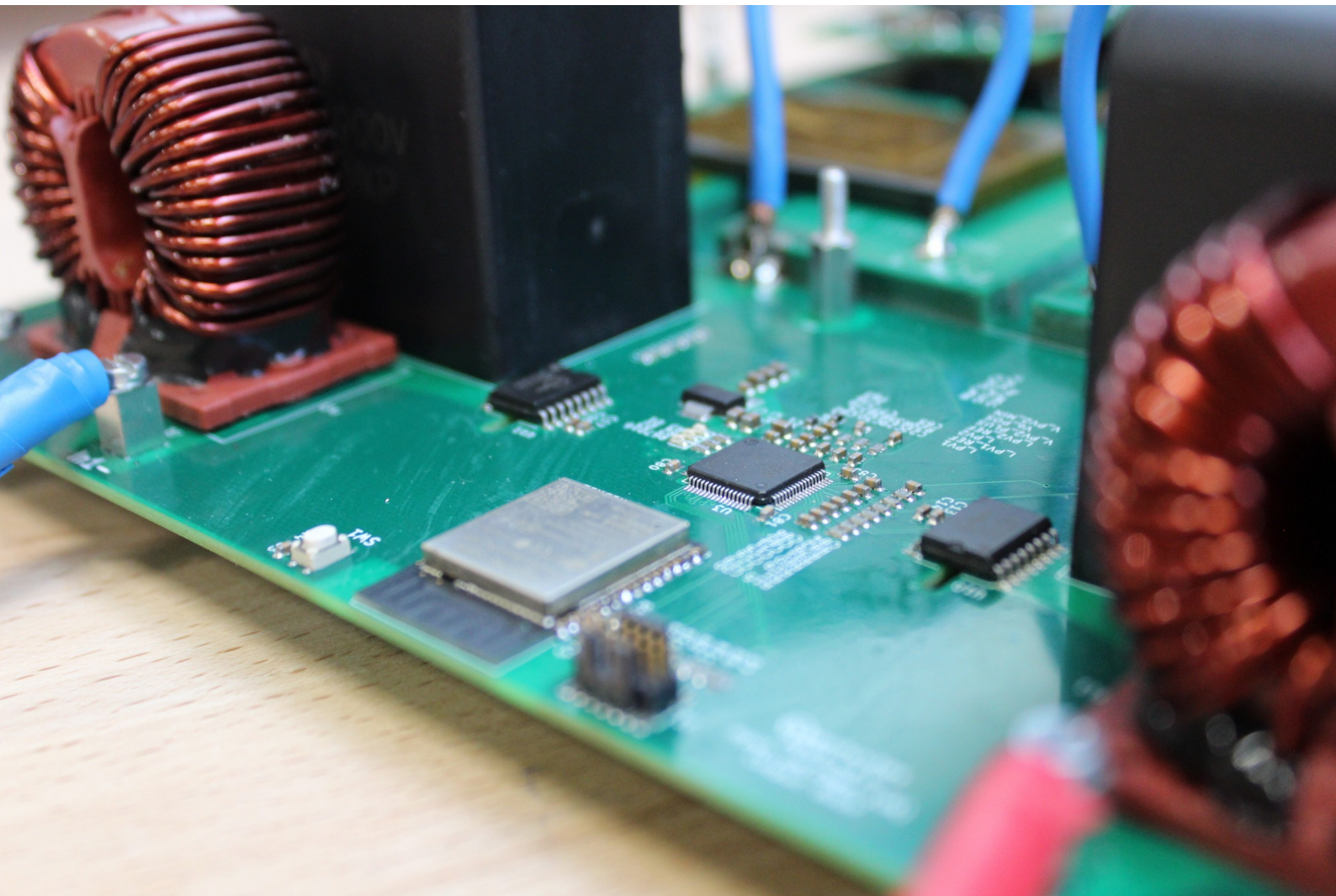


# DC-DC Converters for Photovoltaic Powered DC Microgrid

Thesis Report  
by  
Gerasimos Maroulis



---

# DC-DC Converters for Photovoltaic Powered DC Microgrid

---

*Design and testing of DC-DC  
power electronics converters for PV  
powered DC applications & Microgrids*

by  
Gerasimos Maroulis

Student Number: 4861825

In partial fulfilment of the requirements for the degree of

Master of Science

## Sustainable Energy Technology

at the Delft University of Technology,

to be defended publicly on Wednesday October 28<sup>th</sup>, 2020 at 10:00.  
This thesis is confidential and cannot be made public until 28<sup>th</sup> April, 2021.

Committee Members:

Prof. Dr. Arno Smets

Dr. T. Batista Soeiro

Dr. Zian Qin

Dr. Laurens Mackay

---

## ABSTRACT

The modern world demands more and more electric energy. At the same time, almost a billion more people are expected to gain access to electricity over the next decade. All of the above compose a very challenging future, where a continuously increasing amount of electric energy will be needed. However, the planet is not able to provide us anymore with the necessary resources for that, jeopardizing the environmental stability.

The aim of this thesis is the design and testing of power electronics converters that will contribute positively to the production and distribution of sustainable energy. In particular, a Maximum Power Point Tracking Converter is designed and tested. The 6.4kW converter is able to connect to two separate PV strings. The output of the converter is connected to a bipolar DC distribution grid. Afterwards, a 3.68kW Voltage Balancing Converter was designed for the stabilization of the voltage between the two phases of a bipolar DC grid. Particular interest is given to the challenges that arouse for the power supply of a DC Micro-Grid from a Photo-Voltaic plant. The project took place in the DC lab of the company *DC Opportunities*.

The present document concentrates the results of this research. Its purpose is to show the path that was followed from the beginning of the project and the literature study until the design and the testing of the power electronic converters. Finally, future recommendations are provided which can be used as guidelines for further improvements.

---

## PREFACE

The current thesis project is the final step for the completion of my studies in Sustainable Energy Technologies in the Technical University of Delft. Furthermore, it signifies that my academic career reaches to its end. It is a period of my life full of personal and educational development which started with the diploma of Electrical & Computer Engineering in the Technical University of Patra in Greece and concludes with the Master degree of Science in Sustainable Energy Technologies in the TU Delft.

However, I would not be able to do so without the psychological and material support of my family, my friends and my beloved girlfriend Anita. I would also like to thank all the academic members who imparted their knowledge to me. It is also important for me to express my gratitude to Dr. Laurens Mackey for his abiding guidance and sharing of his experience, as well as for trusting me to carry through some of his ideas in the lab of the company DC Opportunities along with excellent colleagues and friends.

During all these years I was given the unique opportunity to expand my knowledge in a broad range of topics. Now, I feel confident that I can apply all these skills for the benefit of the society and the common good.

<b>List of abbreviations</b>	<b>i</b>
<b>List of symbols</b>	<b>ii</b>
<b>List of figures &amp; tables</b>	<b>iii</b>
<b>1 Introduction</b>	<b>1</b>
1.1 Problem definition & motivation . . . . .	1
1.2 Objectives . . . . .	4
1.3 Key research questions . . . . .	5
1.4 General thesis outline . . . . .	5
<b>2 Literature Review</b>	<b>7</b>
2.1 The Development of Photo-Voltaic technologies . . . . .	7
2.1.1 The dependence of Photo-Voltaics on sun radiation . . . . .	8
2.1.2 The existing Photo-Voltaic systems . . . . .	9
Common PV system topologies . . . . .	9
Common MPPT converters . . . . .	12
MPPT converters for DC utility and distribution grids . . . . .	15
2.2 The Era of DC Microgrids . . . . .	15
2.2.1 The existing models of DC Microgrids . . . . .	15
Voltage balancing of distribution lines in DC Microgrids . . . . .	16
2.2.2 The socio-economic benefits of DC Microgrids in rural areas . . . . .	16

<b>3</b>	<b>Analysis &amp; Design of the Voltage Balancing Converter</b>	<b>17</b>
3.1	Introduction . . . . .	17
3.2	Theoretical analysis of the converter . . . . .	17
3.2.1	Interleaved synchronous configuration . . . . .	20
3.2.2	Bidirectional operation & inverse power flow . . . . .	21
	Boost Converter . . . . .	22
	Buck-Boost mode . . . . .	23
	Combined inverse mode . . . . .	23
3.3	Specifications . . . . .	23
3.4	Schematic overview . . . . .	24
3.4.1	Design of power electronics interleaved phases . . . . .	25
3.4.2	Design of the gate drivers circuit . . . . .	26
3.4.3	Design of the micro-electronics . . . . .	27
3.4.4	Auxiliary supply . . . . .	28
3.5	Control strategy . . . . .	29
3.5.1	Droop control of the output voltage . . . . .	29
3.5.2	Zero Voltage Switching technique . . . . .	30
<b>4</b>	<b>Analysis &amp; Design of the Maximum Power Point Tracking Converter</b>	<b>32</b>
4.1	Introduction . . . . .	32
4.2	Theoretical analysis of the converter . . . . .	32
4.2.1	Interleaved configuration . . . . .	34
4.2.2	Coupled inductors . . . . .	35
	Optimization of coupling coefficient . . . . .	38
	Summary of coupled inductors . . . . .	39
4.3	Specifications . . . . .	40
4.3.1	Application in a real project . . . . .	40
4.4	Schematic overview . . . . .	41
4.4.1	Design of the input connection . . . . .	42
4.4.2	Design of power electronics interleaved phases . . . . .	42
4.4.3	Design of the coupled inductors . . . . .	43
	Simulations of the coupled inductors in FEMM . . . . .	44

Planar inductors in PCB . . . . .	45
4.4.4 Design of the gate drivers circuit . . . . .	45
4.4.5 Design of the micro-electronics . . . . .	46
4.4.6 Design of the output connection . . . . .	47
4.4.7 Auxiliary supply . . . . .	47
4.5 Control strategy . . . . .	48
<b>5 Testing &amp; Analysis of the Results</b>	<b>50</b>
5.1 Breakdown of the test setup . . . . .	50
5.1.1 Basic devices of the test setup . . . . .	50
5.1.2 Protection control and output stabilization . . . . .	51
5.2 Test results of the Voltage Balancing Converter . . . . .	51
5.3 Test results of the MPPT converter . . . . .	53
5.4 Test results of the coupled inductors . . . . .	56
5.5 Test results of the flyback converter V.2 . . . . .	58
5.6 Discussion . . . . .	58
<b>6 Conclusion &amp; Recommendations</b>	<b>60</b>
6.1 Discussion over the research questions . . . . .	60
6.2 Future recommendations . . . . .	61
<b>References</b>	<b>63</b>
<b>Appendices</b>	<b>67</b>
<b>A Pictures of the Manufactured Converters</b>	<b>67</b>
A.1 Voltage Balancing Converter . . . . .	67
A.2 Maximum Power Point Tracking Converter . . . . .	69
A.3 Flyback Converter v.1 . . . . .	70
A.4 Flyback Converter v.2 . . . . .	71

## LIST OF ABBREVIATIONS

Symbol	Description
<i>AC</i>	Alternative Current
<i>ADC</i>	Analog-to-Digital Converter
<i>BOS</i>	Balance of System
<i>CCM</i>	Continuous Conduction Mode
<i>DC</i>	Direct Current
<i>DCM</i>	Discontinuous Conduction Mode
<i>HDI</i>	Human Development Index
<i>HV</i>	High Voltage
<i>IEA</i>	International Energy Agency
<i>μCU</i>	micro-Controller Unit
<i>MG</i>	Micro-Grid
<i>MPPT</i>	Maximum Power Point Tracking
<i>NTC</i>	Negative Temperature Coefficient
<i>PCB</i>	Printed Circuit Board
<i>PI</i>	Proportional-Integer
<i>P&amp;O</i>	Perturb and Observe
<i>PV</i>	Photo-Voltaics
<i>SDS</i>	Sustainable Development Scenario
<i>SiC</i>	Silicon Carbide
<i>SMD</i>	Surface Mount Device
<i>STC</i>	Standard Test Conditions
<i>VBC</i>	Voltage Balancing Converter
<i>ZCS</i>	Zero Current Switching
<i>ZVS</i>	Zero Voltage Switching

## LIST OF SYMBOLS

Symbol	Description	Units
$\bar{B}$	Average Magnetic flux density	T
$B_{sat}$	Saturation magnetic flux density	T
$D$	Duty Cycle	-
$\Delta I_L$	Inductor current ripple	A
$\Delta B$	Magnetic flux density ripple	T
$f_s$	Switching Frequency	Hz
$\bar{I}_L$	Average inductor current	A
$I_{Lmax}$	Maximum inductor current	A
$I_{Lmin}$	Minimum inductor current	A
$I_{mpp}$	Current at maximum power point	A
$I_o$	Output current	A
$\kappa$	Coupling Coefficient	-
$P_{mpp}$	Power at maximum power point	W
$T_s$	Switching period of the converter	s
$V_{in}$	Input voltage of the converter	V
$V_{mpp}$	Voltage at maximum power point	V
$V_{oN}$	Negative line output voltage of the bipolar grid	V
$V_{oP}$	Positive line output voltage of the bipolar grid	V

## LIST OF FIGURES

1.1	Global primary energy consumption by source [4]. . . . .	2
1.2	Electric energy demand as part of the consumed energy per global average temperature scenario [3]. . . . .	2
1.3	Prediction of the primary energy production mix in tons of oil equivalent, for a 2 °C increase of the average global temperature [3]. . . . .	3
1.4	The overview of the two designed topologies for the thesis project. . . . .	4
2.1	PV power generation according to the 'Sustainable Development Scenario' of IEA in TWh [11]. . . . .	8
2.2	Basic components of a PV 'Balance of System'. . . . .	9
2.3	Two products of centralized inverters 1.1MW from Hopewind [15] and 2MW from ABB [16]. . . . .	10
2.4	Distributed at string level 120kW inverter from ABB [16]. . . . .	10
2.5	Distributed at module level inverter from Enphase [17]. . . . .	11
2.6	The three main topologies of PV array configuration. . . . .	11
2.7	The model of a boost converter connected to a string of PV panels. . . . .	12
2.8	The schematics of more advanced boost configurations that are used for MPPT. . . . .	14
2.9	The schematics of a 60kW MPPT boost configuration with four interleaved phases from Cree [26]. It is a typical structure used for MPPT. . . . .	14
3.1	The model of a Voltage Balancing Converter. . . . .	18
3.2	The synchronous buck converters inside the Voltage Balancing Converter. The high-side buck is in red and the low side buck is in blue. . . . .	19
3.3	The voltage and the current graphs of some of the most important components of the VBC. . . . .	20

---

3.4	The model of a two phase interleaved balancing converter. . . . .	21
3.5	Inverse power flow mode (a) and the models of the formed boost (b) and buck-boost (c) converters. . . . .	22
3.6	The general schematic overview of the Voltage Balancing Converter. . . . .	25
3.7	One of the two identical interleaved phases of the designed VBC. . . . .	26
3.8	The gate driver circuits of the VBC. . . . .	27
3.9	The measuring circuits and the nodes that were measured on the VBC. . . . .	28
3.10	The overview of the auxiliary supply of the VBC. . . . .	29
3.11	The overview of the PI control in the VBC. . . . .	30
3.12	The overview of the frequency control in the VBC. . . . .	31
4.1	The model of the designed MPPT converter. . . . .	33
4.2	The overview of the coupled inductors in inverse coupling, in a two phase interleaved MPPT converter. . . . .	35
4.3	The overview of two pairs of coupled inductors in inverse and in direct coupling. . . . .	36
4.4	The plots of the currents of the two inverse coupled inductors for $D < 0.5$ . . . . .	37
4.5	The plots of the currents of the two inverse coupled inductors for $D > 0.5$ . . . . .	38
4.6	The schematic overview of the MPPT Converter. . . . .	41
4.7	The overview of one of the two identical interleaved phases of the MPPT Converter. . . . .	42
4.8	Density plot of the magnetic flux of the core, when 7A flow through the left side inductor and 3.5A through the right side inductor. . . . .	44
4.9	Two planar coupled inductors, consisting of 1 stack of 6 PCB's per inductors. . . . .	45
4.10	Overview of the gate drivers of the MPPT Converter. . . . .	46
4.11	The measuring circuitry and the nodes that were measured on the MPPT converter. . . . .	47
4.12	The overview of the auxiliary supply of the MPPT converter. . . . .	48
4.13	The graph of the applied control strategy. . . . .	49
5.1	The overview of the points that were connected to the oscilloscope. . . . .	51
5.2	The test setup of the Voltage Balancing Converter. . . . .	52
5.3	The voltage on the switching node of the mosfet $S_{11}$ and $S_{12}$ (blue), the output current on the neutral line (green) and the current of the inductor $L_1$ (red). . . . .	52
5.4	The voltage on the switching node of the mosfets $S_{11}$ and $S_{12}$ (blue), the output current on the neutral line (green) and the current of the inductor $L_1$ (red), when the converter is used in the combined inverse mode. . . . .	53
5.5	The overview of the points that were connected to the oscilloscope. . . . .	54

5.6 The test setup of the MPPT converter. . . . . 54

5.7 The 150V positive (blue) and the negative (brown) line output voltage of the MPPT converter with unbalanced inputs of 120V and 110V. . . . . 55

5.8 The 350V positive (blue) and the negative (brown) line output voltage of the MPPT converter with 200V inputs. . . . . 55

5.9 The voltage on the switching node of the mosfet  $S_{11}$  (green) and the current of the inductor  $L_{11}$  (red). . . . . 56

5.10 The current of the coupled inductor  $L_{11}$  (red), during CCM. . . . . 57

5.11 The voltage on the output of the flyback converter (blue), the voltage on the anode of the auxiliary diode (green) and the voltage on the current-sense pin of the IC (red). . . 58

A.1 The illustration of the Voltage Balancing Converter. . . . . 67

A.2 The overview of the Voltage Balancing Converter. . . . . 68

A.3 The illustration of the MPPT Converter. . . . . 69

A.4 The overview of the MPPT Converter. . . . . 70

A.5 The illustration of the Flyback Converter v.1. . . . . 70

A.6 The overview of the Flyback Converter v.1. . . . . 71

A.7 The illustration of the Flyback Converter v.2. . . . . 71

A.8 The overview of the Flyback Converter v.2. . . . . 72

---

## LIST OF TABLES

3.1	Nominal specifications of the Voltage Balancing Converter. . . . .	24
3.2	Absolute Maximum ratings. . . . .	24
4.1	Nominal specifications of the MPPT converter. . . . .	40
4.2	PV panel specifications and guidelines for the design of the MPPT converter at test conditions of $1000W/m^2$ . . . . .	40
4.3	Values of the most important parameters of the core. . . . .	43

*The booming energy consumption of the human activities creates an unprecedented demand for energy resources. This only burdens the already fragile ecosystem. The diminishing natural supplies along with the environmental stability are sacrificed in order to maintain the social growth. Simultaneously, more and more people are given access to electricity. The above make clear that drastic changes are needed that will allow both to preserve a stable ecosystem and the advance of the societal progress.*

## 1.1 Problem definition & motivation

Electricity is undoubtedly paramount for the social and the economic development of a country. The safe and ensured access to electric energy drastically affects the above. Because of its importance for the modern societies, every possible natural resource is used to produce it. The Human Development Index (HDI) is an indicator of the growth in a country, in terms of financial and social prosperity. The parameters that are used to calculate this index are the health, educational and living standards of its citizens. To a great extent, societies that suffer from extreme poverty, also lack of access to electricity. This condition which is also called "energy poverty" creates a vicious cycle, where the absence of electricity creates a gap of opportunities for the suffering people to improve their living conditions. These communities, which are mainly found in rural areas of the planet, rely on more traditional forms of energy, like biomass and wood. Hence, it is not surprising that developing countries with non-electrified territories have much lower HDI. In particular, this index can be up to 3 times less than that of a developed country [1]. As a consequence, the sustainable energy policies in those regions succumb to the need for survival. Unfortunately, even today more than 800 million people are deprived of electricity. For the first time in 2017, decades of intense global efforts reduced that number below 1 billion [2]. However, this implies that the already depleted stock of natural resources will be used in an even higher pace than before.

In the present, the largest portion of energy consumption belongs to the developed countries. The [Figure 1.1](#) presents a comparison graph of the total energy that is consumed per natural resource. It is far from obvious that the current model is extremely dependant on fossil fuels. The vast majority of energy consuming processes rely on the burning of heavily polluting fossil fuels, taking a destructive toll on the natural environment. Among them, a significant amount is spent on the production of electric energy. In an effort to reduce their carbon footprint and its destructive consequences for the environment, many sectors began to electrify their activities. This will greatly increase the efficiency of those processes. In addition, it will reduce their environmental impact, especially when the electricity is produced from a sustainable resource. Among others, the electric vehicle domain

aims to promote sustainable growth and reduce its total carbon footprint, eliminating the use of fossil fuels for the transportation of humans and goods. This signifies that a sharp rise of electric energy demand should be expected in the following decades. It is estimated that electricity will account for 45% of the total final energy consumed in 2050 [3].

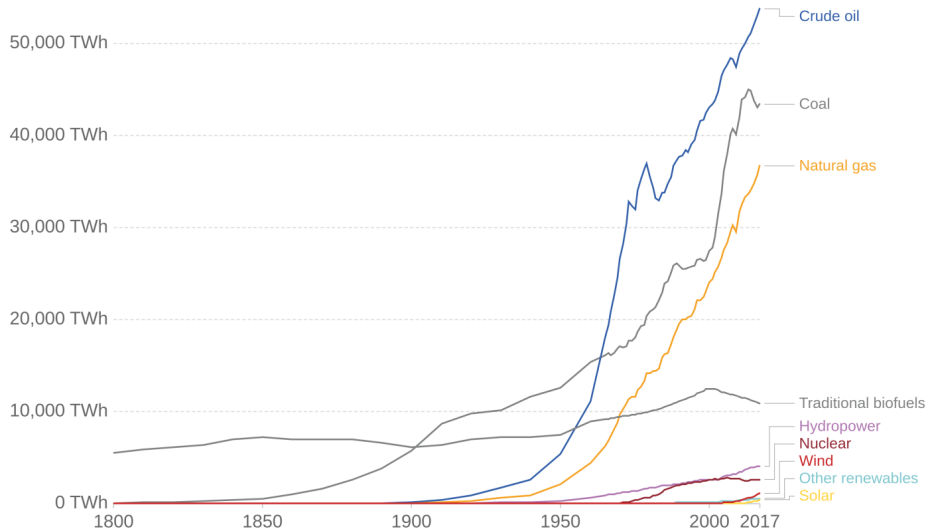


Figure 1.1: Global primary energy consumption by source [4].

All of the above, make clear that we are obliged to make important and necessary changes on the existing model of energy production and consumption. The climate crisis is just around the corner and if the world do not act fast, we will have to face unprecedented consequences. The European Union, in its Global Energy and Climate Outlook for 2019 predicts that even in the case of 1.5 °C increase of the average global temperature, at least 50% of the total energy demand must be covered with electricity [3]. The Figure 1.2 shows the two different temperature scenarios and their relation with the electric energy, as a portion of the total consumed energy.

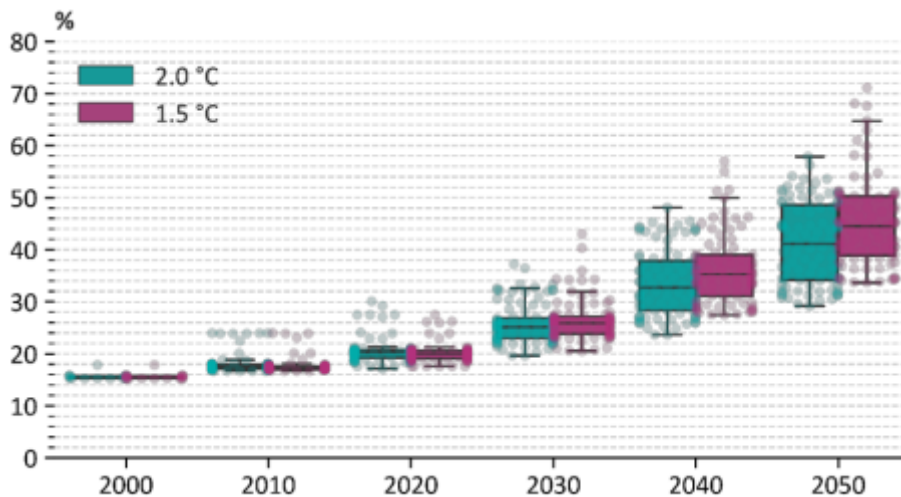


Figure 1.2: Electric energy demand as part of the consumed energy per global average temperature scenario [3].

Remarkable progress has happened over the last three decades on the field of renewable energy

production. This made the argument of substituting the traditional fossil fuels with cleaner energy, sound and achievable. Nowadays, various international environmental agreements aim to reduce or eliminate the energy footprint of the human activities, during the next 30 to 40 years. The feasibility of those agreements relies not only on the progress that is done so far, but mostly on the progress that is expected on the coming years.

According to the Global Energy and Climate Outlook for 2019 by European Commission, more than 50% of the needed energy on 2050 must be produced from renewable energy resources, in order to keep the global average temperature from rising more than 2 °C. Specifically, Figure 1.3 shows that almost 7 giga-tons of oil equivalent energy must be produced from renewable energy sources, in a scenario where the temperature of the planet rises by 2 °C. It is clear that for such a case, the use of coal and oil should be drastically diminished. Their place is taken by renewable energy resources and hydro-power plants. Photovoltaics (PV) are considered the most promising sustainable energy resource mainly for two reasons, which are: they rely on the endless sun power and they present great scalability for use in applications of various sizes.

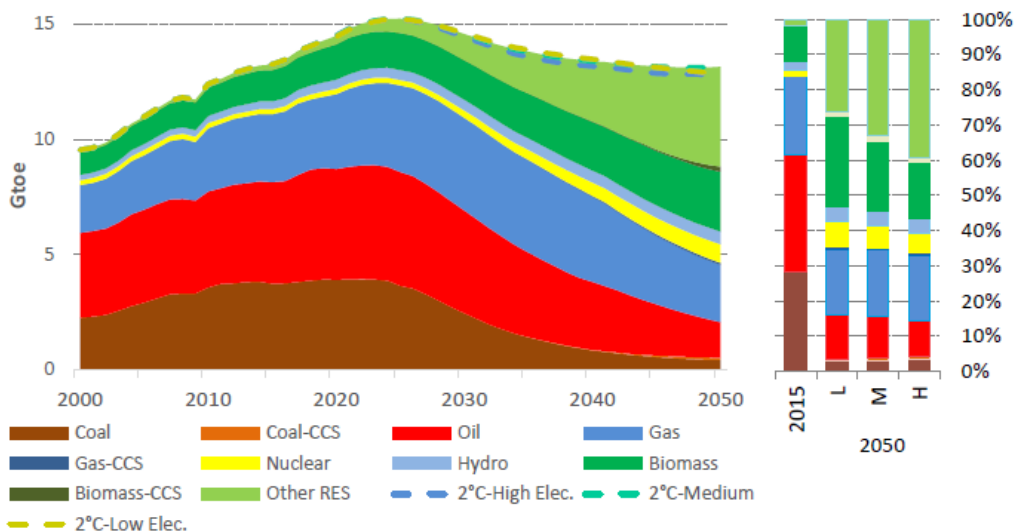


Figure 1.3: Prediction of the primary energy production mix in tons of oil equivalent, for a 2 °C increase of the average global temperature [3].

The rise of environmental awareness brought a rapid progress of renewable technologies. Most of these, like PV, produce directly DC or they use several DC-DC converters before they connect to the grid, like wind turbines. The ability of PV to be installed next to the utility or distribution grid, directly feeding the loads, reduces the transmission losses to a great extent. This implies that there is no need for high voltage transmission lines, which are fed from a big transformer. Finally, an important conversion step from DC to AC can be skipped, saving more energy and boosting the efficiency of the grid [5].

Another field which has significantly changed during the last years in favor of DC is that of the loads. Nowadays, a big number of loads that are found in households and common appliances operate in DC. For instance, consumer electronics, computers, screens, LED lighting and electronic control boards are some of the typical electricity devices around us, that work on DC. The modern power electronic semiconductors, can easily handle voltage levels of 650V, in order to create DC distribution lines of 320-400V for all the DC loads. That way, AC to DC rectifiers and power factor correction devices can be avoided, dropping the cost of the system and increasing the overall efficiency [6]. Nevertheless, this is true strictly for DC systems where the power is produced from local distributed DC sources. If the distribution system is supplied from the main AC grid, the benefit of enhanced efficiency is lost because of the losses in the bulky transformers and the rectifiers that follow [7].

The present electricity model which is based on a centralized production and transfer of the electric energy is no longer able to satisfy the modern needs. Contrary, a decentralized DC Micro-Grid approach which locally produces and consumes the needed energy under the supervision of state of the art power electronic converters is promoted. That way isolated areas could get access to electric power with the minimum long term cost.

The aforementioned are rapidly improved technologies that are actively under research because of the great potentials they present. Nevertheless, the uncontrollable character of the most renewable energy resources like PV, sets significant obstacles on the race for substitution of fossil fuels. This proves that, in order to overcome those barriers, it is important to develop power electronic converters technologies that will allow to effectively and efficiently control and distribute the electric power that is provided from the PV and the other renewable energy sources among the various decentralized points of power consumption.

## 1.2 Objectives

The main goal of this thesis is the design and manufacturing of power electronics converters for the scenario of a DC Microgrid which utilizes PV as the main provider of electric power. Specifically, a set of converter prototypes will be designed, constructed and tested for use on this specific application. Firstly, a Maximum Power Point Tracking (MPPT) converter was made, for the interconnection and optimal power harvesting of two strings of PV panels. The output of the converter is able to supply power to the DC distribution lines either in unipolar or bipolar configuration. Afterwards, a Voltage Balancing converter was constructed, which is used to stabilize and balance the voltage of the bipolar DC Microgrid lines. Finally, in order to ensure that the converters will be ready to be tested in field, two custom-made flyback converters were made, which supply low voltage to the micro-electronics of the converters. The performance of all of the above was tested and evaluated. The [Figure 1.4](#) illustrates the overview of the designed converters and their role in the bipolar DC Micro-Grid.

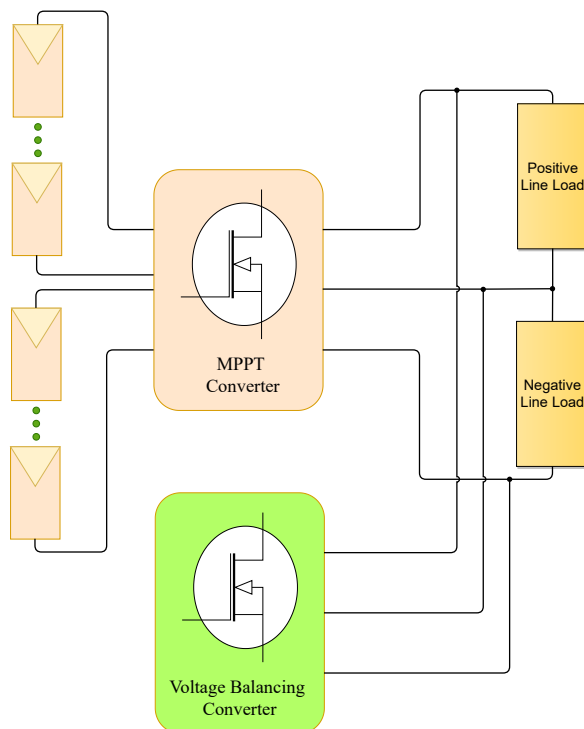


Figure 1.4: The overview of the two designed topologies for the thesis project.

### 1.3 Key research questions

The subject of this thesis was the research and the design of power electronic converters that can be utilized in a PV powered DC Microgrid. Based on these, some key research questions were formed which were used as guiding marks over the course of the project. Those questions are:

#### **How can a PV plant be integrated to a Bipolar DC Microgrid?**

Every PV power plant relies on a Maximum Power Point Tracking (MPPT) converter to operate on the optimal point of production. They have a critical role in the general performance of the power plant, affecting the cost, the losses and the complexity of the installation. Hence, one of the goals of this thesis project was the design of such a topology that will be able to connect with a Bipolar DC Microgrid.

#### **How can the voltage between the positive and the negative phase remain balanced in a Bipolar DC Microgrid?**

Given that the main goal of this project is the interconnection of a DC Microgrid with PV, it is important to take into account that there will be power flow between unipolar and bipolar DC loads. Thus, it is necessary to keep the voltage balanced among the various types of the interconnected DC loads. Otherwise, the grid stability is jeopardized, leading some loads to over-voltage.

#### **What are the possible benefits of using silicon-carbide (SiC) mosfets, zero voltage switching technique and coupled inductors for the specific converters?**

As it was mentioned before, the various power electronic converters are significant parts of a PV plant. Their efficiency can drastically affect the total losses. This makes the research of techniques that reduce the losses particularly important. Some of those techniques are targeted on the switching elements, while others on the magnetic parts of the converter.

### 1.4 General thesis outline

Over the course of this thesis project useful material was extracted from multiple sources, which range from the fields of PV technologies to that of power electronic converters and DC Microgrids. The content of this research is distributed among the various chapters of the document. Each one of them, explains in detail the collected information. The order of the chapters is such that the reader can easily follow how the project was gradually developed, starting from the problem definition up to the test of the power converters. In particular:

In [Chapter 1](#), the problem of climate crisis is analyzed from the global energy consumption point of view. Then, the important role of renewable energy resources and power electronic converters is presented. Finally, the key research questions that are the backbone of the project are elaborated, along with the thesis structure.

The [Chapter 2](#) includes the results of the literature review. The study was focused mainly on two different subjects: the current PV technologies and the development of the DC Microgrids. The outcome of the literature review is the in-depth understanding of the present technologies and the challenges of the design of DC-DC converters for PV powered DC Microgrids.

The [Chapter 3](#) and [Chapter 4](#) deal with the analysis of the two DC-DC power electronic converters that were designed and tested for this thesis project. The Voltage Balancing Converter and the Maximum Power Point Tracking Converter are explicitly explained, through a series of analysis steps. Firstly, the theoretical background is presented, providing the necessary equations and graphs that illustrate the various conversion steps. Afterwards, based upon the previous analysis, the specifications of the designed converter are summarized in a table. Then, the converter is split in several sub-parts. Each sub-part is elaborately presented, focusing on the role of the individual components that were used.

In [Chapter 5](#), the results of the experiments that were done to the manufactured converters are shown and commented. High voltage is applied to their inputs, while protection control schemes make sure that the output voltage remains stable and under the over-voltage limits.

The [Chapter 6](#) summarizes the most important results of the project. It also explains how the research questions were answered, as well as it provides future recommendations.

Finally, the [Appendix A](#) includes the pictures of the manufactured converters. The pictures that are provided aim to focus on the structure of the topologies. The most important sub-parts are shown with arrow pointing comments.

*This chapter presents the collected information of the literature review. The review was focused around two different topics, which are however strongly related. The first section, refers to the Photo-Voltaics and the development of this technology, as the future sustainable power provider. Finally, the benefits of DC Microgrids are discussed, as the forthcoming power distribution model, integrating the advantages of both Photo-Voltaics and DC systems, especially for the electrification of rural and isolated areas.*

## 2.1 The Development of Photo-Voltaic technologies

Among the various renewable energy resources, Photo-Voltaics (PV) are gaining great portion of the research and investment attention. The advent of modern PV technologies and materials brought cells which present low cost, increased efficiency and high volume of produced power per  $\text{m}^2$  [8]. These materials absorb the sunlight and through the photovoltaic effect, they produce electric power. The ability of PV to be easily scaled-up, made them suitable for various projects and installations which range from a few kW up to hundreds of MW power plants. Hence, they can be installed equally well in small projects like the roof of a home or the electrification of a rural inhabited area, which is far from the local electricity grid.

The market of PV made its first steps in the last decade of the twentieth century. The kick-start of this industry was activated with subsidies that were given either by governments (like in Germany and Japan) or international organizations which soon realized the great potentials of this technology. Since then, the market of PV grew to be one of the biggest and most rapidly expanding of the world. The intense research that takes place over the last years reduced the cost of PV cells manufacturing. Furthermore, the accumulated experience on the installation and the maintenance, significantly lowered the total investment price. This makes PV an absolutely competitive solution of energy production [9].

Various types of materials and technologies have been tested and utilized. Some of them are already used in the PV industry, while others are still under research, either trying to expand the full benefits of the material or reducing their manufacturing cost. Overall, the PV technologies consist of 3 different generations. The first one includes the mono and poly-crystalline silicon PV cells. This generation is the oldest and most developed, dominating the market. Following, the second generation relies on rare materials like Indium (In), Tellurium (Te) or Selenium (Se). The advantage of this generation is their mechanical flexibility, which makes them suitable for particular applications. Furthermore, their production cost is expected to drop below that of the first generation, in the coming years [8].

Nevertheless, they cannot be used for mass production of PV panels, given that rare materials must be intensively extracted. Finally, the third generation, which is the youngest, is made of organic materials, but it is still on testing phase, far from mass production [10].

Nowadays, Photo-Voltaics are considered the drive-train on the race to make the energy production sector greener. The International Energy Agency (IEA) on its 'Sustainable Development Scenario' (SDS) predicts that in 2030 over 3300 TWh will be produced annually from PV [11]. Only in 2019, the total installed power of PV around the world was increased by 22%, reaching 720 TWh of produced energy in that year. This expansion of installed capacity, brought PV to the third place of the renewable energy producers behind onshore wind and hydro-power, accounting for 3% of the global generation of electricity. The Figure 2.1 presents the upward trend of the PV-produced energy, from 2010 until 2030. It is clear, that over the following decade Photo-Voltaics are expected to account for a significant amount of the yearly produced energy.

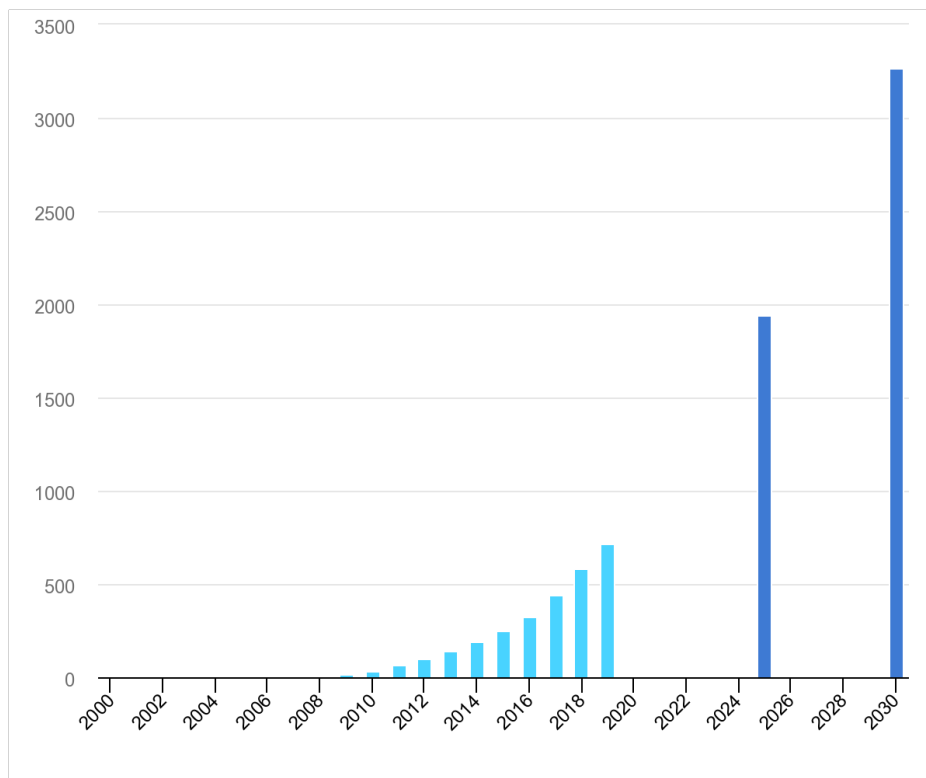


Figure 2.1: PV power generation according to the 'Sustainable Development Scenario' of IEA in TWh [11].

### 2.1.1 The dependence of Photo-Voltaics on sun radiation

One of the main reasons which delay the domination of PV in the energy production sector is their dependence on the weather conditions. The uncontrollable character of sustainable energy sources combined with the rising global energy demand create an unprecedented challenge for the reliable operation of the electricity grid. The hard to predict daily and seasonal variations of the available sun radiation make the accurate estimation of the produced power a very complex procedure. This can have detrimental consequences for the normal operation of the electricity grid, as it can cause sudden shortage of power and black-outs.

Another challenge that must be dealt with is the so-called 'duck curve problem'. Specifically, the PV are able to produce their maximum amount of power during the middle of the day, when the

sun radiation is at its peak. However, the load demand curve, which depends on human activities and habits, has a completely different shape, that resembles with a duck floating in the water, hence the name. The peak of this curve happens several hours later than the peak of the PV production. This creates a miss-match of produced power and demand which has to be covered either by other renewable resources or conventional fossil fuel power plants. Today, advanced power electronics and battery storage systems are more and more utilized to solve this problem.

### 2.1.2 The existing Photo-Voltaic systems

Besides the PV panels, a Photo-Voltaic system consists of multiple other electrical devices and components. In particular, power electronics converters, transformers, cables, batteries and mechanical support equipment are needed for the interconnection of the PV with the electricity grid or the stand-alone loads. The sum of the necessary components is called Balance of System (BOS) [8]. The Figure 2.2 illustrates the most common parts of a PV BOS.

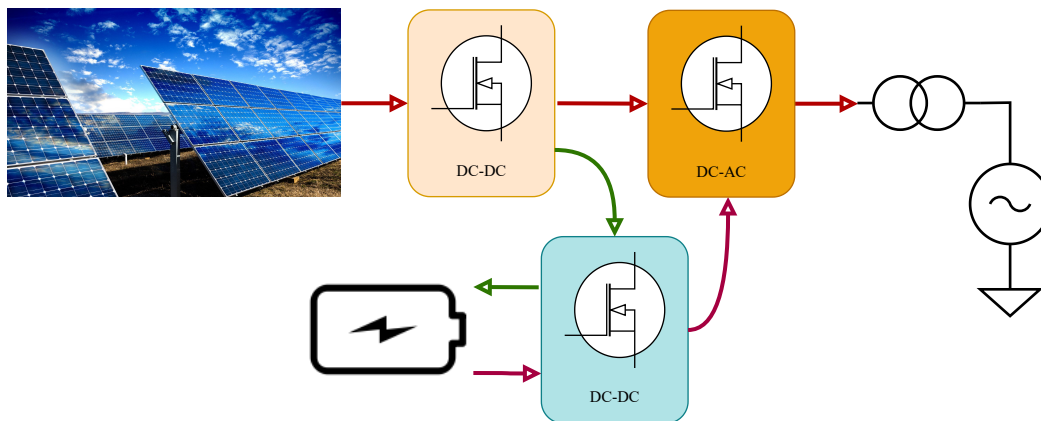


Figure 2.2: Basic components of a PV 'Balance of System'.

#### Common PV system topologies

Several PV array typologies are proposed in the literature. The optimal choice is decided upon parameters like the conversion losses, cost reduction and safety. In general, three different configurations are mainly used: the centralized, the distributed at PV string level and the distributed at PV module level [12].

In the **centralized** configuration, the PV strings are connected in series or in parallel with the main power converter module which includes both a DC-DC converter and an inverter. When the input voltage from the PV panels is high enough, the DC-DC step can be neglected. The use of less components makes the device more reliable [13]. The DC input voltage of this configuration can reach the 1500V DC. The maximum point tracking (MPPT) algorithm is implemented inside the main inverter of the system. Usually, a transformer follows, for galvanic isolation. These transformers usually are heavy and expensive. Sometimes, they are connected to a rectifier and then to a second inverter, which supplies the grid. This way, they can be smaller in size, operating in higher frequency. Nevertheless, the use of a transformer with multiple conversion steps has a negative impact for the losses of the system. The efficiency of the topology is lower compared to other because it is not possible to extract the maximum amount of power from each PV string individually. Hence, a significant amount of power is burnt in the PV by-pass diodes because of partial shading [14]. The Figure 2.3 shows two centralized inverters. The left inverter is a product of the company Hopewind for applications of 1.1MW, while the right inverter is from ABB. This inverter is suitable for PV plants of 2MW, including a three-phase inverter.



Figure 2.3: Two products of centralized inverters 1.1MW from Hopewind [15] and 2MW from ABB [16].

The **distributed at PV string level** topology is the most commonly used in commercial projects, where the voltage can reach 1500V DC. A string of PV panels is connected to a DC-DC converter. This converter implements the MPPT control. The benefit of this system is the increase of the extracted power from each PV string, because the control can be better applied in sub-groups of the total plant, reducing the effects of partial shading between strings. Afterwards, several strings connect with a centralized inverter. Depending on the size of the plant, multiple inverters can be connected in parallel in the same phase or in different phases with  $120^\circ$  delay [13]. A three-phase inverter for distributed at string level applications is shown in Figure 2.4. The inverter can be connected to 6 different PV strings supplying 120kW to a transformerless inverter.



Figure 2.4: Distributed at string level 120kW inverter from ABB [16].

Finally, the **distributed at PV module level** configuration is suitable for smaller applications, where each individual PV module has its own DC-DC converter and micro-inverter. Initially, a DC-DC converter boosts the voltage of the panel, which usually ranges from 22V-45V, to the voltage level of the distribution grid. The benefit of this structure is that it provides the optimal MPPT control, custom-made for each PV module. However, from a cost point of view, this is the most expensive option, since it requires the highest amount of converters [8]. The Figure 2.5 illustrates a micro-inverter from Enphase.



Figure 2.5: Distributed at module level inverter from Enphase [17].

The Figure 2.6 illustrates the three aforementioned configurations.

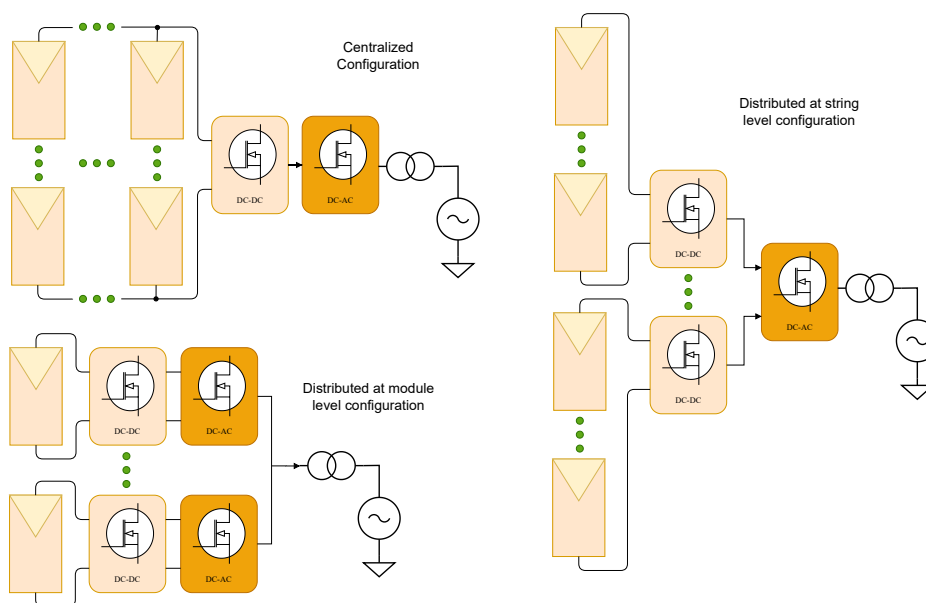


Figure 2.6: The three main topologies of PV array configuration.

Frequently, a battery storage unit is also part of the PV system, especially in applications that supply stand-alone loads. The excess of sun energy can be stored for use when it is necessary. This is also a proposed solution of the 'duck curve problem'. But, the existence of such a battery storage system implies that more power electronic converters are needed, which will regulate the charging and the discharging of the system [18].

### Common MPPT converters

The power electronic converters are essential for the optimal operation of a PV system. They are responsible for the control, the fault detection and the optimal power harvesting. Without them, the PV cannot be connected to the electricity grid, while the produced power will be far below the optimal scenario. Because of that, the cost and the complexity of the PV systems are considerably increased. In some case, the cost of the power electronics can be close to 20% of the total system cost [19].

As it was discussed before, the vast majority of the High Voltage and Power PV projects rely on a distributed at string level DC-DC converter which implements the MPPT algorithm and a DC-AC inverter for the connection with the grid. Today, most of the DC-DC MPPT converters that are connected to the utility grid produce output voltage which ranges from 700V to 850V DC. Afterwards, the inverter converts it to three-phase 480V AC.

Today, the modern MPPT strategies demand cheap power electronic converters, with high power density. The semiconductor components must be able to handle voltage levels above 1kV and current ratings of several amperes. From an electrical engineering point of view, this is a serious challenge that must be answered. Otherwise, the lifetime of the device is reduced, increasing the maintenance cost. In addition, there is significant drop of the harvested energy, which translates into pay-back delay of the investment. The progress of semiconductor material technologies, like the Silicon-Carbide (SiC) mosfets, created power electronics which present lower losses. This allows to design more efficient power electronic converters. Moreover, these new products can switch in much higher frequencies, up to 300 kHz, increasing the power density of the design [20].

Various power electronic configurations have been proposed and tested as MPPT converters, over the last 20 years . In most of the PV projects, the MPPT algorithm is implemented in a DC-DC converter which intervenes between the PV array and the inverter. The most frequently used MPPT converter is the boost (Figure 2.7). This contraction is able to step-up the input voltage, with high efficiency for a very broad range of duty cycle and relatively low hardware complexity [20].

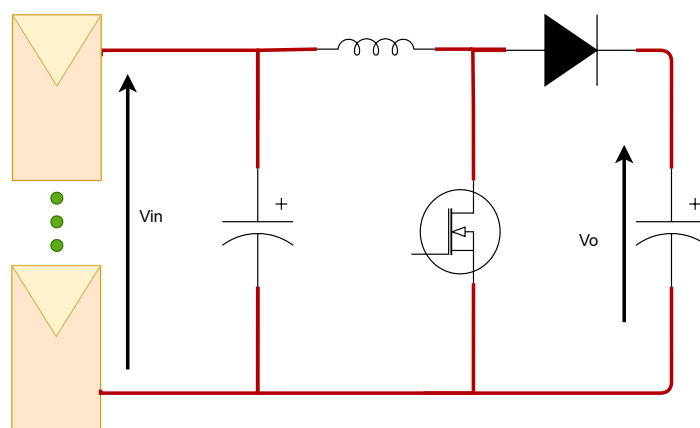


Figure 2.7: The model of a boost converter connected to a string of PV panels.

Despite the structural simplicity of the boost converter, it is often necessary to shift to more complex

variations of the basic design. This is needed because, as it was discussed before, the rising voltage and current ratings of modern PV applications are a tremendous challenge for the present semiconductor and magnetic components. Inadequate loss reduction strategies translate to significantly lower performance, even destruction of the device. Some changes of the basic topology aim to improve the voltage rating of the device, while others to reduce the losses on the semiconductors and the inductors. The following lists presents some of the most promising concepts that are under research or already implemented [21]:

The most popular techniques for the reduction of losses and the thermal dissipation are:

- Interleaved configuration: Multiple boost converters share the same PV input and the same output. This allows to distribute the input current among the various phases. Hence, smaller and cheaper components can be used, for lower current ratings, spreading the heat stress among a larger number of materials.
- Zero Current Switching (ZCS) & Zero Voltage Switching (ZVS): These are techniques which aim to switch-on and off the power electronics when their current and the voltage respectively are as low as possible (ideally zero). This eliminates the switching losses on the semiconductor components [22]. However, in order to implement these techniques, it is needed to add several components on the system and elaborate frequency control techniques, something that complicates the design of the DC filter. All the proposed circuits for the implementation of active or passive ZVS and ZCS need quite a few extra components and mosfet gate driving circuits.
- Coupled inductors: Combined with the interleaved configuration, the coupled inductors allow to magnetically connect several magnetics into one core. This provides better transient response, reduced core losses and smaller size.

The next list shows some of the most discussed topologies which deliver improved voltage and current rating converters:

- Three-Level Boost Converter: The goal of this topology is to split the output voltage in equal pieces, which are supplied from different identical sub-parts of the converter. This allows to use semiconductors which are rated for lower voltage than that of the output. The total losses are reduced, while the EMI behaviour is improved because of the lower  $\frac{dV}{dt}$ .
- Cascade Boost Converter: This configurations is actually a trailer of two independent simple boost converters. The first one amplifies the input voltage up to the desired level, operating in high switching frequency. Following, the second converter amplifies that voltage to its final level, with much lower switching frequency. The merit of this configuration is that the voltage is amplified gradually, with two smaller gains. This drops down the current ripple, reducing the overall losses. On the other hand, two times more components are needed compared to the normal boost version. Also, the outer boost components must be rated for full output voltage.
- High Step-Up Boost Converter: The last converter of this list uses coupled inductors and switched capacitors to amplify the input voltage. The first version which relies on coupled inductors, operates them as an auto-transformer. The turns ratio between the windings of primary and secondary determines the voltage gain. Usually, a clamping circuit is needed to absorb the leakage inductance ringing on the mosfet [23]. The second version of high step-up converters utilizes switched capacitors, in repeated cells of a semiconductor and a diode. This model has no need for magnetic components [24]. The capacitors work as voltage sources. In [25] a resonant tank is used, reducing the need for active semiconductor components like mosfets, which are substituted from diodes. To conclude, the need for high number of components like capacitors, make this type of converters suitable only for low power applications.

All of the above, are techniques which can be widely used, in **every** power electronics converter. However, they attract particular interest in MPPT applications. The [Figure 2.8](#) presents the schematics of the most important converters that are used for MPPT.

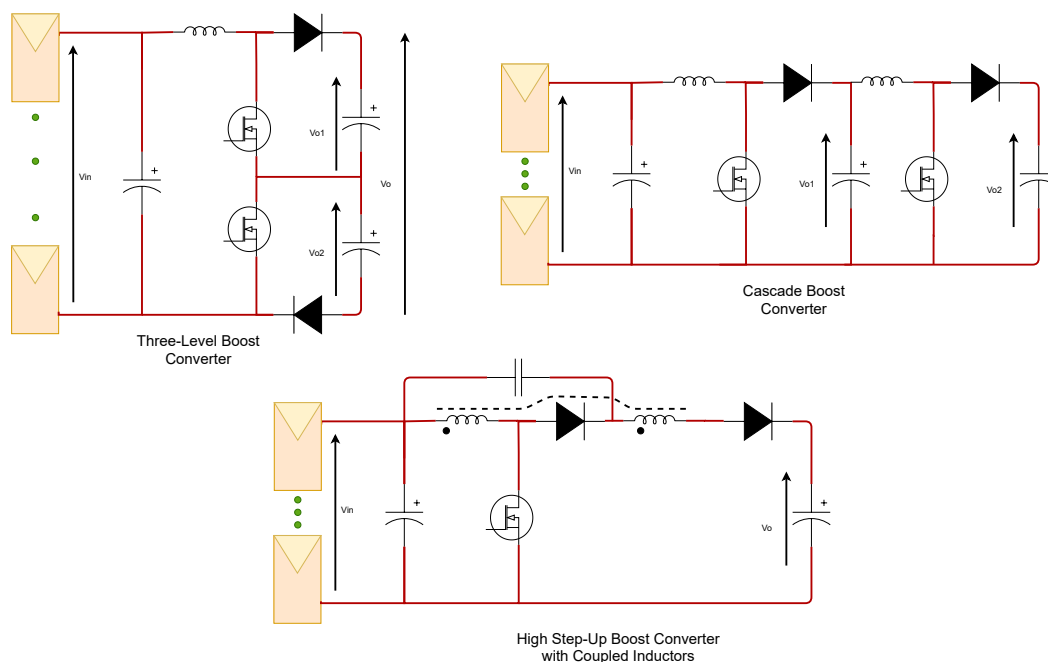


Figure 2.8: The schematics of more advanced boost configurations that are used for MPPT.

The vast majority of MPPT converters, are based on the simple boost converter, usually in interleaved configuration. The Figure 2.9 is the model of a 60kW MPPT converter from Cree. The converter consists of four boost interleaved converters, supplied by two inputs. The 850V DC output is connected to a three-phase inverter. The particular design is a very commonly used topology in real-life applications.

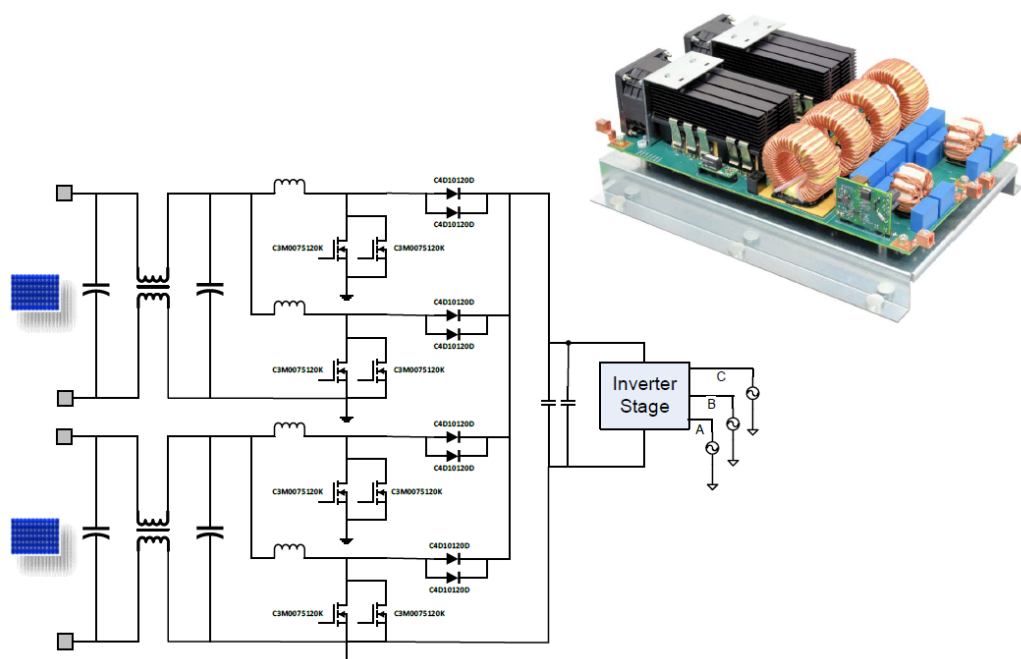


Figure 2.9: The schematics of a 60kW MPPT boost configuration with four interleaved phases from Cree [26]. It is a typical structure used for MPPT.

### MPPT converters for DC utility and distribution grids

The advent of DC systems allows to skip the DC-AC conversion, when the PV plant supplies power to a DC utility grid. Then, the DC-DC converter is responsible to harvest the maximum amount of power controlling the input voltage. The voltage of these converters must range from 700 to 1500V DC. Furthermore, the MPPT converters must be able to connect to bipolar DC grids, supplying power in both positive and negative grid phases. In that case, the output of the converter must range from  $\pm 350\text{V}$  to  $\pm 750\text{V}$  DC [27].

## 2.2 The Era of DC Microgrids

The urgent environmental challenges and dilemmas, demand drastic changes of the present power production and distribution model. In order to cover the forthcoming increase of energy demand, it is necessary to transform the present system, in a way that will make it more adjustable, efficient and interactive [28]. The intensive progress that occurred on the grounds of renewable distributed generation units, like PV, gave birth to the idea of Microgrids (MG). Microgrids are dispersed grid topologies which usually consist of a power production unit, energy storage systems and local loads. Some MG are connected with the grid, while other are isolated (stand-alone) [29]. As a consequence, various autonomous distribution sub-grids can be locally developed, providing more effective control of the power flow both inside the MG itself, as well as between neighboring MG and the grid.

### 2.2.1 The existing models of DC Microgrids

Currently, there are two different models of MG: The DC and the AC Microgrids. Each one of the different configurations has different characteristics. The most suitable MG depends on various parameters which are usually specified per project. So far, DC Microgrids are mostly installed in the telecommunication sector, marine projects and electric vehicles [30]. The progress of the power electronics technologies is expected to make the DC Microgrids the first choice for almost every application in the future. The comparison of the DC and AC Microgrids is usually done in terms of: distribution line losses, protection, power converters, power quality and control complexity [29].

As it was discussed before, the DC systems present lower transmission line losses than their AC counterparts, which are mainly resistive. At the same time, the skin effect is eliminated, allowing higher power level to flow. The same principals apply in the distribution lines, which means that more local loads can be supplied, compared to the AC version. On the other hand, ensuring the safety of users in DC systems is still a significant challenge, mainly because of lack of practical experience compared to AC systems, which are installed and tested in a huge range of applications for more than a century. The weakest point of the protection schemes in DC is the waveform of the current that never crosses zero, something that makes the design of short-circuit breakers more difficult. Nevertheless, in low DC voltage applications, typical AC circuit breakers can be used, as long as their power rating is adjusted for DC [29].

Regarding the power converter criteria, in both cases various converters are needed. Usually, a transformer is included between the distributed power source and the local loads of the Microgrid, offering galvanic isolation. Given that nowadays the number of DC loads is increasing, DC Microgrids could provide less conversion steps, since the AC to DC conversion can be skipped. In addition, the power quality and the control complexity of DC Microgrids shows better results. The reason is the absence of frequency and reactive power control that is required in the AC case.

The DC Microgrids are still on their early age, something that creates a gap of standardization. There is a lot of debate around the design protocols and the safety standards. The voltage levels that are mostly applied in the existing DC Microgrid infrastructure range from 320V to 400V [28], with the most attractive option being that of 326V [31]. The reason behind this proposal is that this voltage

is equal to the peak of the 230  $V_{rms}$  AC. In principal, all the existing DC loads can be connected to such a voltage, just by disconnecting their internal rectifier. Also, the existing AC distribution infrastructure can be used, reducing the cost of the transition from AC to DC.

Overall, two different ways are proposed for the construction of the DC distribution grids, the unipolar and the bipolar. The first one (the unipolar) requires only two cables, which carry the full grid voltage. The second option (the bipolar) needs three wires. Two of them serve as positive and negative lines, while the third is the neutral. Even though, the bipolar version seems more expensive, it provides several advantages. Firstly, the same network can supply power to big industrial loads and smaller commercial loads. The higher loads can be supplied connecting between positive and negative, while the smaller can connect in any of the two phases of the bipolar grid (positive-neutral or neutral-negative). Secondly, any fault on one of the phases does not affect the power transmission on the other phase [32].

### Voltage balancing of distribution lines in DC Microgrids

If the loads between the two phases are balanced, then the voltage is equally distributed between them. In a different and most frequent scenario where the loads are unbalanced, one of the loads is overcharged while the other is undercharged. Similar to the AC voltage balancing that must be implemented among the 3-phase lines, DC bipolar distribution grids need an analogous converter. This voltage balancing converter ensures that the supplied voltage in the bipolar distribution lines, remains between the acceptable safety limits of operation. Otherwise, any inequality of the connected loads on the positive and the negative pole, will create over-voltage on one of the sides [29]. This converter is analyzed in depth in Chapter 3, where it is explained how such a topology was designed and tested.

Overall, the beneficial capabilities of DC Microgrids appear to be the key for the development of environmental friendly distribution grids with increased efficiency and enhanced power quality. However, it is expected that the DC Microgrids will coexist with the AC Microgrids, since the transmission system is still dominated by AC. Nevertheless, this is not expected to last long, given that the development of HVDC transmission lines and state of the art power converters is growing.

### 2.2.2 The socio-economic benefits of DC Microgrids in rural areas

The previous sections discussed the profits that can be extracted from the advent of DC Microgrids. Those topologies are appealing in a broad range of applications. Many countries, such as Spain, Denmark and Germany are already applying this technology, anticipating higher residential loads that can be satisfied from dispersed renewable sources. Over the last years, an increasing number of countries with citizens that suffer from energy poverty realized the merits of DC Microgrids [33]. As it was thoroughly analyzed in Section 1.1, the living and health standards of a community are strongly related to the access to secured and cheap electricity. As a consequence, an impressive number of Microgrid projects has already been or will be constructed in the coming years, in rural non-electrified areas. Usually, hospitals, schools and other facilities are then built, improving the lives of local people.

In most of the cases, multiple shareholders are engaged in the making of such a Microgrid. The World bank, United Nations, governments and private sector are usually the main participants. Only in China, more than 500 MW of PV in stand-alone Microgrids were installed, between 2005 and 2010. India presents the highest motivation for the creation of local Microgrids. The governmental policies strongly incentivizes the citizens to buy electric vehicles, using their batteries to store energy. Furthermore, more than 500 MW of renewable distributed sources will be installed in the coming 5 years [33].

## CHAPTER 3

# ANALYSIS & DESIGN OF THE VOLTAGE BALANCING CONVERTER

*The arrival of DC Microgrids depends on the progress of the DC power distribution sector. Advanced Voltage Balancing converters that will keep the voltage levels of the bipolar power lines inside the allowable limits, are needed.*

### 3.1 Introduction

The Voltage Balancing Converter (VBC) is an interconnection device which is installed between the positive and negative lines and the DC bipolar loads of the microgrid. The goal of this converter is to create the bipolar grid, while keeping the positive and the negative line voltage within the acceptable limits. The converter is able to shift the power consumption between the two bipolar phases, for a specific range of imbalanced loads. The amount of power that this converter has to process depends on the degree of imbalance of the system. The benefit of such a configuration is that, the neutral line can be skipped for big parts of distribution grid, installed only close to the supplied loads, saving a significant amount of copper cost. The absence of such a converter can lead to serious malfunction of the normal operation of the bipolar grid. Any asymmetry between the positive and the negative phase loads can cause voltage imbalance, load shedding, or even destruction of parts of the grid.

In the case of AC rectification for the production of DC, it is common practise to use Neutral-Point-Clamp converters. These devices are able to implement both rectification and voltage balancing for a limited range of load imbalance [34]. However, when the power is produced from DC sources, it is fed to DC-DC converters. These converters are not able to implement voltage balancing. This task is assigned to a VBC. The input of the VBC is the positive and the negative line of the distribution grid. The topology which was designed and tested for this project is based on [35].

### 3.2 Theoretical analysis of the converter

This section focuses on the theoretical exploration of the topology. This is done, extracting the relationships that characterize the voltage and the current of the most important electrical nodes of the converter. This will allow to deeply understand the power conversion steps, calculate the power losses and specify the safe operational limits of the device. The [Figure 3.1](#) illustrates the electrical model of the VBC. The structural simplicity of this converter makes it favorable for this

kind of applications. The input voltage of the balancing converter is usually supplied from a DC-DC converter which regulates the produced power of a DC generator, like PV.

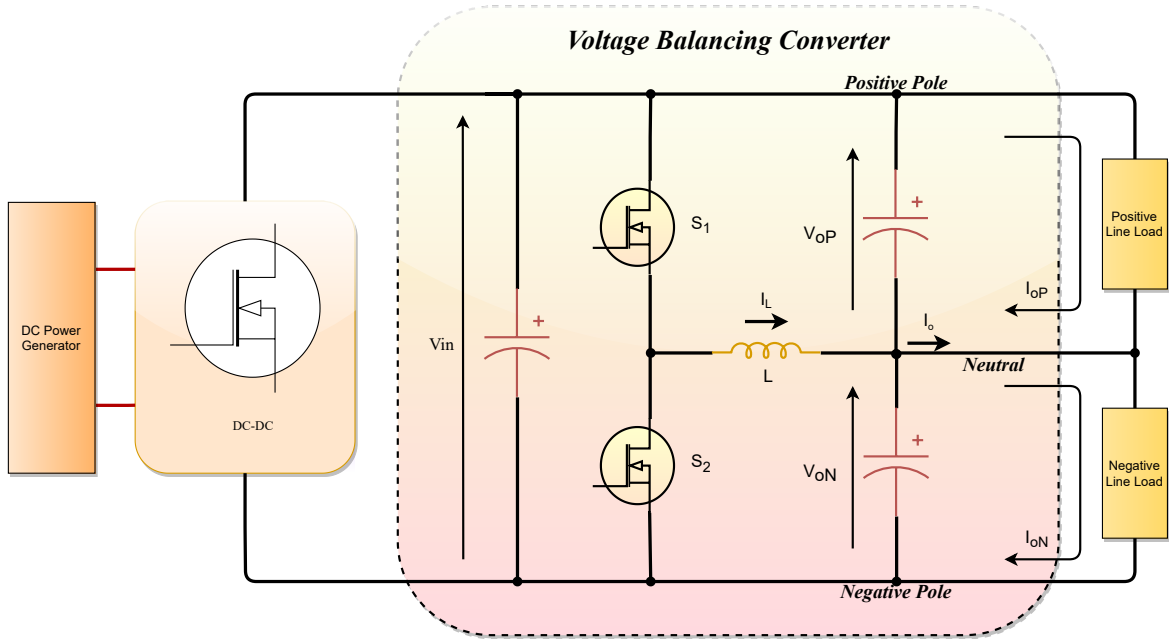


Figure 3.1: The model of a Voltage Balancing Converter.

The above figure makes clear that:  $V_{in} = V_{oP} + V_{oN}$ . When the converter is in steady state, the average current that flows through the output capacitors is zero. Hence, the average inductor current is equal to the output current:  $\bar{I}_L = I_o = I_{oN} - I_{oP}$ . The aim of the balancing converter is to keep  $V_{oP} \approx V_{oN}$ . Often, in the modern DC Microgrids, the  $V_{in} = 700V$ . Then, the VBC must stabilize the output voltages to  $V_{oP} = -V_{oN} = 350V$ . When the positive and negative line loads are equal, the  $I_o = 0$ , because  $I_{oP} = I_{oN}$ .

The analyzed topology uses a synchronous half-bridge of semiconductors ( $S_1$  &  $S_2$ ). This allows the bidirectional power flow, in case it is needed. Also, the use of a semiconductor instead of a diode, reduces the conduction losses and allows to implement ZVS techniques, as it will be explained later. However, this comes at a price, since more gate driving circuits are needed. Because of the synchronous half-bridge configuration, the current of the inductor can flow in both directions, forcing the converter to operate in continuous conduction mode (CCM). Thus, the control of the output voltage can be done exclusively with the adjustment of the duty cycle,  $D$ . The inductor  $L$  forms an output filter with the positive and the negative side output capacitors.

For the rest of this section, the duty cycle of the converter is referred to the switch-on time of the high side semiconductor,  $S_1$ . This creates two independent sub-circuits inside the main converter. Thus, the explanation of the topology can be simplified. In particular, two synchronous buck converters are formed. The first one includes the high side semiconductor and the negative line output voltage, with duty cycle  $D$ . Simultaneously, the same applies for the positive side output and the low side semiconductor  $S_2$ , which operates with duty cycle  $1 - D$ . The Figure 3.2 presents the two synchronous buck converters, in red and blue color.

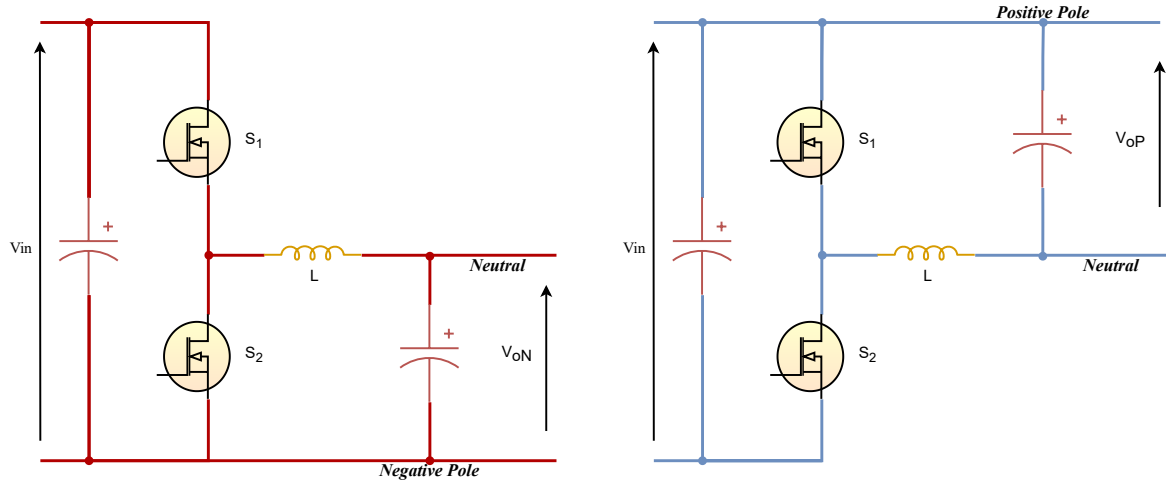


Figure 3.2: The synchronous buck converters inside the Voltage Balancing Converter. The high-side buck is in red and the low side buck is in blue.

According to the equations of the synchronous buck converter in CCM:

$$V_{oN} = DV_{in} \quad [\text{V}] \quad (3.1)$$

$$V_{oP} = (1 - D)V_{in} \quad [\text{V}] \quad (3.2)$$

The [Figure 3.3](#) illustrates some of the most important parameters of the circuit. The following equations are used to calculate the average,  $\bar{I}_L$  and the peak values of the inductor current, as well as the inductor current ripple,  $\Delta I_L$ , which are necessary for the determination of the specifications of the magnetic components and the output voltage ripple.

$$\bar{I}_L = \frac{I_{Lmax} + I_{Lmin}}{2} = I_o \quad [\text{A}] \quad (3.3)$$

$$\Delta I_L = I_{Lmax} - I_{Lmin} = \frac{(V_i - V_o)DT_s}{L} = \frac{V_i(1 - D)DT_s}{L} \quad [\text{A}] \quad (3.4)$$

Combining the [Equation \(3.3\)](#) and the [Equation \(3.4\)](#), the  $I_{Lmax}$  and the  $I_{Lmin}$  can be calculated:

$$I_{Lmax} = I_o + \frac{\Delta I_L}{2} \quad [\text{A}] \quad (3.5)$$

$$I_{Lmin} = I_o - \frac{\Delta I_L}{2} \quad [\text{A}] \quad (3.6)$$

The  $I_{Lmax}$  and the  $I_{Lmin}$  are very important parameters for the choice of the appropriate inductor, because they determine the saturation current limit of the component. Otherwise the inductor will enter the saturation region, which can have detrimental consequences for the device. Furthermore, the  $\bar{I}_L$  dictates the value of the rated current that flows through the magnetic component, in order to keep the losses under control. If not, the inductor presents degradation of its nominal inductance and overheating.

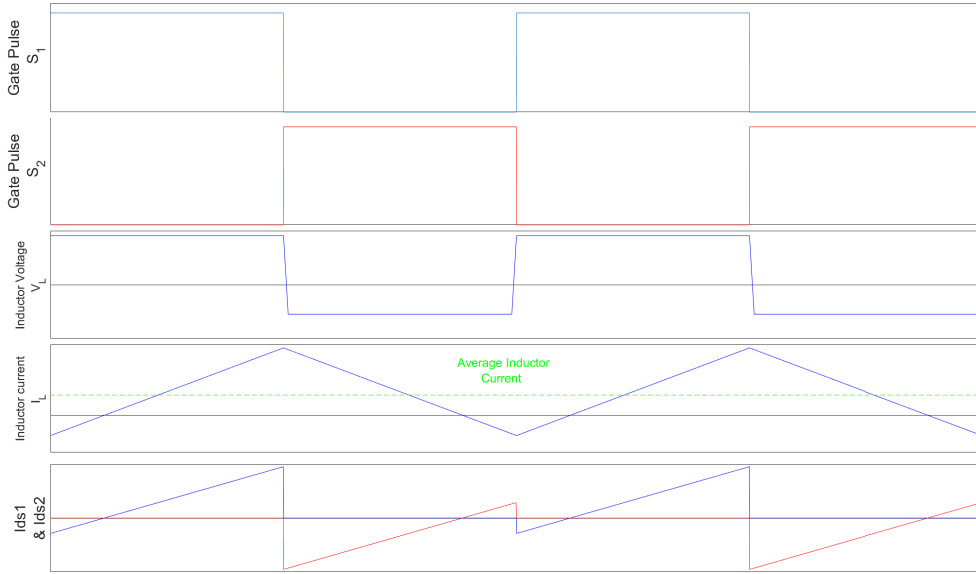


Figure 3.3: The voltage and the current graphs of some of the most important components of the VBC.

### 3.2.1 Interleaved synchronous configuration

According to the material that was discussed in previous chapters, a common and very effective manner to reduce the current rating of particular components is the use of interleaved configuration. Specifically, in the case of a Voltage Balancing Converter, one or more identical half bridges with separate inductors or phases are connected in parallel. The advantage of this topology is that the multiple phases share the input current. Thus, semiconductors and inductors with lower current ratings can be chosen. Furthermore, the existence of two half-bridges improves the output voltage performance, reducing its ripple. The two branches operate with a phase shift of  $180^\circ$ . Thus, the output voltage harmonics that are not filtered by an individual output inductor-capacitor filter, are canceled out, when the duty cycle of the converter is 50%. The [Figure 3.4](#) shows the design of an interleaved balancing converter.

Given that, now the average inductor current is half of the output current, the previous equations are adjusted to:

$$\bar{I}_L = \frac{I_o}{2} \quad [\text{A}] \quad (3.7)$$

$$I_{Lmax} = \frac{I_o}{2} + \frac{\Delta I_L}{2} \quad [\text{A}] \quad (3.8)$$

$$I_{Lmin} = \frac{I_o}{2} - \frac{\Delta I_L}{2} \quad [\text{A}] \quad (3.9)$$

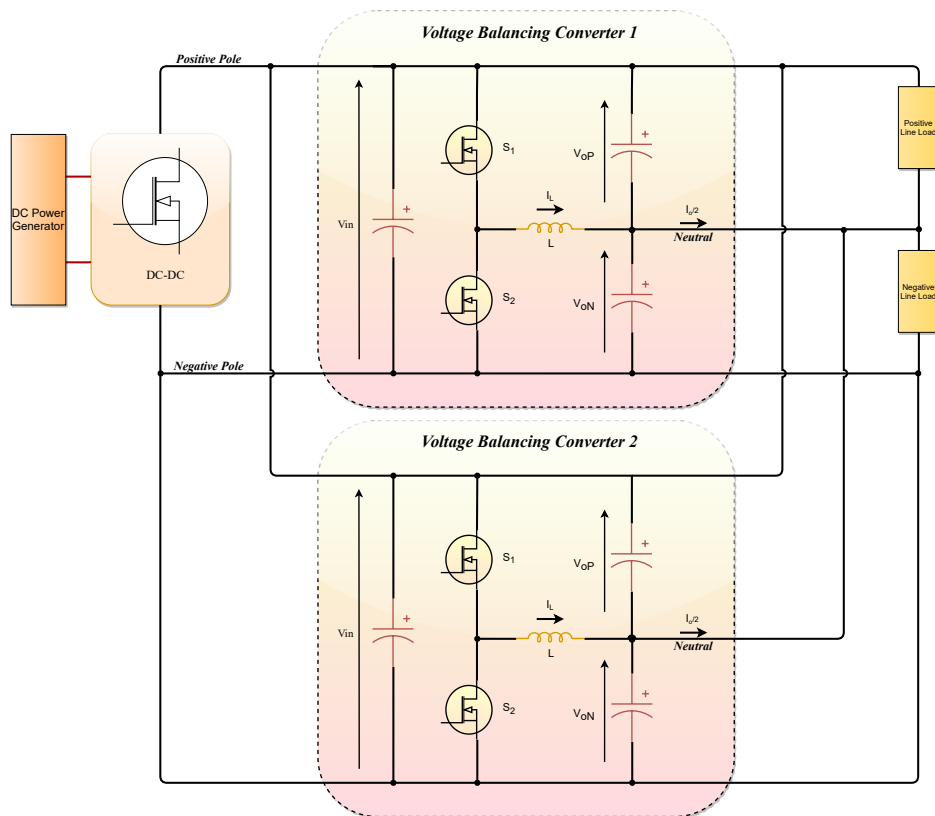


Figure 3.4: The model of a two phase interleaved balancing converter.

### 3.2.2 Bidirectional operation & inverse power flow

The synchronous half bridge of the designed voltage balancing converter offers the ability to transfer power in both directions. This capability is of utmost importance for the modern DC Microgrids, because bidirectional loads can supply power back to the distribution grid if needed. A typical example of such a case is the battery storage systems of an electric vehicle. To do so, the input and one output of the converter must be substituted, connecting a power supply to one of the former outputs of the converter and a load or the distribution grid to the previous input. The following paragraphs explain the basic tenets of this mode, for a two-phase interleaved converter.

In this section, the duty cycle is defined as the switch-on time of the low-side semiconductor ( $S_2$ ). For the inverse power flow mode of the balancing converter, a DC power source/ battery system is connected between the neutral and the negative line, while a DC load is placed in the other phase of the bipolar grid (positive). Finally, the distribution grid is connected between the positive and the negative line (former input of the balancing converter). The Figure 3.5(a) depicts the above mentioned changes. For sake of simplicity, the converter is split in two independent configurations, one which outputs power to the distribution grid and one which supplies power to the positive line load. The first configuration forms a boost converter (Figure 3.5(b)), while the second configuration is a buck-boost converter (Figure 3.5(c)). The next paragraphs provide independent analysis of the converters in a two-phase interleaved topology. Finally, the results are combined, in order to provide the total model of the currents and voltages on the main components of the Voltage Balancing Converter during inverse power flow.

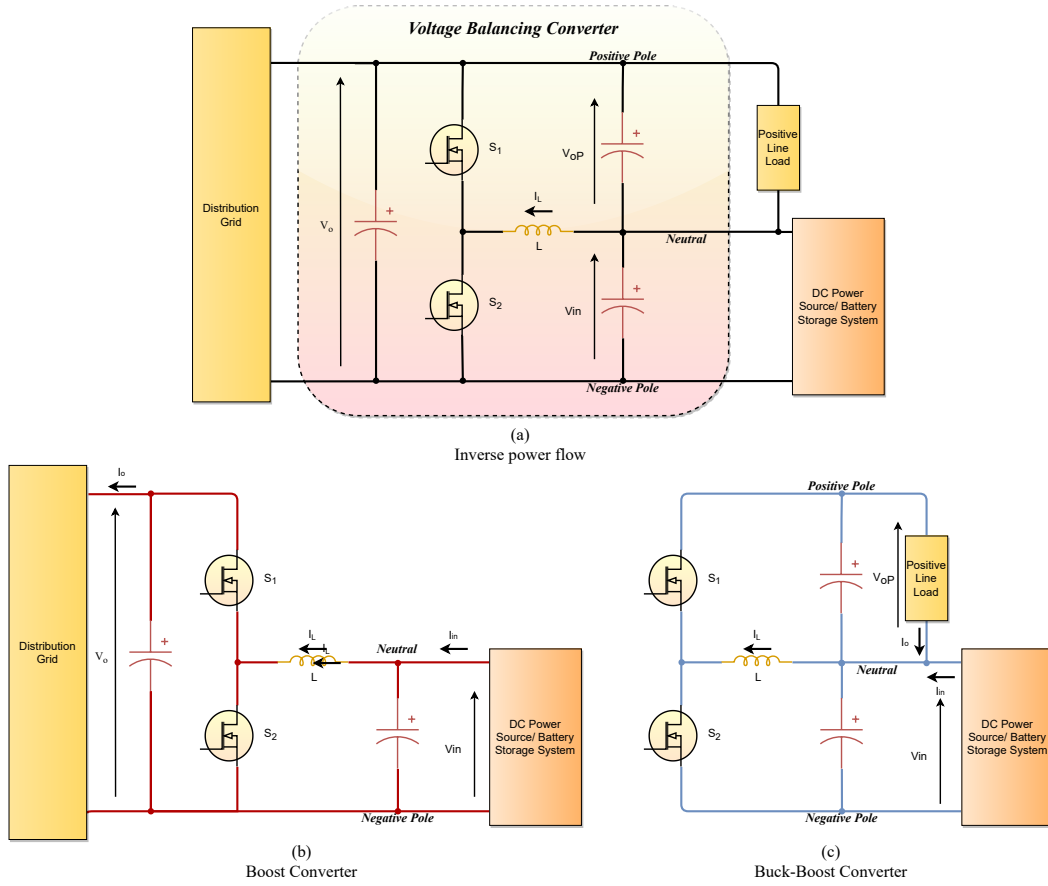


Figure 3.5: Inverse power flow mode (a) and the models of the formed boost (b) and buck-boost (c) converters.

### Boost Converter

The boost converter that is formed operates in CCM, since a synchronous half-bridge is used. The semiconductor element  $S_2$ , switches on and off with duty cycle  $D$ . The duty cycle determines the output voltage (distribution grid side) according to the equation:

$$V_o = \frac{V_{in}}{1-D} \quad [\text{V}] \quad (3.10)$$

The average inductor current of the two-phase interleaved boost converter is equal to the half of the average input current. Hence, the average inductor current and the inductor current ripple are:

$$\bar{I}_L = \frac{I_{in}}{2} = \frac{I_o}{2(1-D)} \quad [\text{A}] \quad (3.11)$$

$$\Delta I_L = I_{Lmax} - I_{Lmin} = \frac{V_{in}DT_s}{L} \quad [\text{A}] \quad (3.12)$$

The equations of the maximum and minimum inductor current values are provided from the substitution of the Equation (3.11) to the Equation (3.12):

$$I_{Lmax} = \frac{I_o}{2(1-D)} + \frac{\Delta I_L}{2} \quad [\text{A}] \quad (3.13)$$

$$I_{Lmin} = \frac{I_o}{2(1-D)} - \frac{\Delta I_L}{2} \quad [\text{A}] \quad (3.14)$$

where  $I_o$  is the current that flows towards the distribution grid from the output of the boost converter.

### Buck-Boost mode

The other output of the voltage balancing converter, which is used to connect a DC load is supplied by a buck-boost converter. The switching semiconductor component of this converter is the  $S_1$ . The duty cycle of the converter is  $D' = 1 - D$  and the output voltage (positive line of the bipolar grid) is:

$$V_{oP} = V_{in} \frac{D'}{1 - D'} = V_{in} \frac{1 - D}{D} \quad [\text{V}] \quad (3.15)$$

The average inductor current of the interleaved buck-boost converter is half of the sum of input and output average current. The following equations are used to calculate the average inductor current and its current ripple:

$$\bar{I}_L = \frac{I_o + I_{in}}{2} = \frac{I_o}{2(1 - D')} = \frac{I_o}{2D} \quad [\text{A}] \quad (3.16)$$

$$\Delta I_L = I_{Lmax} - I_{Lmin} = \frac{V_{in} D' T_s}{L} = \frac{V_{in}(1 - D) T_s}{L} \quad [\text{A}] \quad (3.17)$$

Substituting the Equation (3.16) to the Equation (3.17), the equations of the maximum and minimum inductor current are extracted:

$$I_{Lmax} = \frac{I_o}{2(1 - D')} + \frac{\Delta I_L}{2} = \frac{I_o}{2D} + \frac{\Delta I_L}{2} \quad [\text{A}] \quad (3.18)$$

$$I_{Lmin} = \frac{I_o}{2(1 - D')} - \frac{\Delta I_L}{2} = \frac{I_o}{2D} - \frac{\Delta I_L}{2} \quad [\text{A}] \quad (3.19)$$

where  $I_o$  is the current that flows through the DC load that is connected between the positive line and the neutral.

### Combined inverse mode

The merging of the previous conclusions provides the complete picture of Voltage Balancing Converter under inverse mode. Based on the principal of superposition, the total average current that flows through each one of the components of the converter is equal to the sum of the average currents that flow in each of the boost and the buck-boost converters, independently:

$$\bar{I}_L = \bar{I}_{L_{Boost}} + \bar{I}_{L_{Buck-Boost}} = \frac{I_{o_{Boost}}}{2(1 - D)} + \frac{I_{o_{Buck-Boost}}}{2D} \quad [\text{A}] \quad (3.20)$$

$$I_{Lmax} = \bar{I}_L + \frac{\Delta I_L}{2} \quad [\text{A}] \quad (3.21)$$

$$I_{Lmin} = \bar{I}_L - \frac{\Delta I_L}{2} \quad [\text{A}] \quad (3.22)$$

## 3.3 Specifications

Among the goals of this thesis project is the design and testing of a Voltage Balancing Converter, which will be connected to the load side of a DC Microgrid, creating a bipolar grid. The manufactured topology is able to provide balancing for loads which differ up to 3.68kW. It is important to clarify that this is not the actual power of the connected loads. That depends on the power capacity of the positive and the negative line.

Some of the nominal specifications of the converter are determined according to the proposed standards from the literature review for the DC Microgrids. Specifically, the voltage difference between positive and negative line ( $V_{in}$ ), should be close to 700V. Furthermore, the output voltage per phase of the converter can range from 320-400V, with the most prominent value, that of 350V. Other limits are the outcome of a comparison among several factors like the cost of the components, the efficiency optimization and the ability to find 'off-the-shelf' products which will be able to cover the needs of such an application. For example, the current rating of the device was a compromise among the inductance value, the saturation current rating and the range of the switching frequency. In particular, in order to reduce the inductor current ripple, either the inductance value must be increased or the switching frequency. Nevertheless, the switching frequency affects the switching losses in the semiconductor components and the core losses of the inductor. On the other hand, it is not always easy to find a mass production inductor with high saturation current limit and big inductance value. Finally, it is clear that the duty cycle must be close to 50% in order to produce balanced bipolar grid voltages.

The converter that was constructed has the following nominal specifications:

Table 3.1: Nominal specifications of the Voltage Balancing Converter.

Specifications	Description	Value
$P$	Maximum Power Imbalance between the Positive and Negative Phase	3.68 kW
$V_{in}$	Nominal Input Voltage between Positive and Negative Line	700 V
$V_{oP}$	Nominal Output Voltage of Positive Phase	350 V
$V_{oN}$	Nominal Output Voltage of Negative Phase	-350 V
$I_{oP}$	Maximum Output Current of Positive Phase	10.5 A
$I_{oN}$	Maximum Output Current of Negative Phase	10.5 A
$D$	Duty Cycle	47-54 %
$f_s$	Switching Frequency	180-650 kHz

The following table presents the absolute maximum ratings of the device, that are tolerated by the components, if different control strategies are combined with active cooling or if they are applied for a short period. This, implies that the switching frequency must be very high and that it will not be always possible to apply ZVS techniques. The absolute maximum voltage of the device is 800V, because it is 200V lower than the maximum blocking voltage of the semiconductor element that was used (1000V), introducing a safety margin of 20%:

Table 3.2: Absolute Maximum ratings.

Specifications	Description	Value
$V_{in}$	Input Voltage between Positive and Negative Line	800 V
$I_{oP\text{ or }N}$	Nominal Output Current of Positive or Negative Phase	14.5 A
$f_s$	Switching Frequency	650-900 kHz

### 3.4 Schematic overview

The components that were chosen for the construction of the Voltage Balancing Converter and their basic functionality will be presented in the following paragraphs. Furthermore, the general overview of the design process will be shown. The design of the converter was divided in multiple sub-parts, each one of them with different purpose. The [Figure 3.6](#) illustrates the general schematic overview of

the VBC. The main parts of the converter are highlighted, with different colors.

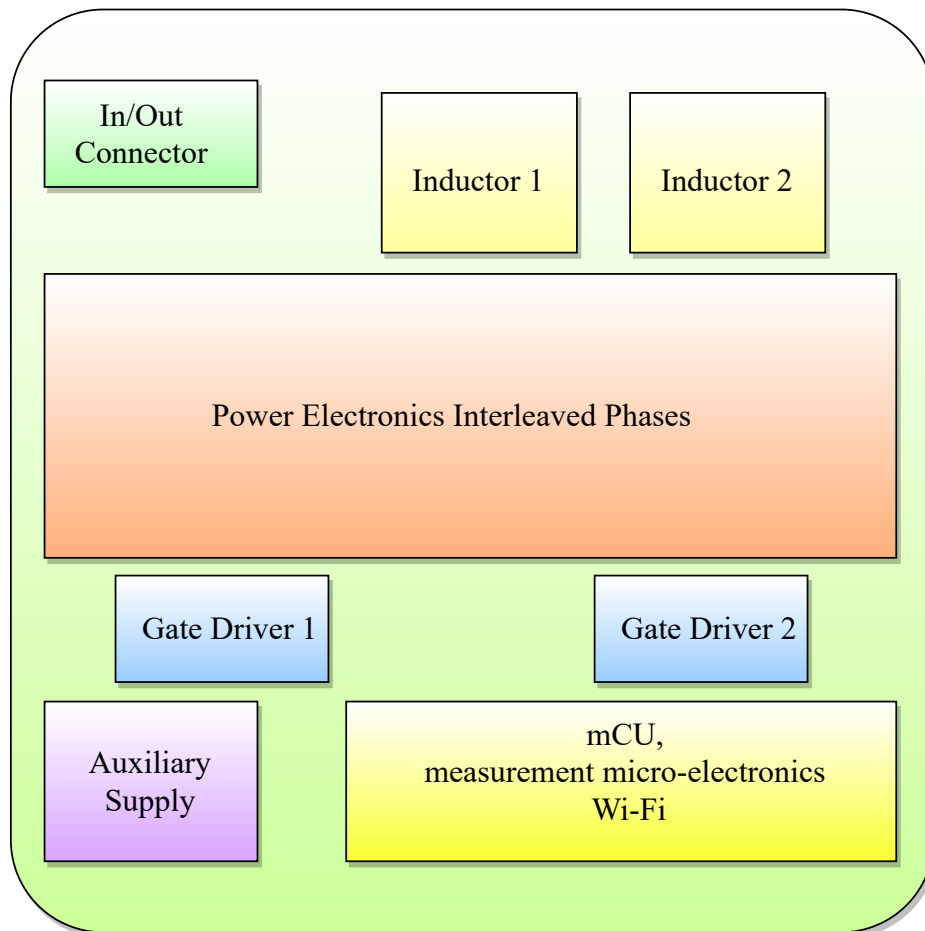


Figure 3.6: The general schematic overview of the Voltage Balancing Converter.

The converter consists of two interleaved phases of half-bridge and inductor. The semiconductor components that were chosen were the SiC mosfets. The input and the output of the converter differ only in the neutral, which is only part of the output. The input power is directed to the two-interleaved half-bridges. The half-bridges are controlled by a micro-Controller Unit ( $\mu CU$ ), which regulates the duty cycle, the dead time and the switching frequency of the converter. Several measurements of voltage and current are taken from critical points of the converter, which are stored to the  $\mu CU$ . The  $\mu CU$  is then responsible to process these data and act according to the control strategy. A Wi-Fi/Bluetooth is also integrated in the design, which allows to apply remote control to the converter and monitor the safety alerts of the device.

### 3.4.1 Design of power electronics interleaved phases

Each one of the two interleaved phases of the converter consists of two mosfets and an output filter of one inductor and capacitors. The absolute maximum voltage rating of the converter is 800V. The mosfets that are used should be able to handle at least 10-20% higher voltage. Specifically, the mosfet **C3M0065100J** from Cree was chosen. It belongs to the relatively new technology of SiC mosfets, which present significantly reduced conduction and switching losses. This product can block up to 1000V, while it can let up to 22A flow through drain and source, at 100°C, with  $R_{ds_{on}}$  of 65m $\Omega$ . One of the advantages of SiC mosfets is that they have reduced output parasitic capacitance,

compared to the silicon mosfets. This feature makes them suitable for applications with very high switching frequency, a detail which can make the design of the output filter of the converter much smaller and cheaper. In total, four mosfets are needed for each constructed converter. They make pairs of two and each pair is used to form a half-bridge.

The second part of each interleaved phase is the LC filter, which is used to absorb the harmonic content of the output voltage. It consists of a power inductor and the output capacitors. The size of this filter determines the voltage ripple in the output and the current ripple in the inductors. Overall, the calculation of the ripple is a combination of the values of these components and the switching frequency. The inductor that was placed for the design of the Voltage Balancing Converter is the [74437429203680](#) from Würth. This particular product presents adequately high inductance value (68uH) for a big range of average current, with saturation current rating of 10.7A. Three ceramic capacitors were used between each pair of lines. Each capacitor is 330nF and has a voltage rating of 500V.

The finding of the appropriate inductor was one of the most challenging parts of the design process. The majority of the "off-the-shelf" inductors of SMD technology are rated for much lower current and voltage ratings. Otherwise, a bulkier inductor had to be placed, making the design of a device that can be attached to DIN rail impossible. Hence, it became clear very soon, that a two-phase interleaved configuration was necessary, in order to divide the current between the multiple inductors. Otherwise, the available inductance values would force the converter to very high switching frequencies. The [Figure 3.7](#) illustrates the one of the two identical interleaved phases.

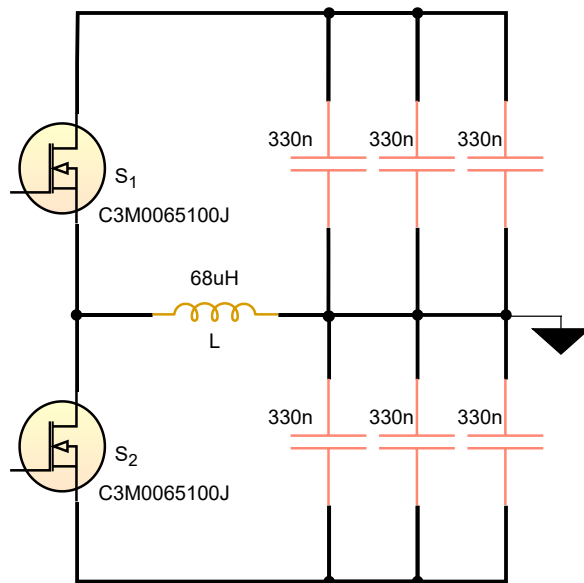


Figure 3.7: One of the two identical interleaved phases of the designed VBC.

### 3.4.2 Design of the gate drivers circuit

For the switching of the two mosfets, the gate driver [UCC21530](#) of Texas Instruments was used. One gate driver is able to control two mosfets with its two isolated outputs. The isolation between the two outputs and the input allows to use the chip for the driving of mosfets that do not have their source connected to the ground. A typical example is the high-side mosfet of the half-bridge, For this particular converter, the ground of the  $\mu CU$  and the other micro-electronic components was connected to the neutral line of the bipolar grid. As a consequence, all of the mosfets needed isolated driving.

The disadvantage of this type of gate driving is that several isolated power supplies are needed. The two low side mosfets of the converter have their source connected to the same line (negative line of the bipolar grid). Thus, one isolated power supply is enough for the driving of both of them. This supply is part of the auxiliary supply system, as it will be explained below (Section 3.4.4). On the other hand, the high side mosfets needed different supplies. To do so, a small push-pull converter was integrated next to each one of the gate drivers, providing the necessary voltage. The push-pull converter was implemented with the chip **SN6505BDBVR** from Texas Instruments and a small center-tapped transformer. Each isolated power supply provides 19V. The outputs of the gate driver were connected to the gate of the mosfets, sending the PWM pulses. In order to eliminate the danger of parasitic switching-on of the mosfets, negative gate voltage is applied to the source when it switches-off. This is done with a 4.3V clamping voltage zener diode, in parallel with a capacitor, placed right after the output of the gate driver. When this circuit is in steady-state, it pulls the source of the mosfet to -4.3V, protecting it from the high frequency ringing on the  $C_{gd}$ . Finally, a diode with the anode connected to the gate is used to bypass the regular gate resistance of  $2.2\Omega$ , accelerating the switching-off of the mosfet.

The benefit of using a gate driver with two outputs is that the design is greatly simplified. Also, any manufacturing differences of the chip that could affect the switching delay of the PWM pulses are eliminated. Finally, advanced integrated chips like the one that was used are able to introduce dead-time between the high and low pulses, even when the  $\mu CU$  fails to do so. This increases the reliability of the system. The Figure 3.8 demonstrates the aforementioned gate driving circuitry of one half-bridge.

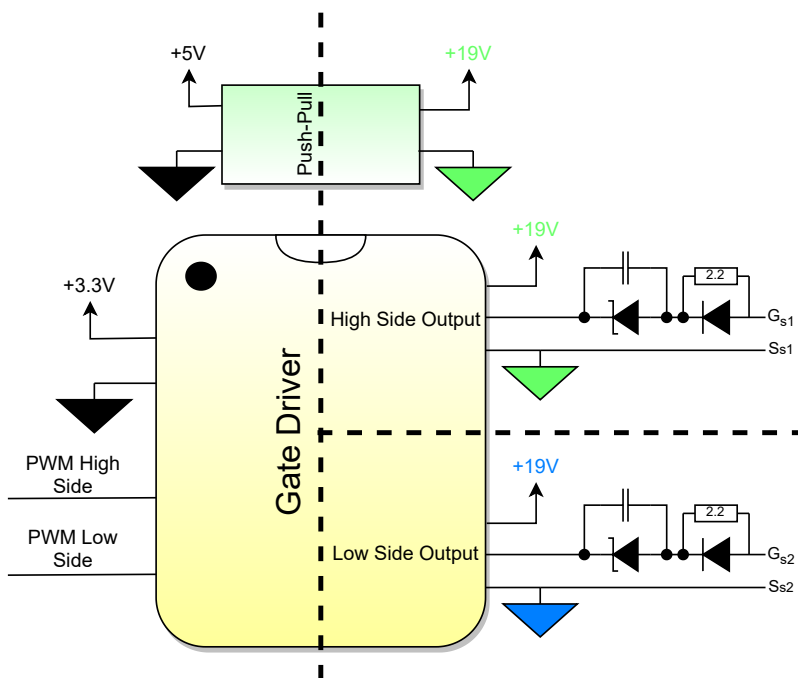


Figure 3.8: The gate driver circuits of the VBC.

### 3.4.3 Design of the micro-electronics

One of the most vital parts for the proper function of the converter is the design of the micro-electronics circuits. This part consists of several integrated chips and other components, with each one of them implementing different tasks. Overall, the micro-electronics of the specific converter that was constructed can be divided in two different categories: the  $\mu CU$  & Wi-Fi module and the micro-electronics for the measurement of important parameters.

The micro-controller that was used is the [STM32G071](#) from ST. It is a 48-pin unit with 129 kBytes of flash memory, 1 Analog-to-Digital Converter (ADC) and 4 UART communication lines. The internal crystal oscillator can run up to 48MHz, while it has 14 different timers. The  $\mu$ CU can operate with very low voltage supply, which ranges from 1.7V to 3.6V. Among the tasks of the  $\mu$ CU is the receipt of the analog measurements of the two bipolar output voltages (positive-neutral and neutral-negative) and the currents of the neutral line and of the two inductors. The micro-controller is also responsible to switch-off the device, in case of over-current in any of the two inductors. Finally, the  $\mu$ CU communicates with the Wi-Fi module [ESP32](#). The module sends and receives data with wireless communication, facilitating the control of the device.

As it was mentioned before, 5 different measurements were taken and sent to the  $\mu$ CU: the two bipolar output voltages (positive-neutral and neutral-negative) and the currents of the neutral line and of the two inductors. The voltage measurement was carried out with a series of resistors which form a voltage divider. The output of the voltage divider is filtered by an RC filter with cut-off frequency of 1.5MHz and then is sent to the ADC of the  $\mu$ CU, which converts it to the actual output voltage value. The measurement of currents was implemented with a small shunt resistor of 2.5m $\Omega$ . The differential voltage of the resistor was then introduced to the operational amplifier [OPA320](#) from Texas Instruments. The measuring points are visible in [Figure 3.9](#).

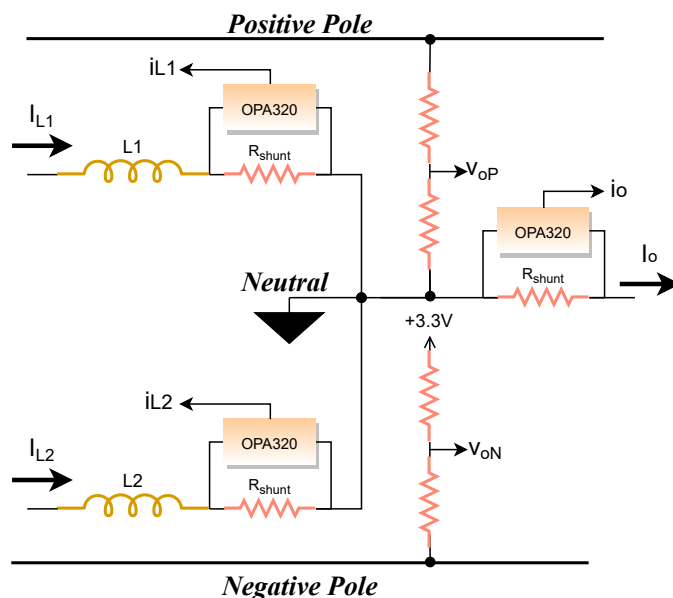


Figure 3.9: The measuring circuits and the nodes that were measured on the VBC.

#### 3.4.4 Auxiliary supply

Various voltage levels are needed to supply every electronic device of the converter. In addition, several isolated supplies are also required to supply the gate drivers of the mosfets. The most common practice that is followed for the design of power electronic converters is the integration of a small flyback converter. During the current thesis project, a flyback converter was designed in an autonomous PCB, which can be mounted on the main converter PCB.

The specific flyback which was designed, when connected to the VBC PCB, is supplied with bipolar voltage of 800V maximum. Then, it converts the input voltage to two isolated outputs of 19V each. These outputs are transferred to the micro-electronic devices of the main converter and to the other small power converters. The integrated chip [UCC28740](#) from Texas Instruments controls the duty cycle and the switching frequency of the flyback, sending PWM pulses to the SiC mosfet [C2M1000170J](#). The particular mosfet blocks up to 1700V. For the conversion of the input voltage, the

transformer [WA8759-AL](#) from Coilcraft is used. The transformer has two secondary windings with turns-ratio of 1:0.083 and an auxiliary winding which feeds the output voltage back to the IC, until it reaches the desirable output voltage. An optocoupler [TCLT1004](#) is also used, providing feedback to the flyback controller. This is the first version of flyback that was designed and tested. The testing of this version showed that the leakage inductance of the primary winding has a great impact on the voltage feedback trace of the IC. Because of inexperience on the PCB layout making of such a converter, the leakage inductance made the output voltage regulation unstable. Furthermore, the output capacitance was much lower than the recommended. The useful conclusions from the testing of the first version were later corrected with the making of the second version.

The next part of the auxiliary supply is the conversion of the 19V of one of the outputs to 5V and 3.3V for the micro-electronic devices. Specifically, a small buck converter, integrated in a chip, converts the 19V to 5V. This is supplied to the push-pull IC that powers the high-side mosfet gate driving circuits. Afterwards, the 5V is converted to 3.3V through a LDO device. The last voltage level is necessary for almost all of the electronic devices: the  $\mu CU$ , the Wi-Fi module, the operational amplifiers and the gate drivers. Finally, the other output of the flyback converter is used to power the low-side gate driving circuit. The [Figure 3.10](#) shows an overview of the auxiliary supply system.

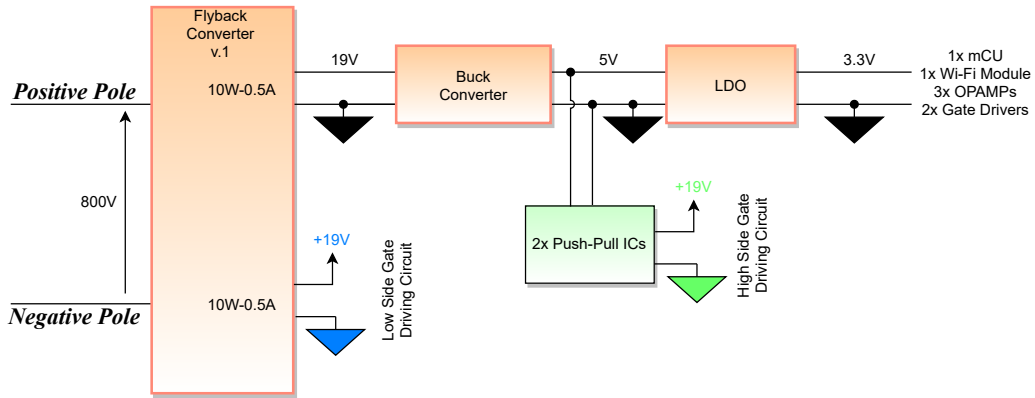


Figure 3.10: The overview of the auxiliary supply of the VBC.

## 3.5 Control strategy

The aim of a Voltage Balancing Converter is to keep the positive and negative voltages of the bipolar grid inside the acceptable limits. However, this must be done with respect to the safety limits of the topology and the components that are used. Overall, the control strategy that was followed, combines the output voltage regulation with zero voltage techniques. A proportional-integer (PI) control algorithm is applied, which reacts to any unbalance between the positive and the negative loads. Simultaneously, the use of a synchronous half-bridge permits the implementation of passive ZVS techniques, that rely on the bidirectional current of the inductor, for a big range of operation. This eliminates the switching losses on the mosfets. The following subsections present the two different targets of the control both as independent strategies, as well as combined.

### 3.5.1 Droop control of the output voltage

In order to effectively control the output voltage of the converter and make it able to react to any change in the load side, a PI control is implemented. This algorithm is controlled by the  $\mu CU$ , which determines the duty cycle of the converter. This decision is based upon the measurement of the output current and voltages. Specifically, the positive and negative output voltages are measured. A margin of  $\Delta V$  is allowed between positive and negative line. This margin ranges from  $\frac{V_{oP}}{V_{oN}} = 0.95 - 1.05$

for the specific application. In the future, when the DC distribution grid standards are set, these values might be different. Afterwards, this ratio is used to calculate the reference value of the output current, which is then deducted from its actual value that is measured. The error is then introduced to a PI controller which outputs the new duty cycle, which is applied then to the converter. When the converter output current reaches  $\pm 10.5\text{A}$ , the control must be able to prevent it from further increase. Otherwise, the inductors will enter to the saturation region. The Figure 3.11 illustrates the overview of the implemented PI control.

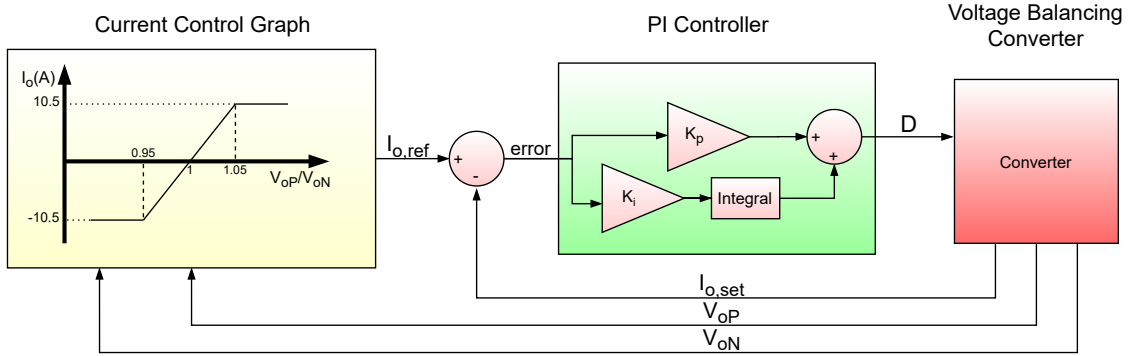


Figure 3.11: The overview of the PI control in the VBC.

### 3.5.2 Zero Voltage Switching technique

The technique of zero voltage switching (ZVS) is used to reduce or minimize the switching losses during the commutation of the semiconductor elements of the converter. To do so, the technique relies on the bidirectional inductor current. Specifically, during dead time the inductor current will attempt to flow through the mosfet that is not on yet. Before the body diode of this mosfet begins to conduct, the  $C_{oss}$  will be fully discharged. Simultaneously the  $C_{oss}$  of the other mosfet charges up to the input voltage level. When this procedure is over, the inductor current flows through the body diode. From this moment and afterwards, the switching-on of the mosfet will not cause losses, because its  $V_{ds} = 0$ .

It is crucial that the inductor has enough energy stored during the dead time, to discharge the  $C_{oss}$  of the mosfet. Otherwise, the parasitic capacitor will be partially or not at all discharged. Nevertheless, particular attention must be paid on the peak values of the inductor current, so that it is not led to saturation.

Besides the PI control, a frequency control is needed in order to keep the inductor peak values below the saturation limit. As it was explained before, the output current is split between the two inductors. The maximum absolute value that the current of the inductor can reach is:  $|\hat{I}_L| = \left| \frac{I_o}{2} + \frac{\Delta I_L}{2} \right|$ . Controlling the switching frequency allows to determine the magnitude of the  $\Delta I_L$ . Since, the inductor value is know, the  $\mu CU$  is able to set the proper switching frequency value, that will make the inductor current change its direction, in order to achieve ZVS. It is apparent that, the more balanced the loads, the lower the output current. Hence, the  $\Delta I_L$  is smaller, which translates to lower ripple in order to change direction. In other words, higher frequency is needed. The frequency control is depicted in the Figure 3.12.

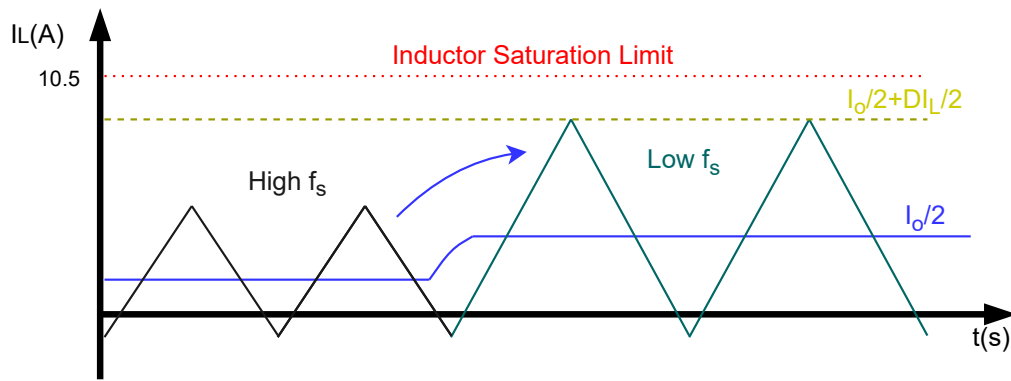


Figure 3.12: The overview of the frequency control in the VBC.

## CHAPTER 4

# ANALYSIS & DESIGN OF THE MAXIMUM POWER POINT TRACKING CONVERTER

*The progress of the PV sector depends on the design of efficient MPPT converters. New topologies are proposed that are about to fundamentally transform the present converters capabilities.*

### 4.1 Introduction

The maximum power point tracking converter that was designed is connected to two independent strings of PV modules. The goal of this topology is to monitor the input current and voltage that is supplied from the PV strings. Based on this information, the control algorithm of the converter determines the desirable output voltage and current, that will force the PV to produce the maximum amount of power.

As it was discussed in [Section 2.1.2](#), several topologies are proposed for the connection of the PV modules. The most commonly used topology is the distributed at PV string level because it minimizes the impact of partial shading and power degradation, with less money spent for power electronic equipment compared to the distributed at PV module level configuration [12]. One of the main goals of this thesis project is the design and testing of a MPPT converter, suitable for distributed at string level configurations. In addition, the output of the designed converter is capable to be directly connected to a bipolar DC distribution grid. This is a feature that will raise a lot of interest over the next years, as the bipolar DC distribution grids and the Microgrids expand.

### 4.2 Theoretical analysis of the converter

The purpose of this section is the in-depth analysis of the theoretical background of the topology. The fundamental equations that provide the current and voltage in some of the most critical points of the converter are shown and explained. Moreover, the different steps of conversion of a period are presented and analyzed.

The introduced topology has two independent inputs. Each one of the inputs is connected to a different string of PV modules. On the other side, the output consists of three lines (positive, neutral and negative), that feed power to the distribution grid or a Microgrid. A string of power electronics are used in order to implement the power conversion. For the designed topology, two diodes and two

mosfets are placed for the formation of this string. One inductor is connected between each input and the power electronics string. Capacitors absorb the harmonic content of the output voltage, producing stepped-up DC voltage. The converter overview is illustrated in Figure 4.1.

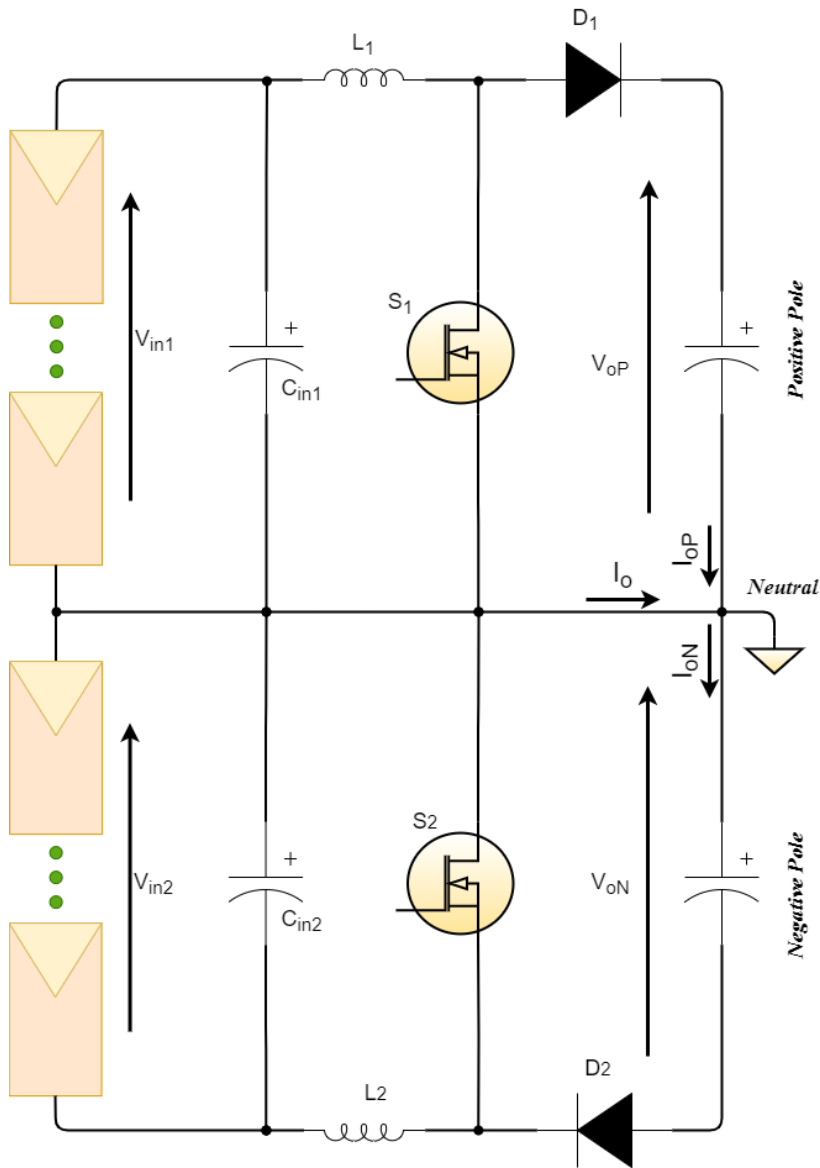


Figure 4.1: The model of the designed MPPT converter.

For sake of simplicity, the designed topology will be approached as two independent boost converters. Each converter consists of one input, one inductor and a pair of mosfet-diode. Each one of the converters operates under its own duty cycle ( $D_1$  and  $D_2$ ) and its own switching frequency ( $f_{s1}$  and  $f_{s2}$ ).

For the rest of this section, only the top part of the converter will be taken into account, analyzed in CCM, unless otherwise specified. In any case, the analysis holds for the other part of the converter, for its own duty cycle and switching frequency. In order to use the following equations for the bottom part, the indicator of 1 and the bipolar phase indicator  $P$  must be converted to 2 and  $N$  respectively and vice versa.

The voltage on the inductor of the converter is:

$$V_{L1_{t:0 \rightarrow D_1 T_{s1}}} = V_{in1} \quad [\text{V}] \quad (4.1)$$

$$V_{L2_{t:D_1 T_{s1} \rightarrow T_{s1}}} = V_{in1} - V_{oP} \quad [\text{V}] \quad (4.2)$$

In steady-state situation the average voltage of the inductor is 0. Hence, the area that is formed above 0 is equal to the area that lies below. This way, the duty cycle equation is determined for CCM:

$$\begin{aligned} V_{in1} D_1 T_{s1} &= (V_{oP} - V_{in1})(T_{s1} - D_1 T_{s1}) \Rightarrow \\ V_{oP} &= \frac{V_{in1}}{1 - D_1} \quad [\text{V}] \end{aligned} \quad (4.3)$$

Similarly, in the case of the bottom side converter:

$$V_{oN} = \frac{V_{in2}}{1 - D_2} \quad [\text{V}] \quad (4.4)$$

The ripple of the inductor current is:

$$\Delta I_{L1} = \frac{V_{in1} D_1 T_{s1}}{L_1} \quad [\text{A}] \quad (4.5)$$

$$\Delta I_{L2} = \frac{V_{in2} D_2 T_{s2}}{L_2} \quad [\text{A}] \quad (4.6)$$

The average current of the inductor is equal to the average input current, since they are in series. When the mosfets are on, the corresponding output capacitor of each mosfet absorbs the inductor current ripple. Based on the above, the average output current is equal to the average inductor current, for as long as the mosfet is switched-off:

$$\bar{I}_{L1} = \frac{I_{oP}}{1 - D_1} \quad [\text{A}] \quad (4.7)$$

$$\bar{I}_{L2} = \frac{I_{oN}}{1 - D_2} \quad [\text{A}] \quad (4.8)$$

while the peak value of the inductor current is:

$$\left| \hat{I}_{L1} \right| = \left| \bar{I}_{L1} + \frac{\Delta I_{L1}}{2} \right| \quad [\text{A}] \quad (4.9)$$

$$\left| \hat{I}_{L2} \right| = \left| \bar{I}_{L2} + \frac{\Delta I_{L2}}{2} \right| \quad [\text{A}] \quad (4.10)$$

### 4.2.1 Interleaved configuration

Particular interest is given again to the integration of interleaved configuration to the design of the converter. The benefit of such a design is once again the sharing of the current among the inductors of each interleaved phase. For the specific topology, one more string of power electronics and two inductors are added. The same side mosfets of each interleaved phase operate with phase shift of  $180^\circ$ . Similar to the VBC, the average current of each inductor is now the half:

$$\bar{I}_{L1} = \frac{I_{oP}}{2(1 - D_1)} \quad [\text{A}] \quad (4.11)$$

$$\bar{I}_{L2} = \frac{I_{oN}}{2(1 - D_2)} \quad [\text{A}] \quad (4.12)$$

### 4.2.2 Coupled inductors

The coupled inductors are capturing more and more the attention of power converters designers. The merits they bring to the system are valuable. They are suitable for applications that include multiple inductors, using common cores for several magnetics. The theory of coupled inductors will be presented in this subsection, adjusted for the case of the two-phase interleaved MPPT converter that was designed and tested for this thesis project. The four inductors of the converter were combined in groups of two in the same core. Each group consists of the two inductors that are on the same side of the two interleaved phases. The Figure 4.2 illustrates the designed topology.

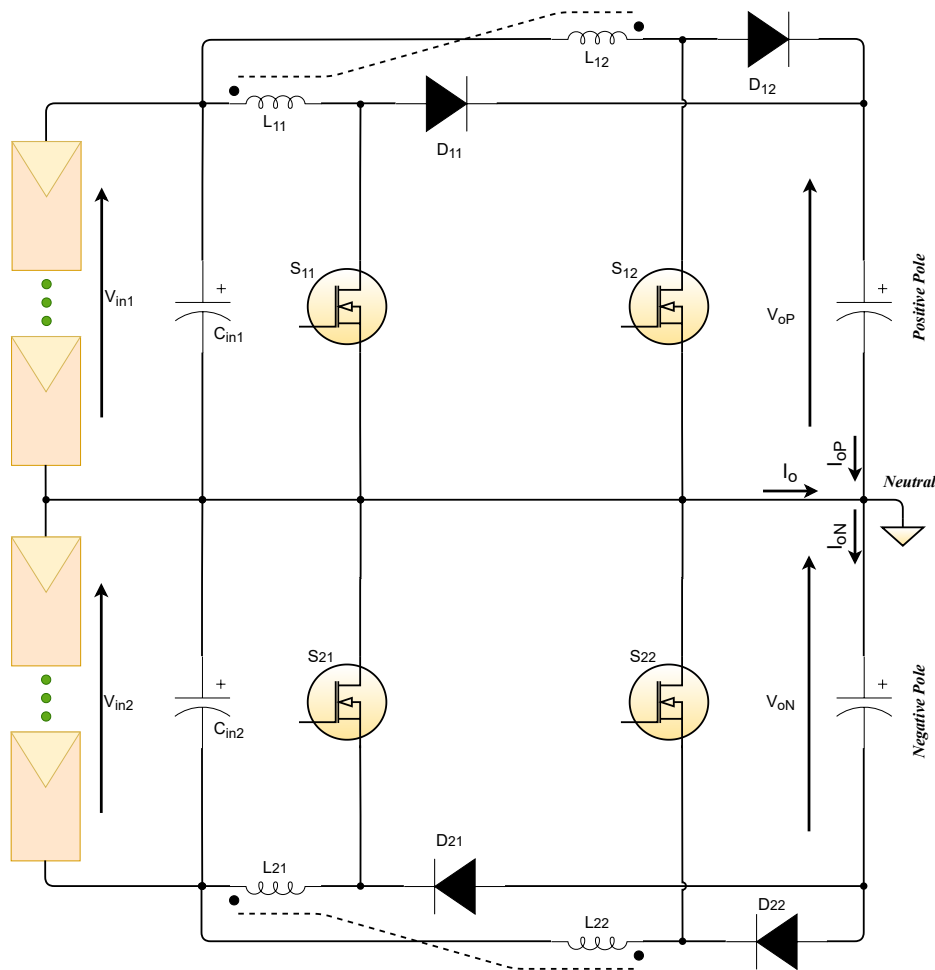


Figure 4.2: The overview of the coupled inductors in inverse coupling, in a two phase interleaved MPPT converter.

For the rest of this section, the analysis will be focused on the pair of coupled inductors  $L_{11}$  and  $L_{12}$  and the semiconductors of the top part of the converter ( $S_{11}$ ,  $D_{11}$ ,  $S_{12}$  and  $D_{12}$ ). Given that these inductors are in the same spot of different interleaved phases, they operate under the same duty cycle  $D$  and the same switching period  $T_s$ . In order to use the following equations for the other part of the converter, the indicator of 1 and the bipolar phase indicator  $P$  must be converted to 2 and  $N$  respectively and vice versa.

Compared to the independent inductors, the coupled bring faster transient response and higher effective inductance when the coupling coefficient is carefully optimized. Furthermore, the ripple of the inductor current and of the output voltage are reduced. Simultaneously, the core losses are diminished, using less material for the core [36]. The two most commonly used configurations of

coupled inductors are the direct coupling and the inverse coupling. In the first one, the current enters to both the inductors from the side of the dot, while in the other option, it enters from opposite sides. The coupling coefficient is:

$$\kappa = \frac{M}{\sqrt{L_{11}L_{12}}} \quad (4.13)$$

where  $M$  is the mutual inductance and  $L_{11}, L_{12}$  are the self-inductances of the two coupled inductors. The  $\kappa$  is positive for direct coupling and negative for inverse coupling. The Figure 4.3 shows a pair of coupled inductors with inverse coupling and a pair with direct coupling, with the lines of the magnetic flux in the core.

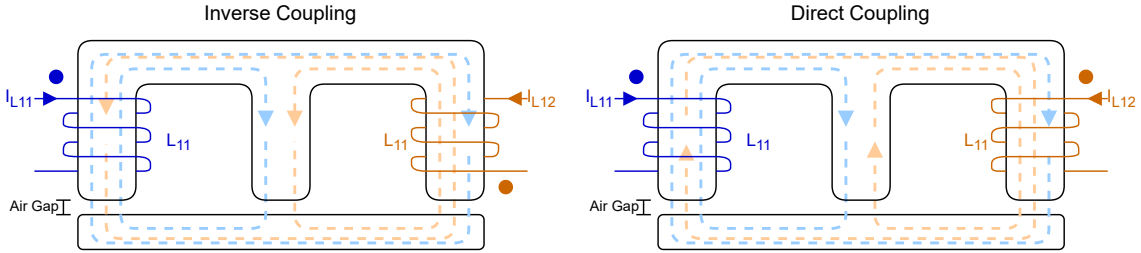


Figure 4.3: The overview of two pairs of coupled inductors in inverse and in direct coupling.

The induced voltages between the two coupled inductors can be modelled with the equivalent circuit of a controlled voltage source, in series with the leakage inductance of each individual inductor. The controlled voltage source of the one inductor is equal to the coupling coefficient, multiplied with the applied voltage of the other inductor:  $V_{L_{11}ctr} = \kappa V_{L_{12}}$ . The total voltage of  $V_{L_{11}} = V_{L_{11}ctr} + V_{L_{k11}}$ , where  $V_{L_{k11}} = (1 - \kappa)L_{11}$  is the leakage inductance of the same inductor [37]. In the case of the most power electronics converters, there are a few and very specific voltage levels that are applied to the inductors. These levels usually depend on which semiconductor is switched on at that particular moment. For the specific MPPT that was tested, there are four different scenarios which happen with the following sequence:

1. The  $S_{11}$  switch is ON, while the  $S_{12}$  is OFF.
2. For  $D < 0.5$ , both switches are off, while for  $D > 0.5$ , both of them are on.
3. The  $S_{11}$  switch is OFF, while the  $S_{12}$  is ON.
4. The second scenario repeats.

In general, if the mosfet  $S_{11}$  is on or off, then the voltage on the inductor  $L_{11}$  is:

$$V_{L_{11}} = V_{in1}, \text{ when it is ON [V]} \quad (4.14)$$

$$V_{L_{11}} = V_{in1} - V_{oP}, \text{ when it is OFF [V]} \quad (4.15)$$

The fundamental equations of coupled magnetics are:

$$V_{L_{11}} = L_{11} \frac{di_{L_{11}}}{dt} + M \frac{di_{L_{12}}}{dt} \quad [V] \quad (4.16)$$

$$V_{L_{12}} = L_{12} \frac{di_{L_{12}}}{dt} + M \frac{di_{L_{11}}}{dt} \quad [V] \quad (4.17)$$

Rearranging the terms of Equation (4.13), Equation (4.14), Equation (4.15), Equation (4.16) and Equation (4.17) and assuming that the two coupled inductors have the same self-inductance  $L$ , it can

be found that the effective inductance of every coupled inductor at each particular time frame of a switching period is: [36]:

$$L_{eq1} = \frac{1 - \kappa^2}{1 + \frac{D}{1-D}\kappa} L \quad [\text{H}] \quad (4.18)$$

$$L_{eq2} = (1 + \kappa)L \quad [\text{H}] \quad (4.19)$$

$$L_{eq3} = \frac{1 - \kappa^2}{1 + \frac{1-D}{D}\kappa} L \quad [\text{H}] \quad (4.20)$$

where  $D$  is the duty cycle of the converter,  $L$  is the self-inductance of each coupled inductor and  $\kappa$  is the coupling coefficient. The  $L_{eq1}$  is the effective inductance, during the first item of the scenario list. Similarly, the  $L_{eq3}$  is the effective inductance, during the third item of the list and  $L_{eq2}$  is the effective inductance during the second and the fourth scenario. Further analysis of the above equations shows that in the case of direct coupling ( $\kappa > 0$ ), the effective inductance is always smaller than the self-inductance  $L$ . Contrary, when inverse coupling is used ( $\kappa < 0$ ), there is a range of duty cycles for which the effective inductance is larger than the self-inductance. This feature can be used to reduce the current ripple and the core losses. Specifically, the effective inductance in inverse coupling is higher than the self-inductance when:

$$\kappa > -\frac{D}{1-D}, \quad \text{when } D < 0.5 \quad (4.21)$$

$$\kappa > -\frac{1-D}{D}, \quad \text{when } D > 0.5 \quad (4.22)$$

When the  $D$  is below 0.5, the  $L_{eq1}$  can be used to determine the current ripple of each coupled inductor. On the other hand, when  $D > 0.5$ , the  $L_{eq3}$  must be used. The following equations provide the inductor current ripple in every case:

$$\Delta I_{L11} = \frac{V_{in1} D T_s}{L_{eq1}}, \quad \text{when } D < 0.5 \quad [\text{A}] \quad (4.23)$$

$$\Delta I_{L11} = \frac{(V_{in1} - V_{oP})(1-D)T_s}{L_{eq3}}, \quad \text{when } D > 0.5 \quad [\text{A}] \quad (4.24)$$

The following graphs (Figure 4.4 and Figure 4.5) depict the currents of the two inverse coupled inductors, with the equivalent inductance of each time region. It is clear that the peak-to-peak current ripple of the inductors is given from  $L_{eq1}$ , for  $D < 0.5$  and from  $L_{eq3}$ , for  $D > 0.5$ .

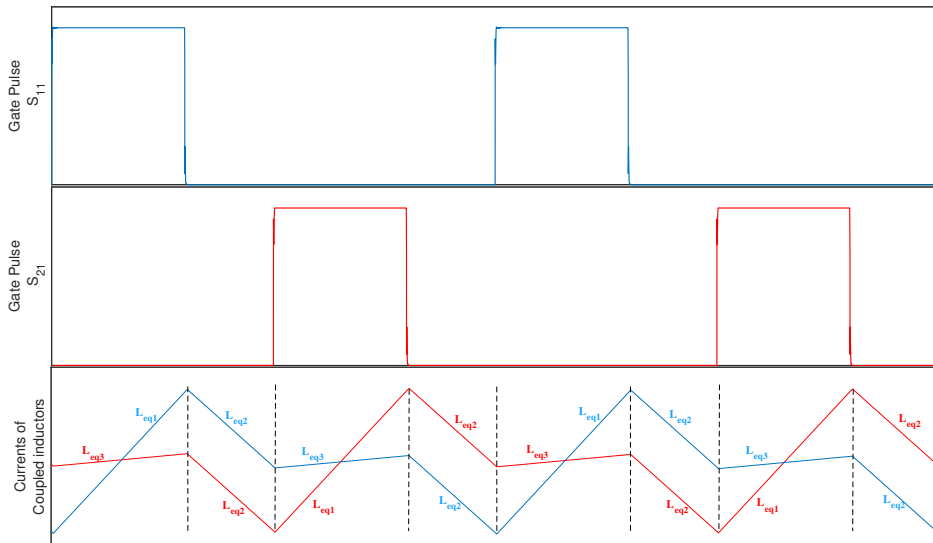
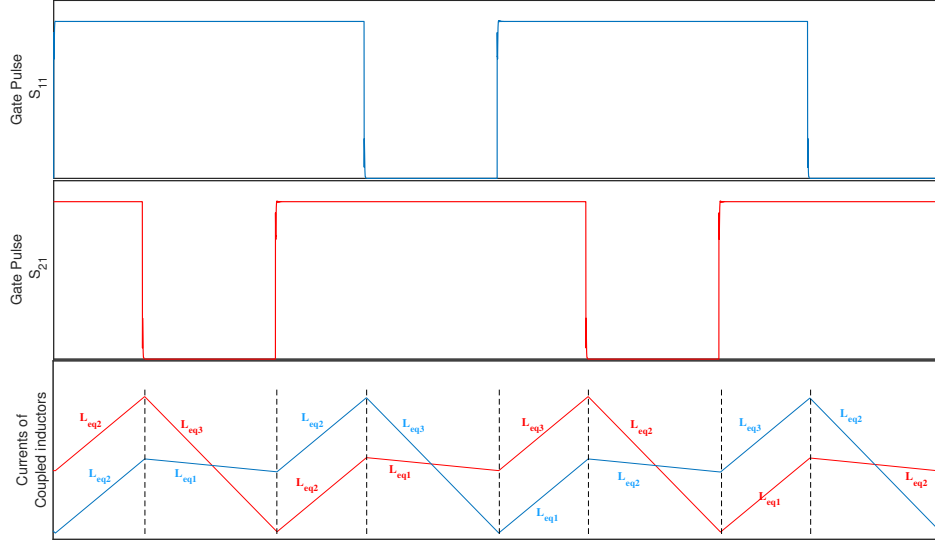


Figure 4.4: The plots of the currents of the two inverse coupled inductors for  $D < 0.5$ .


 Figure 4.5: The plots of the currents of the two inverse coupled inductors for  $D > 0.5$ .

### Optimization of coupling coefficient

One of the main advantages that the coupled inductors bring is the lowering of their current ripple. A comparison of coupled and uncoupled inductors follows, in order to determine how they affect their current ripple, as well as the output ripple, based on  $L$  [38]. As output current ripple is defined: the sum of the two interleaved inductors, before that ripple is absorbed by the output capacitors. The comparison is adjusted for the designed MPPT converter. In the case of uncoupled inductors ( $uc$ ) with  $D < 0.5$  are, where  $S_{11}$  is ON and  $S_{12}$  is OFF and equal inductances  $L$ :

$$\begin{aligned} \frac{\Delta i_{L11uc}}{\Delta t} &= \frac{V_{in1}}{L} \xrightarrow{\Delta t=DT_s} \\ \Delta I_{L11uc} &= \frac{V_{in1}DT_s}{L} \quad [\text{A}] \end{aligned} \quad (4.25)$$

$$\begin{aligned} \frac{\Delta i_{L12uc}}{\Delta t} &= \frac{V_{in1} - V_{oP}}{L} \xrightarrow{\Delta t=DT_s} \\ \Delta I_{L12uc} &= \frac{(V_{in1} - V_{oP})DT_s}{L} \quad [\text{A}] \end{aligned} \quad (4.26)$$

The current ripple in the output of the system is:

$$\Delta I_{oPuc} = \Delta I_{L11uc} + \Delta I_{L12uc} = \frac{V_{in}DT_s}{L} \frac{1-2D}{1-D} \quad [\text{A}] \quad (4.27)$$

The previous analysis holds also for the case of coupled inductors ( $c$ ). To do so, the self-inductance  $L$  is substituted with the equivalent inductance. In a scenario where  $D < 0.5$  and  $S_{11}$  is ON for time  $DT_s$ , the inductance of  $S_{11}$  is substituted by  $L_{eq1}$  and the inductance of  $S_{12}$  by  $L_{eq3}$ , since it is OFF. The current ripples are:

$$\begin{aligned} \frac{\Delta i_{L11c}}{\Delta t} &= \frac{V_{in1}}{L_{eq1}} \xrightarrow{\Delta t=DT_s} \\ \Delta I_{L11c} &= \frac{V_{in1}DT_s}{L_{eq1}} \quad [\text{A}] \end{aligned} \quad (4.28)$$

$$\begin{aligned}\frac{\Delta i_{L12c}}{\Delta t} &= \frac{V_{in1} - V_{oP}}{L_{eq3}} \xrightarrow{\Delta t = DT_s} \\ \Delta I_{L12c} &= \frac{(V_{in1} - V_{oP})DT_s}{L_{eq3}} \quad [\text{A}]\end{aligned}\quad (4.29)$$

The current ripple in the output of the system is:

$$\Delta I_{oPc} = \Delta I_{L11c} + \Delta I_{L12c} = \frac{V_{in}DT_s}{L(1 - \kappa^2)} \left( (1 - D)(1 + \kappa) + \frac{D}{1 - D} \right) \quad [\text{A}] \quad (4.30)$$

The aforementioned equations make clear that the coupling coefficient  $\kappa$  determines the current ripple of the inductors and of the output. Hence, it is very important to optimize the value of  $\kappa$  during the design phase of the coupling inductors. The value of  $\kappa$  must create an effective inductance that is higher than the self-inductance of the inductor, for as bigger range of duty cycles as possible [39]. This will reduce the ripple, which affects the losses of the converter. In order to find the optimal  $\kappa$  in relation to the duty cycle, the Equation (4.28) will be used. Specifically, the optimal value of  $\kappa$  occurs when the  $\Delta I_{L11c}$  is minimum. For the minimum  $\Delta I_{L11c}$ :

$$\frac{\Delta I_{L11c}}{\Delta \kappa} = 0 \Rightarrow \kappa_{opt} = \frac{-1 + D + \sqrt{1 - 2D}}{D} \quad (4.31)$$

Similar analysis can be made for  $D > 0.5$ , which leads to:

$$\kappa_{opt} = \frac{-D + \sqrt{2D - 1}}{1 - D} \quad (4.32)$$

### Summary of coupled inductors

The goal of these paragraphs are to summarize all the extracted information around the coupled inductors and the optimal design, oriented in the case of the designed MPPT converter. Overall, two different modes are usually applied: the inverse and the direct coupling. The characteristics of each mode are:

For the inverse coupling:

- For a range of different  $D$  and  $\kappa$ , it can lead to higher effective inductance, than the actual self-inductance. This produces less inductor ripple and less magnetic flux density ripple ( $\Delta B$ ), so less core losses, in the center leg of the core. For  $D = 0.5$ , the magnetic flux density ripple becomes zero, minimizing the core losses.
- Even though the ripple is less, the average magnetic flux density  $\bar{B}$  is higher compared to direct coupling, which makes it challenging to avoid the saturation limit of the core.
- The ( $\Delta B$ ) occurs in double the switching frequency  $f_s$  of the converter, which increases the core losses.

For the direct coupling:

- The effective inductance is always lower compared to an independent inductor with the same self-inductance.
- The  $\Delta B$  is higher compared to the inverse coupling, but with the same frequency as the switching of the converter.
- The  $\bar{B}$  is zero, simplifying the saturation limit design.

### 4.3 Specifications

The voltage and current ratings of the components that were used for the design of the converter were decided upon the most modern technologies of PV panels. The following table summarizes the specifications of the converter:

Table 4.1: Nominal specifications of the MPPT converter.

Specifications	Description	Value
$P$	Maximum conversion power per input	3.2 kW
$V_{in}$	Input voltage range per input	150-320V
$I_{in}$	Maximum current per input	10 A
$V_{oP,nom}$ or $V_{oN,nom}$	Nominal output voltage per phase	$\pm 350V$
$V_{o,nom}$	Nominal bipolar output voltage	700V
$V_{oP}$ or $V_{oN}$	Output voltage range per phase	$\pm 320V - \pm 400V$
$V_o$	Bipolar output voltage range	640V-800V
$I_{oP}$ or $I_{oN}$	Maximum output current per phase	7.35A
$D$	Duty Cycle	0-62.5 %
$f_s$	Switching Frequency	75 kHz

The input voltage limit was decided upon the following two parameters: it should be high enough to activate the controller of the converter and lower than the minimum allowable output voltage of 320V. For the input current, the limiting factor is the rated current of the two interleaved coupled inductors which is 5A, hence 10A in total.

#### 4.3.1 Application in a real project

The MPP voltage ( $V_{mpp}$ ) and current ( $I_{mpp}$ ) of the modern 72 cells PV panels ranges from 38-45V and 9-10.5A, respectively. As a guide, the  $P - Series$  products of the PV panel manufacturing company *SunPower*, were used. They present  $V_{mpp} = 39.5V$  and  $I_{mpp} = 9.3A$ , while  $P_{mpp} = 365W$ , in standard test conditions of  $1000W/m^2$  at  $25^\circ C$ . Also, the open-circuit voltage is  $V_{oc} = 48.08V$  and the short-circuit current is  $I_{sc} = 9.79A$ . Based on these values, the maximum and minimum values of  $V_{mpp}$  and  $P_{mpp}$  can be determined for different temperature conditions. The system is designed for a temperature range of  $-40^\circ C$  to  $85^\circ C$ . According to the datasheet of the panel, the voltage temperature coefficient is  $-0.28\%/^\circ C$ , while the current coefficient is  $0.046\%/^\circ C$ . Finally the power temperature coefficient that was used is  $-0.377\%/^\circ C$ . The following table summarizes the range of operation of a modern PV panel of 72 cells:

Table 4.2: PV panel specifications and guidelines for the design of the MPPT converter at test conditions of  $1000W/m^2$ .

Specs	Temp		
	$-40^\circ C$	$25^\circ C$	$85^\circ C$
$P_{mpp}$ (W)	471	365	306
$V_{mpp}$ (V)	50.85	39.5	33.05
$I_{mpp}$ (I)		9.3	
$V_{oc}$ (V)	60	48.08	42.5
$I_{sc}$ (V)		9.7	

The maximum and minimum values that are shown on the above table are useful for the rating evaluation of the components that will be used. The converter must be able to handle higher voltage

than the maximum  $V_{oc}$  of the worst case scenario (60V per panel at  $-40^{\circ}C$ ). Also, it must be able to supply 300V at a very warm environment of  $85^{\circ}C$ . A string of 5 panels of 72 cells or 6 panels of 60 cells in each input of the converter satisfies the voltage demands of the converter. Every string provides 9.3A at STC, because all the panels are connected in series. According to the temperature and the  $V_{mpp}$ , the maximum provided power of the converter ranges from 1.11-3.72 kW. Hence the maximum output current ranges from 2.8-9.3A.

## 4.4 Schematic overview

This section will present the basic parts of the converter from an electrical engineering point of view, focusing on the components that are used. The Figure 4.6 illustrates the general schematic overview of the MPPT converter. The main parts of the converter are highlighted, with different colors.

The converter consists of two asynchronous interleaved phases with SiC mosfets and diodes. The input power is directed to the two-interleaved phases, which also include the coupled inductors. The micro-Controller Unit ( $\mu CU$ ), regulates the duty cycle, and the switching frequency of the converter. Several measurements of voltage and current are taken from critical points of the converter, which are stored to the  $\mu CU$ . The  $\mu CU$  is then responsible to process these data and act according to the control strategy, implementing the MPPT algorithm. A Wi-Fi/Bluetooth is also integrated in the design, which allows to apply remote control to the converter and monitor the safety alerts of the device.

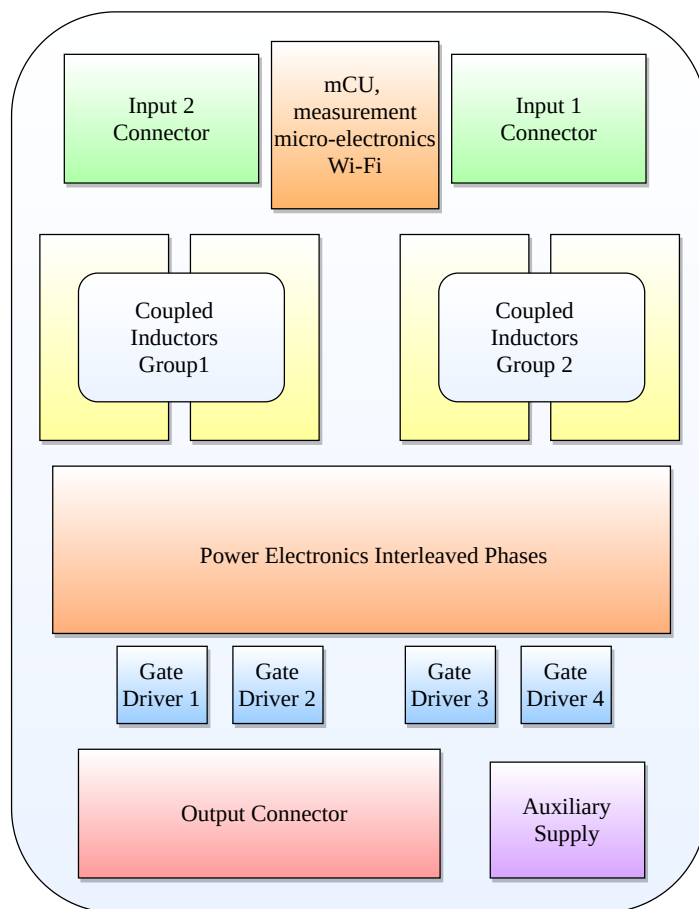


Figure 4.6: The schematic overview of the MPPT Converter.

#### 4.4.1 Design of the input connection

The transfer of power from the PV strings to the inputs of the converter must happen with a stable and safe connection point. The connectors must be able to handle high currents, while they also provide strong mechanical stability. Specifically, the 7462810 from Würth was used. For the filtering of any common mode noise that can travel from the positive and the negative lines of the inputs to the earth, the choke 744831016164 was placed. Finally, for the filtering of the harmonics and the reduction of the input voltage and current ripple, a capacitor is needed. This capacitor stabilizes the input voltage of the PV string, providing the necessary current ripple on the inductors. The product MKP1848C65090JY5 was installed in each one of the two inputs of the converter. It has a capacitance of  $50\mu\text{F}$ , while it can handle up to 900V.

#### 4.4.2 Design of power electronics interleaved phases

The two interleaved phases of the converter consist of two mosfets and two diodes each. Between each diode and a mosfet, an inductor is connected. The semiconductor elements must be able to handle the peak values of the inductor current. The voltage rating of the mosfets and the diodes must be at least 20% more than the output voltage of any phase of the converter. The SiC mosfet C3M0060065J from Cree was chosen for this position. This product can block up to 650V drain-source voltage and tolerate more than 20A at  $120^\circ\text{C}$ . The low  $R_{ds,on}$  and the excellent switching performance minimize the losses. SiC technology was also used for the diodes of the converter, C3D10060G. The use of SiC diodes eliminates the reverse recovery losses, even though the diode presents 1.5V of forward voltage drop. These diodes are also responsible to block the inverse flow of current during the night, when the PV panels are not able to produce high voltage anymore. The Figure 4.7 illustrates one of the two identical interleaved phases.

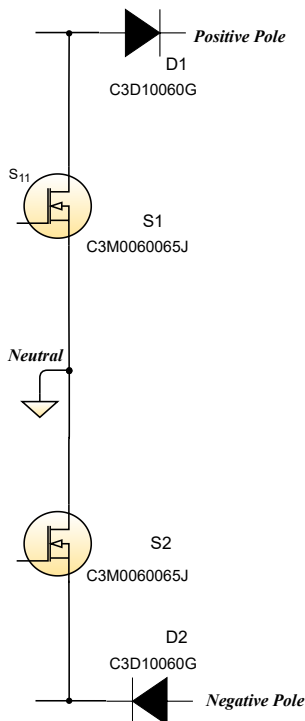


Figure 4.7: The overview of one of the two identical interleaved phases of the MPPT Converter.

### 4.4.3 Design of the coupled inductors

One of the most challenging steps of the design process was the making of the coupled inductors. Due to lack of 'off-the-shelf' coupled inductors that can handle such a high current rating, in compact size that can be soldered on the PCB, it was decided that the magnetics of the converter will be designed and manufactured in the lab. Thus, the blueprint of a planar inductor, consisting of several PCB's, stacked and soldered was tested. Then, four of these stacks were coupled in groups of two with magnetic cores.

As it was discussed before, the inductors that are coupled are the ones that belong to the same position of the interleaved phases. It was decided that the magnetics will be coupled with **inverse coupling**. With this type of coupling, the magnetic fluxes of the two windings are added on the center leg of the core. In the interleaved mode where the applied voltages on the inductors are  $180^\circ$  phase-shifted, the sum of the two fluxes on the core creates smaller flux ripple, hence less core losses. But the high dc offset affects the saturation limit, increasing the specifications of the core. Finally, for a specific range of duty cycle the effective inductance is higher than the self-inductance.

For the proper sizing of the inductors, it is important to calculate the peak current and the maximum current ripple. The peak current will determine the saturation limit of the device. On the other hand, the current ripple will be used to calculate the core losses. The maximum allowable input current of the converter is approximately 10A. Given that the converter has two interleaved phases, each inductor receives half of this average current (5A). After several trials, for different switching frequencies that range from 75 to 100kHz and different core sizes, it was found that the current ripple can be up to two times the average current, with a safety margin of 20%, so 12A. This is the trade-off for designing compact inductors, while keeping the switching frequency as low as possible. Otherwise,  $f_s$  must be increased, with a negative impact both for the switching and the core losses.

Because of the high switching frequency (75-100kHz), the core material that was used is the ferrite. In particular, the cores are made from **3F36**. This type of products is suitable for applications with switching frequency up to 1MHz, presenting low core losses. Also, they have initial permeability of 1600 and saturation magnetic flux density  $B_{sat} = 420T$  at  $100^\circ C$ . Different sizes of 3F36 cores were used for the initial calculations. The core must be able to handle the magnetic flux density of the two inductors, while at the same time it provides enough space between the legs for the current flow on the planar windings. Finally, the legs must have enough length to fit the appropriate number of PCB's, in order to create the desired number of turns and inductance. After several trials, the 'E' type core **E58/11/38** and the 'I' type core **PLT58/38/4** from FerroxCube were combined for the making of each one of the two cores. The effective area of the center leg of this core is  $310mm^2$ . Furthermore, the effective length of the magnetic flux is  $100mm$ . Finally, the volume of the core is  $20800mm^3$ . The above mentioned parameters will be used to calculate the inductance, the number of turns and other important parameters. The next table summarizes the values of the most important parameters:

Table 4.3: Values of the most important parameters of the core.

Specifications	Description	Value
$L_s$	Self-inductance of each inductor	$200 \mu H$
$\mu_i$	Initial permeability	1600
$A_e$	Effective area of the core center leg	$310 mm^2$
$l_e$	Effective length of the magnetic flux	100 mm
$l_g$	Air gap between the 'E' & the 'I' core	1.4 mm
$\hat{I}_L$	Peak inductor current	12 A
$\Delta I_L$	Half of the maximum current ripple of the inductor	6 A

Based on the equations from [40] and [41] for the design of coupled inductors:

$$N = \sqrt{L_s \frac{l_g + \frac{l_e}{\mu_i}}{0.4\pi A_e 10^{-9}}} = 26 \quad (4.33)$$

$$\Delta B_{max} = \frac{\Delta I_L L_s 10^{-6}}{A_e N} = 0.12 \quad [\text{T}] \quad (4.34)$$

$$\hat{B} = \frac{L_s \hat{I}_L 10^{-6}}{A_e N} = 0.25 \quad [\text{T}] \quad (4.35)$$

The worst case scenario for the magnetic flux in the center leg of the core happens when the duty cycle is either 0 or 1. In that case, the peak of the summed magnetic flux in the center leg is:

$$\sum \hat{B} = \frac{3\hat{B}}{2} = 0.375 < 0.420 \quad [\text{T}] \quad (4.36)$$

### Simulations of the coupled inductors in FEMM

Besides the theoretical calculations of the inductance, the magnetic flux density and other parameters, a series of simulations were also made. The model of each simulated coupled inductor was simplified to that of a two-parts surface. In one of the parts the current enters the surface, while in the other part it exits, 26 times. The magnetic flux density plot is shown in Figure 4.8. As it can be seen in the figure, the 'I type' core is on the top of the structure and below that is the 'E type' core. Then, from left to the right of the structure, the boxes show: the part of the PCB's of the first inductor to which the current exits, the part of the first that the current enters, the part of the second that the current exits and the part of the second that the current enters.

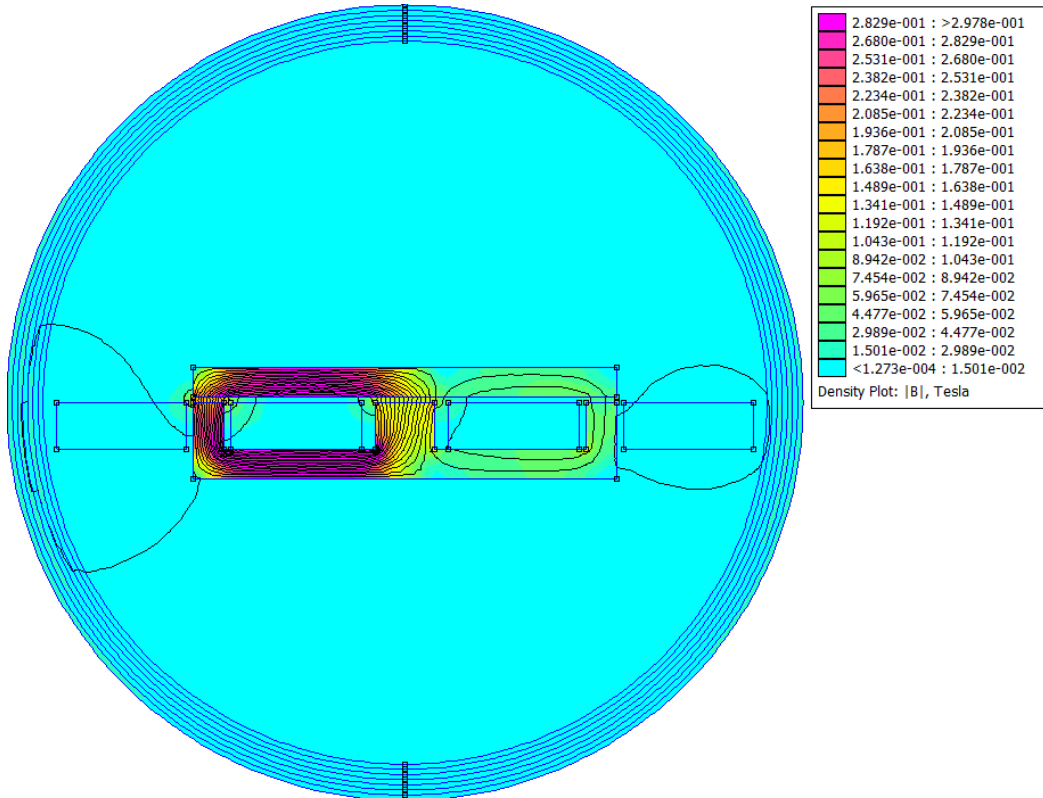


Figure 4.8: Density plot of the magnetic flux of the core, when 7A flow through the left side inductor and 3.5A through the right side inductor.

According to the simulation, the expected inductance of such a design is  $105.8\mu H$ . Furthermore, using the manual of FEMM, it is explained how to calculate the mutual inductance. To do so, the equation (2.10) of the manual [42] is applied. The mutual inductance is expected close to  $85\mu H$ . Hence, from the Equation (4.13), the coupling coefficient will be 0.78.

### Planar inductors in PCB

Each one of the inductors consists of six PCB's. In total, 3 different types of PCB's were made for the completion of a repeatable structure. Every PCB has four layers and every layer is one turn. Thus, every stack of six PCB's makes an inductor of 24 turns, instead of 26 as it was initially aimed. This is done because only six PCB's could fit on the outer legs of the chosen core. The Figure 4.9 shows the structure of two planar coupled inductors. Two of these structures were manufactured and soldered on the main converter PCB.

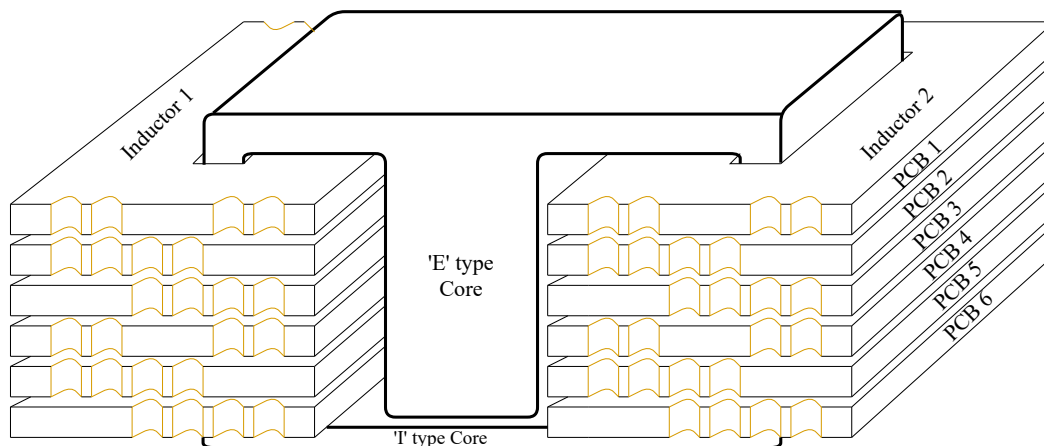


Figure 4.9: Two planar coupled inductors, consisting of 1 stack of 6 PCB's per inductors.

The width of the layers should be enough to handle the maximum average current that can flow on the inductor. For a value of 7A, it was calculated that a copper track with width of at least 15mm was enough for the internal layers of the PCB, which have less copper thickness ( $17\mu m$ ), producing a temperature increase of  $25^\circ C$ , above the average temperature. With these dimensions, the expected resistance of each PCB is  $30m\Omega$  and the total  $180m\Omega$ , producing 8.5W of copper losses.

#### 4.4.4 Design of the gate drivers circuit

For the gate driving of the mosfets in the converter, two different strategies were followed. The mosfets  $S_1$  of the two interleaved phases have their source pins connected, in the same ground with the  $\mu CU$  and the gate driver output supplies. Hence, there is no need for complex isolated gate driving circuitry. The integrated chip **UCC27511** from Texas Instruments was chosen, supplied with 18V from the auxiliary supply of the system.

On the other hand, the mosfets  $S_2$ , need an isolated gate driver, since their source pins are not connected to the ground. For this task, the **UCC5390SC**, also from Texas Instruments, with peak isolation of 5000V, was utilized. The primary side of the chip is supplied with 5V, while the other side is provided with 19V of a devoted isolated power supply. To do so, a small push-pull converter was integrated next to each one of the gate drivers, providing the necessary voltage. The push-pull converter was implemented with the chip **SN6505BDBVR** from Texas Instruments and a small center-tapped transformer, similar to the Voltage Balancing Converter.

Again, a 4.3V clamping voltage zener diode, is used in parallel with a capacitor, placed right after the output of the gate driver. When this circuit is in steady-state, it brings the source of the mosfet to  $-4.3\text{V}$ , protecting the device from the high frequency ringing on the  $C_{gd}$  of the mosfet, which can provoke parasitic switching-on. All of the gate driving chips, have independent outputs for the switching-on and the switching-off of the mosfets. This permits the separate calibration of the on and off delay time. Finally, a resistor is connected in each one of the outputs of the gate drivers, in order to reduce the sourced and sinked currents on the drivers. The overview of the gate drivers is visible in Figure 4.10.

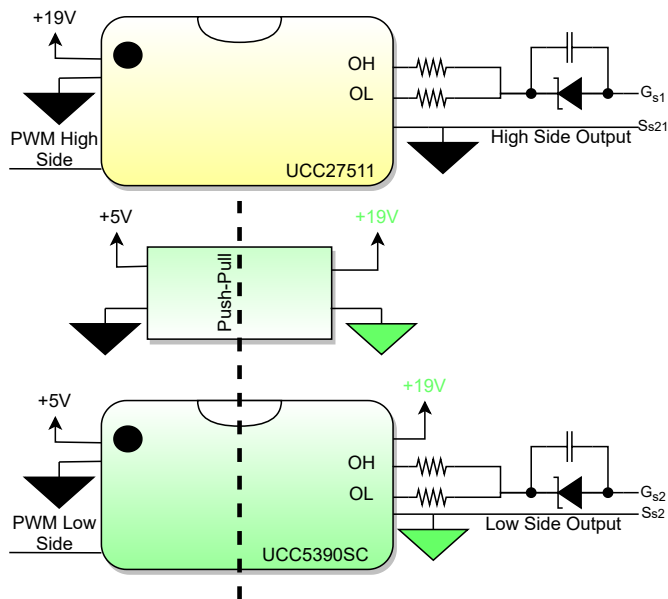


Figure 4.10: Overview of the gate drivers of the MPPT Converter.

#### 4.4.5 Design of the micro-electronics

The  $\mu\text{CU}$  of the MPPT converter is responsible for the implementation of the control algorithms, the measurement of critical values, the switching of the mosfets and the safety overview of the whole topology. For this task, the **STM32G474RET6** was chosen. The particular,  $\mu\text{CU}$  includes 512 kBytes of flash memory, 5 different ADC modules, 17 timers, internal operational amplifiers and up to 48MHz clock. The modern features of the particular micro-controller allow to apply very fast and effective control schemes, while at the same it is ensured that the converter operates with safety. Simultaneously, the  $\mu\text{CU}$  is in charge of the MPPT algorithm. To do so, the  $\mu\text{CU}$  must cooperate with several other micro-electronic devices that measure the voltage and the current in crucial points of the topology. The timers 1 and 2 are used for the PWM generation. Finally, with a UART communication line the  $\mu\text{CU}$  interacts with the Wi-Fi/Bluetooth module **ESP32**. The module sends and receive data with wireless communication, facilitating the remote control of the device.

In the particular converter the points that are measured are: the input voltage, the output voltage and the input current. Different techniques are used for the measurement of each one of them. For the voltages, simple voltage dividers are used. A string of resistors senses the differential voltage between the positive line and the ground. The same strategy is followed for the measuring of the negative line. The only difference is that the voltage divider is not connected to the ground but to  $+3.3\text{V}$  of the auxiliary supply. The measured value is converted through the  $\mu\text{CU}$  to the actual input voltage of the negative line with the following equation:  $V_{inN} = 3.3 - (3.3 - V_{ADC}) \frac{R_1 + R_2}{R_1}$ . Finally, the measurement of the input currents is executed with the **MCA1101-20-3**. This chip includes an anisotropic magneto-resistive sensor which converts an input current of up to  $\pm 20\text{A}$  to a voltage signal

of 0-3V. The measured input currents and voltages are used from the  $\mu CU$  in order to implement the MPPT control. A small RC filter is placed before the signals enter to the  $\mu CU$ . The overview of the above information is shown in Figure 4.11.

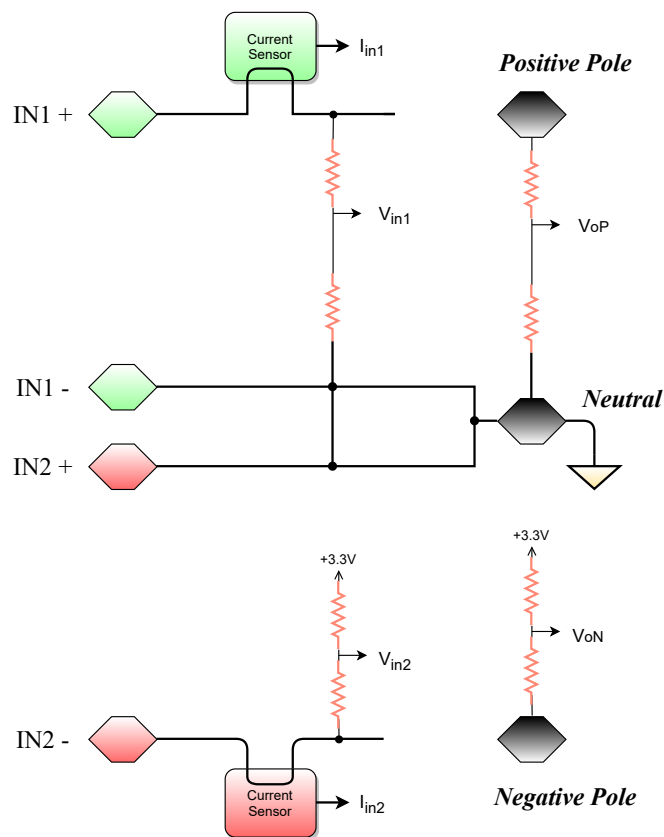


Figure 4.11: The measuring circuitry and the nodes that were measured on the MPPT converter.

#### 4.4.6 Design of the output connection

The power of the converter is transferred to the output with the use of the same connectors as in the input. In addition, two capacitors [C4AQLBW5900A3OK](#) are connected to each bipolar output, filtering the ripple of the output voltage. The capacitors are rated for 500V with capacitance of  $90\mu F$ .

#### 4.4.7 Auxiliary supply

The different voltage levels that are needed to supply every electronic device of the converter are provided with the integration of a small flyback converter. The design of this converter is similar to that of the flyback that was used on the VBC ([Section 3.4.4](#)). This is the second version of this topology which aimed to solve the problems that occurred during the testing of the first prototype. Instead of an 'off-the-shelf' transformer, a planar transformer was designed and integrated in a 6-layers PCB. The PCB of the flyback, is mounted and connected to the output of the main converter PCB.

The integrated chip [UCC28711](#) from Texas Instruments was used for the control of the duty cycle and the switching frequency of the flyback, sending PWM pulses to the SiC mosfet [C2M1000170J](#). The particular mosfet blocks up to 1700V. The transformer consists of 4 different windings. The primary winding is printed in the second and the fourth layer of the PCB, the auxiliary on the first and the sixth and the two output windings on the third and the fifth. The turns ration between the primary

winding and the auxiliary is 13:1, while the turns ratio between the primary and secondary is 11:1. The core of the transformer contains two 'E' type cores E32/6/20 and two 'I' type cores PL32/20/3.2 from FerroxCube, next to each other for higher cross-sectional area. Another difference between the first and the second version is that the input and output capacitance was greatly increased, stabilizing the control of the IC. The testing of the second version at 800V showed excellent results. The converter was able to provide two isolated outputs of 19V. The leakage inductance of the primary winding was negligible, while the achieved inductance of both primary and secondary side was very close to the estimated value. Another advantage of the integrated transformer is that it reduces the size of the converter, making it more compact.

Similar to Section 3.4.4, the first flyback output of 19V is converted to 5V with an integrated buck converter and then to 3.3V with a LDO, supplying power to all the micro-electronic devices. The other output of the flyback is converted to 18V with an adjustable LDO, supplying power to the gate drivers of the  $S_2$  mosfet. The Figure 4.12 shows an overview of the auxiliary supply system.

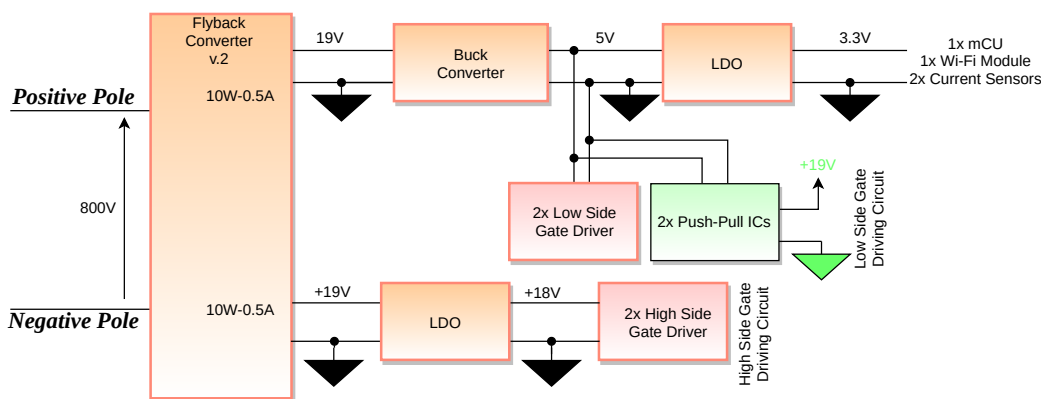


Figure 4.12: The overview of the auxiliary supply of the MPPT converter.

## 4.5 Control strategy

The  $\mu CU$  is responsible for the implementation of the control strategy. Firstly, it executes the MPPT algorithm. Secondly, it must ensure that the converter operates with safety, according to the standards that are set. Two independent controls are applied, for the two inputs of the converter. Hence, it is possible to have better energy yield, with custom-made MPPT for each PV string individually.

The MPPT algorithm that will be used is the 'Perturb and Observe' (P&O). It is widely used as it is considered one of the simplest MPPT techniques. However, it can lead to oscillations around the maximum power point, especially when sudden environmental changes take place [43]. The P&O relies on the observation of the input power through the measurement of the input voltage and current. Specifically, it provokes changes to the input voltage until it reaches a point where  $\frac{dP_{in}}{dV_{in}} = 0$ .

When the voltage of the grid reaches a specific limit, the converter is not able anymore to provide the maximum amount of power. At that region of operation a droop control strategy is applied, reducing the output current. The Figure 4.13 shows the overview of the control.

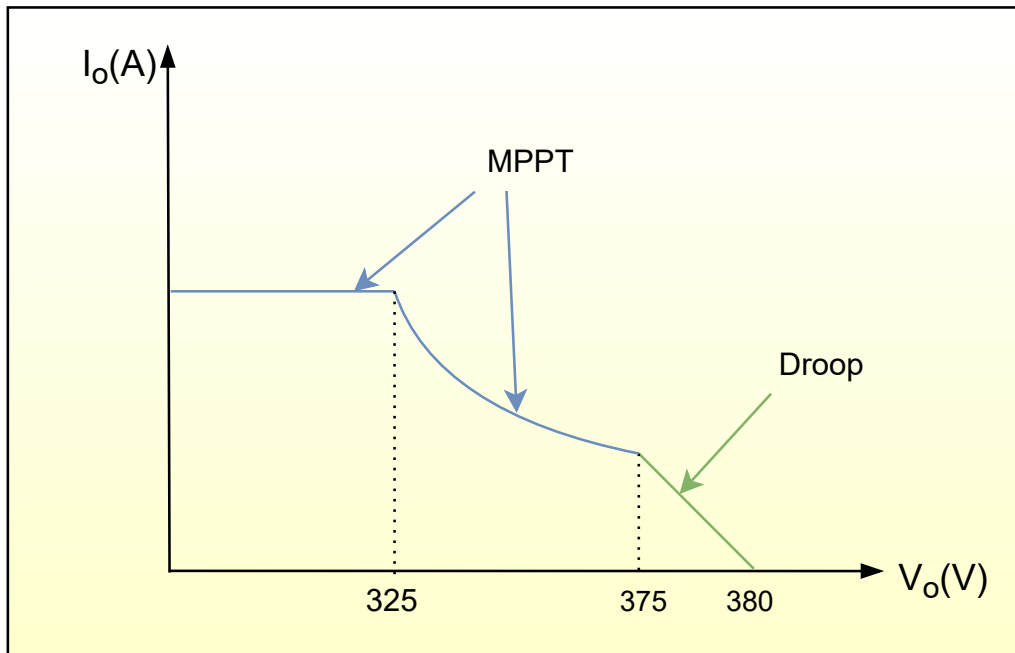


Figure 4.13: The graph of the applied control strategy.

## CHAPTER 5

# TESTING & ANALYSIS OF THE RESULTS

*After the manufacturing of the converters, several tests were carried out. The outcome of the testing process verified the proper functioning of the designed topologies and their useful capabilities for the modern DC Microgrids.*

### 5.1 Breakdown of the test setup

The experiments that took place in the DC lab of *DC-Opportunities* aimed to verify mainly the two following facts:

- The chosen topologies are able to implement the principal tasks for which they were chosen, in a Microgrid.
- The components that were used for the manufacturing of the converters were able to meet with the high voltage standards of the application, with safety and reliability.

Initially, the two basic converters of the project, the Voltage Balancing Converter and the MPPT converter were tested separately.

#### 5.1.1 Basic devices of the test setup

The feeding of power to the converters was done with the use of two 400V DC power supplies. Each device can provide regulated output voltage which ranges from 70V to 400V. The power supplies were connected either in series to the Voltage Balancing converter or independently to the two inputs of the MPPT converter.

During the testing phase and before the the flyback converter was fully tested, two low voltage power supplies were used. These 19V supplies powered the low voltage auxiliary circuits of each power converter.

As a load, two strings of negative temperature coefficient (NTC) resistors of 2kW each were used, connected to the output side of the converters. Each string consists of 4 smaller resistors providing a big span of values, which ranges from 100 $\Omega$  to 2000 $\Omega$ .

Finally, a PC oscilloscope with four channels was used to capture and save the test results.

### 5.1.2 Protection control and output stabilization

In order to conduct the experiments with safety, a control software was developed and applied. The control that was implemented in the Voltage Balancing Converter is explicitly described in [Section 3.5.1](#). On the other hand, the PI algorithm that is applied to the MPPT converter aims to keep the output voltage in a predefined value, chosen by the user. The control scheme is based on a PI algorithm, that is responsible to stabilize the output voltage on the desired level, irrespective of the supplied input voltage or the fluctuations of the load.

Simultaneously, several protection features are integrated on the core of the control. Specifically, if an over-voltage above 400V is detected in the output of the MPPT converter or an over-current which crosses the threshold of the 10.5A in the inductors of the Voltage Balancing Converter, then the corresponding topology switches off.

## 5.2 Test results of the Voltage Balancing Converter

The testing of the Voltage Balancing Converter is implemented in two different ways. Initially, the main voltage balancing mode is tested. Afterwards, the same test setup is used to test the combined inverse mode ([Section 3.2.2](#)). The colored dots in the [Figure 5.1](#) show the points to which the PC oscilloscope channels were connected on the PCB of the converter, while the [Figure 5.2](#) shows the test setup.

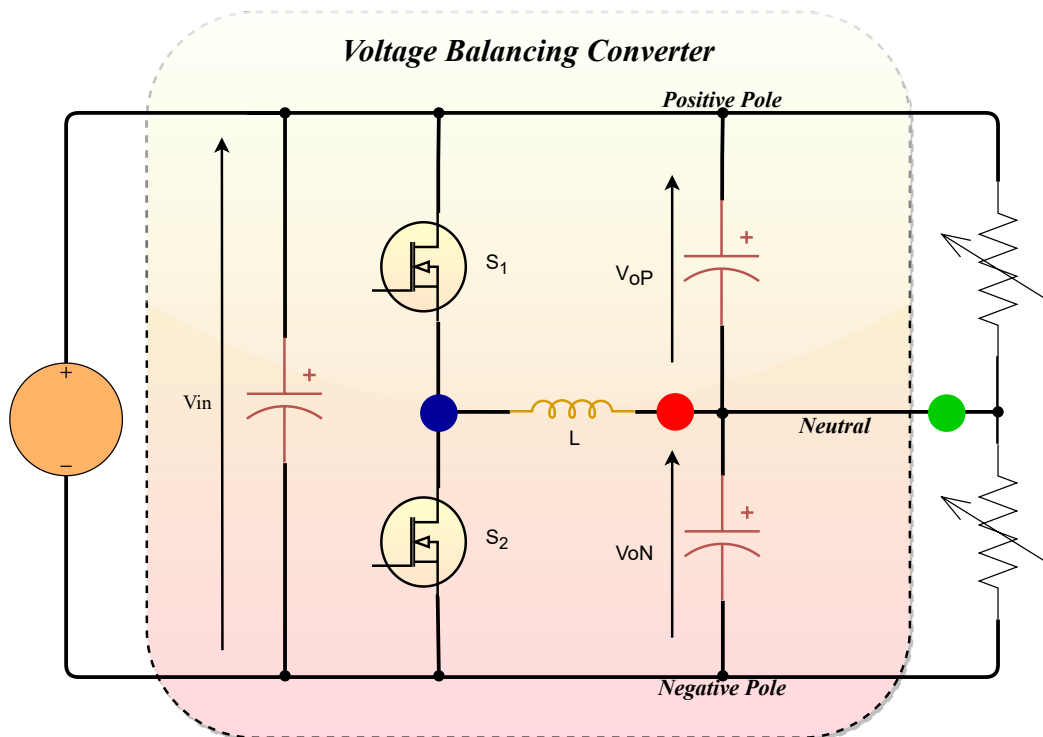


Figure 5.1: The overview of the points that were connected to the oscilloscope.

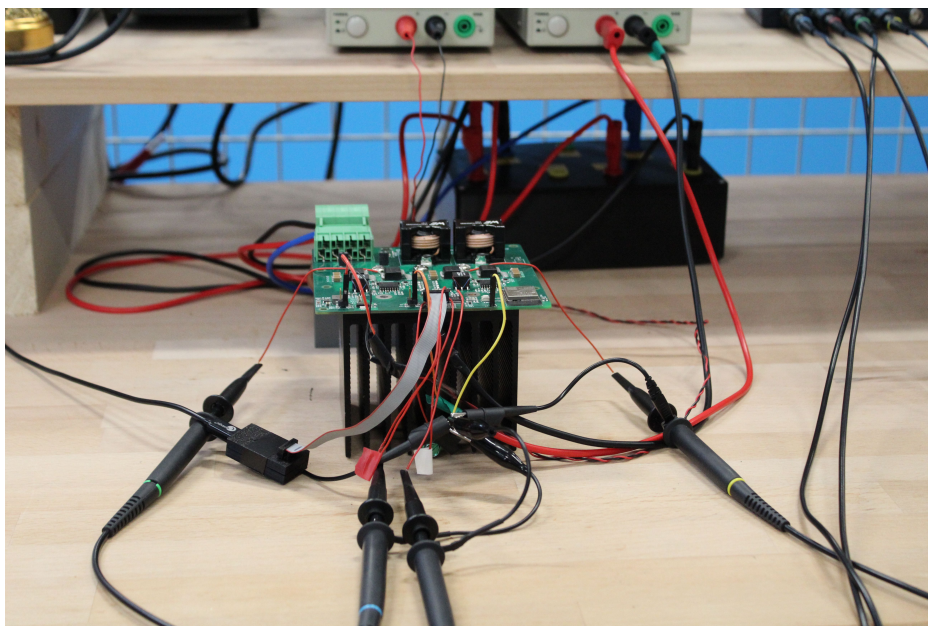


Figure 5.2: The test setup of the Voltage Balancing Converter.

The first test focused on the Voltage Balancing mode (Figure 5.3). A power supply of 335V was connected to the input of the converter, between the positive and negative line. On the load side, two NTC resistors were connected with values of  $400\Omega$  to the positive side and  $500\Omega$  to the negative side. The duty cycle was equal to 0.48 and the switching frequency is 330kHz.

The slightly unbalanced load produced a 0.25A positive current to flow (green), which is shared between the two inductors of the converter. A duty cycle of 0.48, produced 175V in the positive line and -160V to the negative (blue). Finally, the red line shows the inductor current which has a positive average value equal to the half of the output current. Because of the electromagnetic noise that is induced to the measured signals during the switching moments, a digital cut-off filter of 2MHz is introduced.

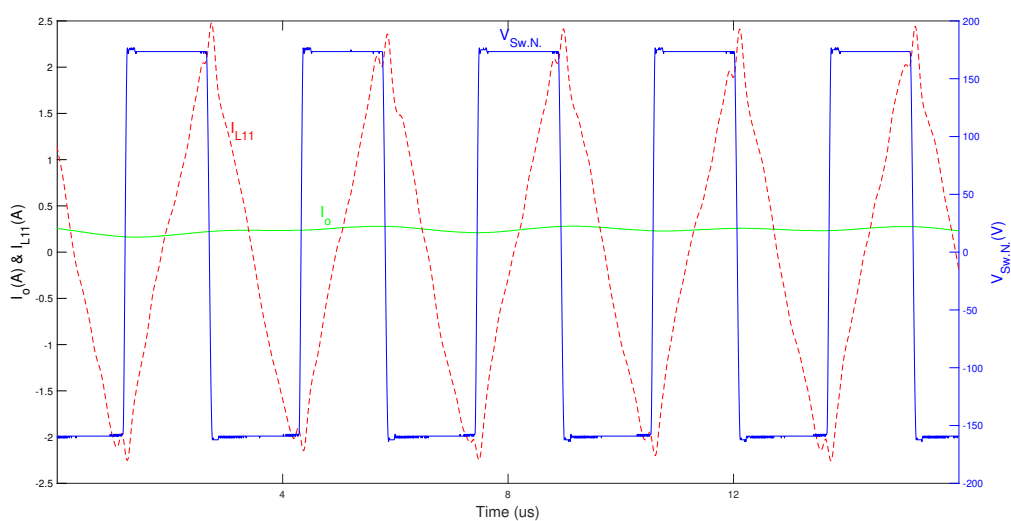


Figure 5.3: The voltage on the switching node of the mosfet  $S_{11}$  and  $S_{12}$  (blue), the output current on the neutral line (green) and the current of the inductor  $L_1$  (red).

The next test, which is illustrated in [Figure 5.4](#), shows the results of the combined inverse mode. The former input of the converter is now connected to the  $400\Omega$  load. The phase between neutral and negative line is connected to a load  $500\Omega$ . Finally the phase between the positive line and the neutral is connected to a power supply of  $110V$ . The duty cycle is  $0.42$ .

The former input that is now connected to the  $400\Omega$  forms a boost converter with output voltage:  $V_{oP} - V_{oN} = 100 - (-90) = 190V$ . Contrary, the negative phase load of  $500\Omega$  forms a buck-boost converter with output voltage of  $-90V$ . The aforementioned details are shown in blue color, on the switching node of the mosfet  $S_{11}$ . This provokes a positive output current of  $1.9A$  (green), which is shared between the two inductors. The red curve shows the current of the inductor  $L_1$ .

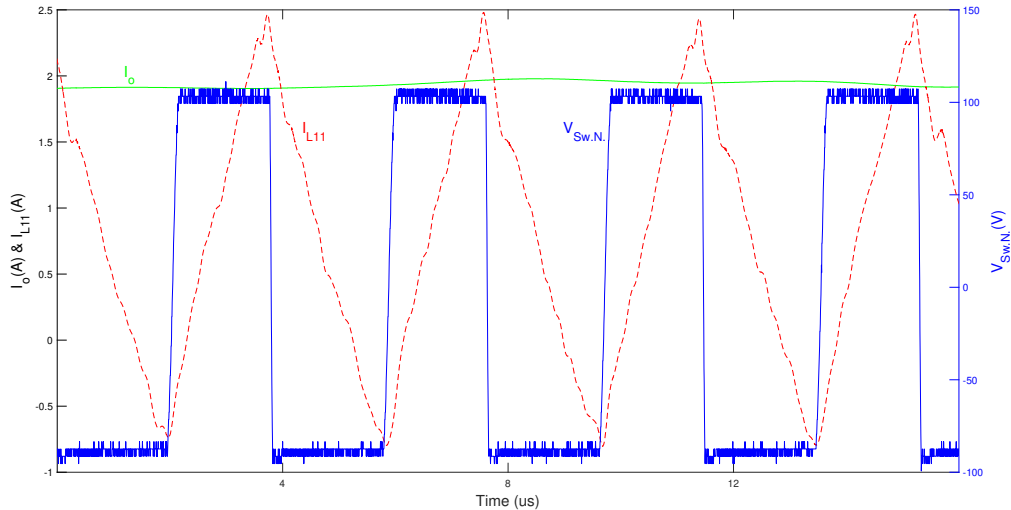


Figure 5.4: The voltage on the switching node of the mosfets  $S_{11}$  and  $S_{12}$  (blue), the output current on the neutral line (green) and the current of the inductor  $L_1$  (red), when the converter is used in the combined inverse mode.

### 5.3 Test results of the MPPT converter

The testing of the MPPT converter aimed to prove that the converter can reach the maximum output voltage limits of  $\pm 350V$ . In order to carry out the tests, the designed PI control brought the output voltage to the desired levels. Several trials were done before the proportional ( $K_p$ ) and integral ( $K_i$ ) gains of the control scheme were properly tuned. Simultaneously, the  $\mu CU$  of the converter switches-off the mosfets, if an over-voltage of  $400V$  or more is detected in the output. The goal of the PI control is to keep the output voltage constant and independent of the changes of the input voltage or the load.

The colored dots in the following graph ([Figure 5.5](#)) show the points to which the PC oscilloscope channels were connected on the PCB of the converter. The [Figure 5.6](#) illustrates the test setup.

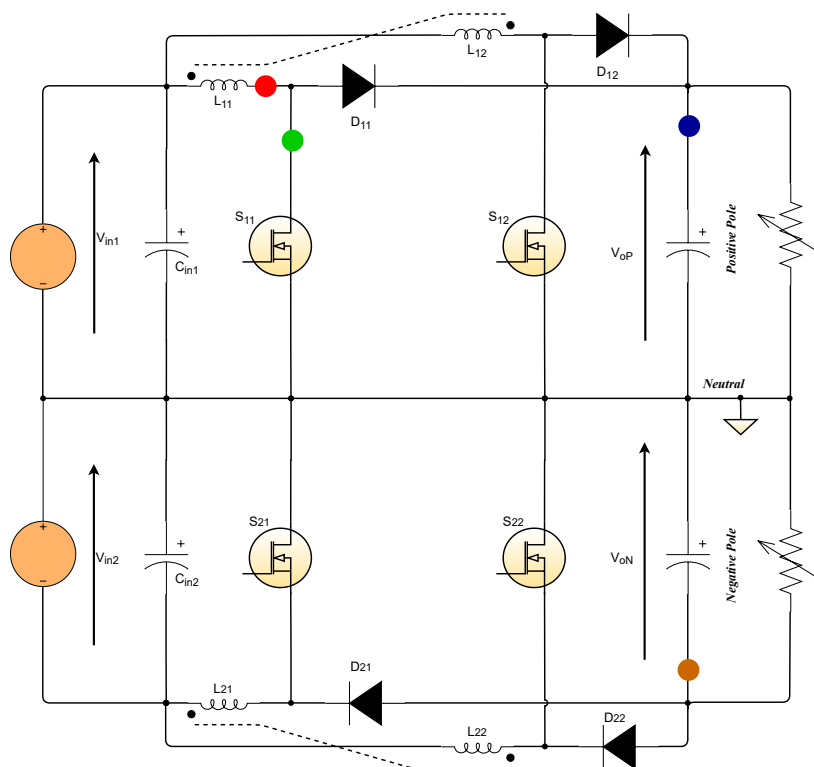


Figure 5.5: The overview of the points that were connected to the oscilloscope.

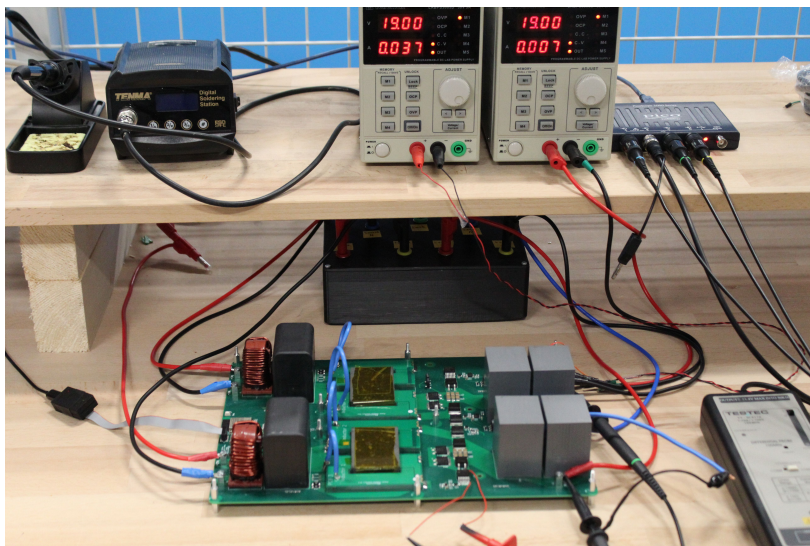


Figure 5.6: The test setup of the MPPT converter.

The [Figure 5.7](#) shows the first test that was done to the MPPT converter. The Input 1 provides 120V, while the Input 2 110V. On the other side, the loads that were connected were initially 800Ω, while their values reduced as they become warmer.

The PI controller of this test is set to provide 150V in the output. At  $t=0.3s$ , the Input 1 is activated. After the overshoot of 30V is damped, the positive output voltage (blue) is stabilized at this value.

### 5.3. TEST RESULTS OF THE MPPT CONVERTER

The same applies for the negative output (brown) of the converter, when the Input 2 is connected at  $t=2.25$ s. Despite the fact, that the load resistor values gradually changed, the PI controller was able to keep the output voltages constant.

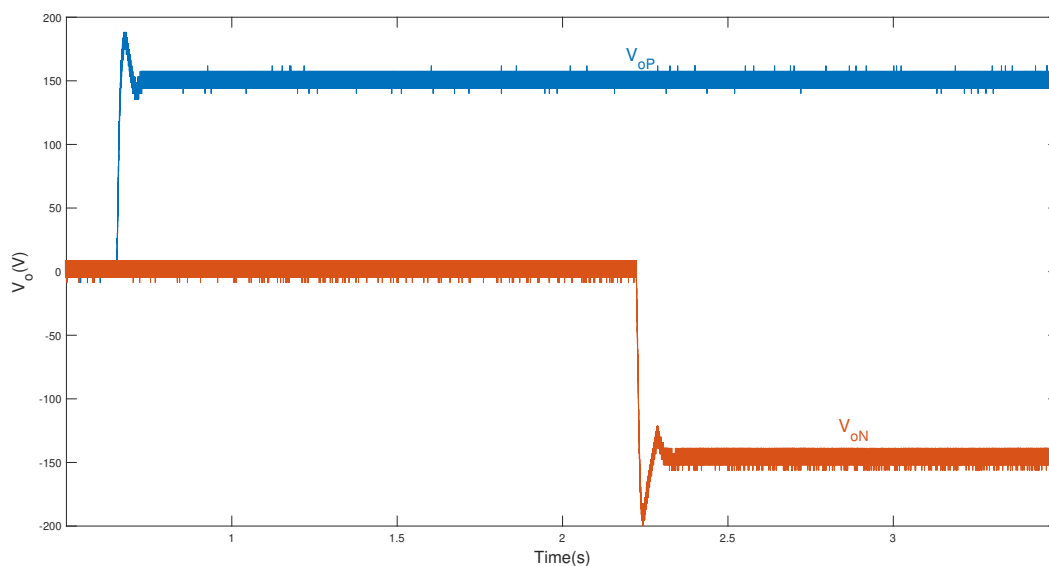


Figure 5.7: The 150V positive (blue) and the negative (brown) line output voltage of the MPPT converter with unbalanced inputs of 120V and 110V.

A similar test is presented in the [Figure 5.8](#). However, now the goal is to provide 350V to the outputs, verifying that the converter is able to meet the output voltage specifications. In particular, both the input voltages are 200V. The Input 1 is activated at  $t=1$ s, while the Input 2 at  $t=2.25$ s. When the 15V overshoot is damped, the positive (blue) and the negative (brown) voltages stabilize at the value of  $\pm 350$ V. This creates a bipolar DC grid of 700V.

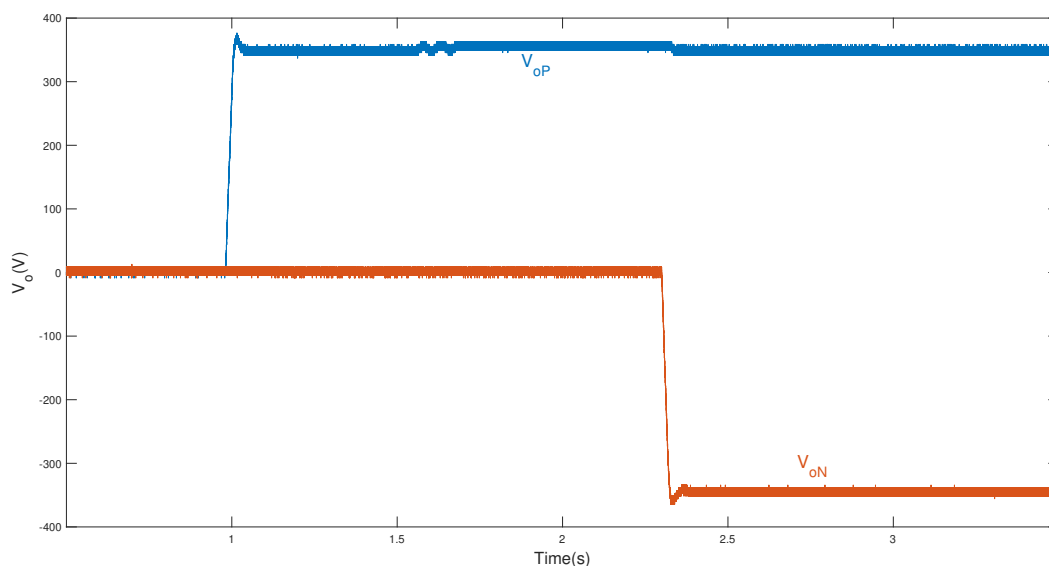


Figure 5.8: The 350V positive (blue) and the negative (brown) line output voltage of the MPPT converter with 200V inputs.

Afterwards, the switching node (green) between the mosfet  $S_{11}$  and the diode  $D_{11}$  is measured along

with the current (red) of the coupled inductor that is connected at this point, when the output voltage is 300V, in [Figure 5.9](#). Given that the load is very small, the converter operates in DCM. Hence, the current of the inductor presents many oscillations. Further details of the coupled inductors will be given in [Section 5.4](#).

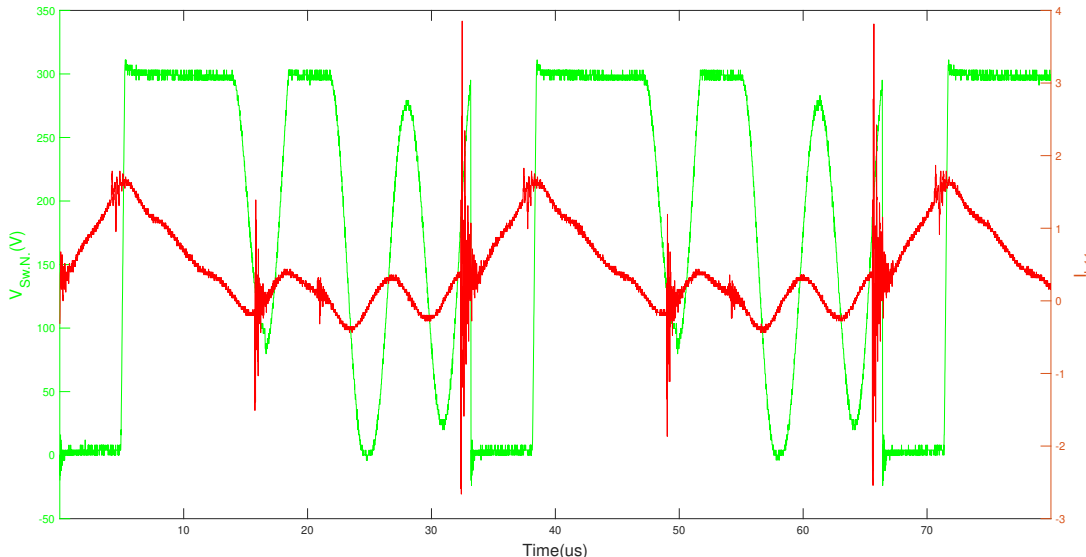


Figure 5.9: The voltage on the switching node of the mosfet  $S_{11}$  (green) and the current of the inductor  $L_{11}$  (red).

## 5.4 Test results of the coupled inductors

One of the most important parts of the testing phase is the calculation of the inductance and the coupling coefficient of the manufactured coupled inductors. These data can be compared with the theoretical calculations, providing useful feedback.

In order to make the calculations simpler and more reliable, a low voltage and higher current experiment was conducted which made the converter operate in CCM. This way, the different regions of operation of the coupled inductor are distinguishable. Only the Input 1 was used providing 30V, while the output voltage was 96V.

The [Figure 5.10](#) provides the waveforms of the current of the inductor  $L_{11}$  (red). The hard switching of the mosfets emits a significant amount of electromagnetic noise in the measured signals. Thus, a 10MHz digital cut-off filter is applied to the inductor current graph (red), in order to make it more clear.

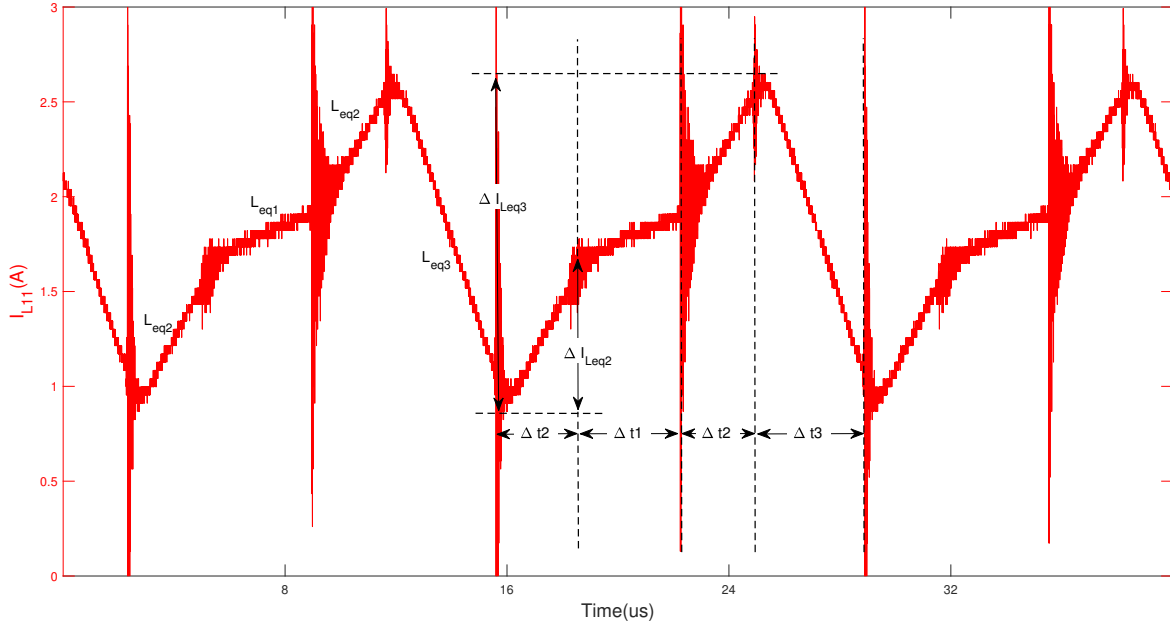


Figure 5.10: The current of the coupled inductor  $L_{11}$  (red), during CCM.

The following calculations provide the inductance and the coupling coefficient of the coupled inductors. Given that the inductors were manufactured in the lab and they are not an "off-the-shelf" product, they present some differences. However, they are negligible, making the assumption that they have equal inductances valid.

From the [Figure 5.10](#) it can be found that:

$$\begin{aligned}\Delta I_{Leq2} &= 0.674A \\ \Delta t_2 &= 2.9\mu s \\ \Delta I_{Leq3} &= -1.32A \\ \Delta t_3 &= 3.805\mu s \\ D &= \frac{\Delta t_2 + \Delta t_1 + \Delta t_2}{\Delta t_1 + \Delta t_2 + \Delta t_3 + \Delta t_2} = 0.7\end{aligned}$$

Adjusting the fundamental equation of inductors to the case of coupled inductors:

$$L_{eq2} = \frac{V_{in1}\Delta t_2}{\Delta I_{Leq2}} = 128.9\mu H \quad (5.1)$$

$$L_{eq3} = \frac{(V_{oP} - V_{in1})\Delta t_3}{\Delta I_{Leq3}} = 193.13\mu H \quad (5.2)$$

Using the [Equation \(4.19\)](#) and [Equation \(4.20\)](#) it was found that the self-inductance and the coupling coefficient of the coupled inductors are:

$$\begin{aligned}L_s &= 185\mu H \\ \kappa &= -0.305\end{aligned}$$

## 5.5 Test results of the flyback converter V.2

The following graph (Figure 5.11) shows one of the two identical output voltages (blue) of the second version of the flyback converters that was designed. In addition, it is presented in green color, the voltage on the auxiliary winding of the transformer. Finally, the voltage on the shunt resistor that senses the primary transformer winding current is shown in red.

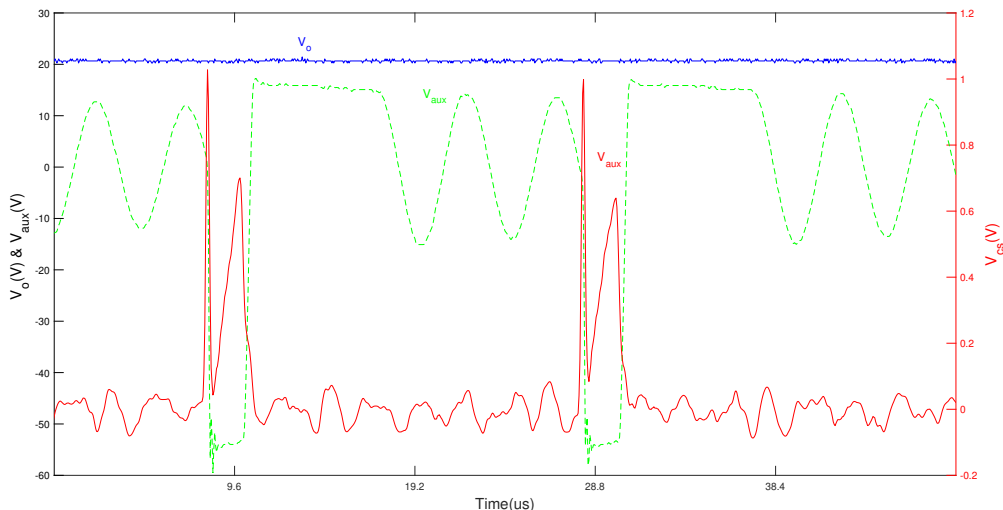


Figure 5.11: The voltage on the output of the flyback converter (blue), the voltage on the anode of the auxiliary diode (green) and the voltage on the current-sense pin of the IC (red).

The flyback converter was tested under full input voltage of 800V. The two outputs of the topology supplied almost 20V (ideally the converter should provide 19V) to two loads of 2W.

## 5.6 Discussion

The testing procedure of all the designed topologies extracted very useful data, both for the potentials and the challenges of DC-DC converters, when they are used in PV powered DC Microgrids. Overall, the experiments showed that the converters are able to meet the voltage criteria of the project and reliably produce a stable bipolar DC grid. Specifically:

### For the Voltage Balancing Converter:

- The open loop control tests, provided constant bipolar DC output. The use of synchronous half-bridges, simplified the control complexity, since the output depends only on the duty cycle.
- The use of interleaved configuration, reduces the current stress of the components and makes the accomplishment of zero voltage switching easier, given that the average inductor current is half of the output current.

### For the MPPT Converter:

- The closed loop PI control tests that were done, proved that it can reliably create a  $\pm 350V$  bipolar DC grid.
- The positive and the negative outputs are completely independent. This makes the design of two independent MPPT algorithms feasible.

### **For the coupled inductors:**

- The testing of the coupled inductors and the calculations that were afterwards done, verified that the final manufactured product is very close to the theoretical estimations of the design phase.
- The inductors reached peak currents of 6.5A without presenting saturation effects. Hence, they meet the criteria of the project, given that the maximum input current is 10A and the inductors are interleaved.

### **For the flyback converter V.2:**

- The second version of this converter solved the problem of auxiliary supply when the converters are not tested anymore in lab setup, but as actual products, in real projects.

*The interesting results that are extracted from the design and the testing of the converters are summarized in this chapter. Useful conclusions are drawn and recommendations are given for future improvements.*

## 6.1 Discussion over the research questions

The goal of this section is to present if and how this thesis project answers to the research questions that were addressed in [Chapter 1](#):

### **How can a PV plant be integrated to a Bipolar DC Microgrid?**

The use of two independent MPPT boost converters connected as it is described in [Chapter 4](#), proved to be a very efficient solution. The manufactured topology is able to host in the same structure two converters that share the same micro-electronic components, auxiliary supplies and  $\mu CU$ . Simultaneously, two independent PV strings can be connected to its inputs, with separate MPPT algorithms that extract the maximum amount of power from each PV string individually. If necessary, the neutral line can be omitted, providing power to the grid only through the positive and the negative line.

### **How can the voltage between the positive and the negative phase remain balanced in a Bipolar DC Microgrid?**

The topology that was chosen to implement this task, as explained in [Chapter 3](#), is a structure which presents low hardware complexity, while at the same time it can efficiently balance the output loads. This converter can be connected between the output of the MPPT converter and the loads, providing an extra degree of freedom and shaping the grid voltage of the two bipolar phases of the Microgrid.

## What are the possible benefits of using silicon-carbide (SiC) mosfets, zero voltage switching technique and coupled inductors for the specific converters?

The use of silicon-carbide mosfets instead of their standard counterparts, allows to the converters to operate at much higher switching frequency. When necessary, the Voltage Balancing converter is able to operate even at 600kHz, lowering the inductor current ripple. This minimizes the core losses and the conduction losses. Simultaneously, they present reduced conduction and switching losses. This feature gives to the MPPT converter the ability to operate at 75kHz with hard-switching, making the control strategy much simpler. Furthermore, increased switching frequency results in smaller inductors. This reduces the cost and the size of the magnetics and the filters approximately by 30%. Besides the SiC mosfets, the MPPT includes SiC diodes. This type of diodes has almost zero reverse-recovery losses, even though the present slightly higher forward voltage drop compared to standard technologies.

Another feature that is added to the Voltage Balancing Converter is the zero voltage switching. As it is explained in [Section 3.5.2](#), the inductor current can be used to eliminate the switching losses on the SiC mosfets. These losses constitute almost 50% of the total losses on the semiconductors. Hence, the efficiency of the converter is greatly improved.

Finally, the coupled inductors have a positive impact on the MPPT converter. Firstly, the size of the core is reduced by 30% compared to a similar design which has non-coupled magnetics. This reduces the cost and the size of the converter. In addition, when the duty cycle ranges from 0.5 to 0.7 the effective inductance is higher than the self-inductance. Thus, the current ripple is lower, reducing the core losses. However, actual test results will be available only when the converter is tested at higher power.

## 6.2 Future recommendations

The general outcome of this thesis project is the designing, the manufacturing and the testing of the aforementioned topologies. Each one of these steps was carried out carefully, in order to achieve the individual milestones of every phase. During this procedure, very useful knowledge and experience was acquired. All of these lessons can be used in the future for the making of even more advanced power electronics converters. The main areas that can or should be improved in the future are analyzed in the following paragraphs.

Overall, the converters were able to meet the high voltage standards of the application. However, it is important that the control algorithms are fully developed in order to make the product reliable. Only then, the topologies will be able to implement MPPT, balance the bipolar voltages while having ZVS and monitor the system for over-voltage or over-current scenarios. When this step is done, the converters will be able to achieve their full functionality and interconnect, forming a modern DC bipolar Microgrid.

The future testing in a higher power setup, will provide useful feedback for the thermal behaviour of the converters. It is crucial to make clear that the components that are used are able to handle the losses. If not, extra measures have to be taken on the existing thermal design, that will keep the semiconductors below the destructive temperature of 170 °C.

Another factor that has a lot of room for improvement is the coupled inductors. Despite the fact that the manufactured products are operating well, it is important to search for ways to make their manufacturing more reliable or find an "off-the-shelf product". Otherwise, there might be significant differences on their properties. Also, the mounting of the PCB stacks of the inductors on the main converter must be done through a mechanically stable connection point and not through the electrical connection of the solder pads.

Finally, minor changes could be done on the measurement signals circuitry that feed the ADC

## 6.2. FUTURE RECOMMENDATIONS

---

converters of the  $\mu CU$ . This will provide more valid measurements that can improve the speed and the effectiveness of the control algorithms.

## BIBLIOGRAPHY

- [1] Makoto Kanagawa and Toshihiko Nakata. “Assessment of access to electricity and the socio-economic impacts in rural areas of developing countries”. In: *Energy policy* 36.6 (2008), pages 2016–2029.
- [2] International Energy Agency. *SDG7: Data and Projections*. URL: <https://www.iea.org/reports/sdg7-data-and-projections/access-to-electricity#abstract>.
- [3] K Keramidas et al. “Global Energy and Climate Outlook 2019: Electrification for the low-carbon transition”. In: ().
- [4] Our World in Data. *SDG7: Data and Projections*. URL: <http://vaclavsmil.com/2016/12/14/energy-transitions-global-and-national-perspectives-second-expanded-and-updated-edition/%20;%20https://www.bp.com/en/global/corporate/energy-economics/statistical-review-of-world-energy.html>.
- [5] Donald J Hammerstrom. “AC versus DC distribution systemsdid we get it right?” In: *2007 IEEE Power Engineering Society General Meeting*. IEEE. 2007, pages 1–5.
- [6] Alexander Stippich et al. “From AC to DC: Benefits in household appliances”. In: *International ETG Congress 2017*. VDE. 2017, pages 1–6.
- [7] Daniel Nilsson and Ambra Sannino. “Efficiency analysis of low-and medium-voltage DC distribution systems”. In: *IEEE Power Engineering Society General Meeting, 2004*. IEEE. 2004, pages 2315–2321.
- [8] Arno HM Smets et al. *Solar Energy: The physics and engineering of photovoltaic conversion, technologies and systems*. UIT Cambridge, 2015.
- [9] Darren M Bagnall and Matt Boreland. “Photovoltaic technologies”. In: *Energy Policy* 36.12 (2008), pages 4390–4396.
- [10] Priscila Gonçalves Vasconcelos Sampaio et al. “Photovoltaic technologies: Mapping from patent analysis”. In: *Renewable and Sustainable Energy Reviews* 93 (2018), pages 215–224.
- [11] International Energy Agency. *Solar PV*. URL: <https://www.iea.org/reports/solar-pv>.
- [12] Weidong Xiao et al. “Review of grid-tied converter topologies used in photovoltaic systems”. In: *IET Renewable Power Generation* 10.10 (2016), pages 1543–1551.
- [13] Frede Blaabjerg, Zhe Chen, and Soeren Baekhoej Kjaer. “Power electronics as efficient interface in dispersed power generation systems”. In: *IEEE transactions on power electronics* 19.5 (2004), pages 1184–1194.
- [14] Juan Manuel Carrasco et al. “Power-electronic systems for the grid integration of renewable energy sources: A survey”. In: *IEEE Transactions on industrial electronics* 53.4 (2006), pages 1002–1016.
- [15] Hopewind. *Inverters Hopewind*. URL: [http://www.hopewindelectric.com/c-d-pv-grid-connected-inverter\\_p12.html](http://www.hopewindelectric.com/c-d-pv-grid-connected-inverter_p12.html).
- [16] ABB. *Inverters*. URL: [https://library.e.abb.com/public/5d75f6eca7624e76a8fa4c4362953460/Solar\\_inverters\\_and\\_inverter\\_solutions\\_for\\_power\\_generation\\_brochure\\_3AXD50000039235\\_RevD\\_EN\\_2019.pdf](https://library.e.abb.com/public/5d75f6eca7624e76a8fa4c4362953460/Solar_inverters_and_inverter_solutions_for_power_generation_brochure_3AXD50000039235_RevD_EN_2019.pdf).

- [17] Enphase. URL: <https://www.stralendgroen.nl/wp-content/uploads/2018/07/IQ7-IQ7plus-DS-NL-NL.pdf>.
- [18] K Arulkumar, K Palanisamy, and D Vijayakumar. “Recent advances and control techniques in grid connected PV system—A review”. In: *International Journal of Renewable Energy Research* 6.3 (2016), pages 1037–1049.
- [19] Sudipta Chakraborty, Bill Kramer, and Benjamin Kroposki. “A review of power electronics interfaces for distributed energy systems towards achieving low-cost modular design”. In: *Renewable and Sustainable Energy Reviews* 13.9 (2009), pages 2323–2335.
- [20] R Reshma Gopi and S Sreejith. “Converter topologies in photovoltaic applications—A review”. In: *Renewable and Sustainable Energy Reviews* 94 (2018), pages 1–14.
- [21] Wuhua Li and Xiangning He. “Review of nonisolated high-step-up DC/DC converters in photovoltaic grid-connected applications”. In: *IEEE Transactions on Industrial Electronics* 58.4 (2010), pages 1239–1250.
- [22] Carlos Marcelo de Oliveira Stein, José Renes Pinheiro, and Hélio Leães Hey. “A ZCT auxiliary commutation circuit for interleaved boost converters operating in critical conduction mode”. In: *IEEE Transactions on Power Electronics* 17.6 (2002), pages 954–962.
- [23] R-J Wai and C-Y Lin. “High-efficiency, high-step-up DC–DC converter for fuel-cell generation system”. In: *IEE Proceedings-Electric Power Applications* 152.5 (2005), pages 1371–1378.
- [24] H Shu-Hung Chung. “Design and analysis of a switched-capacitor-based step-up DC/DC converter with continuous input current”. In: *IEEE Transactions on Circuits and Systems I: Fundamental Theory and Applications* 46.6 (1999), pages 722–730.
- [25] KK Law, KW Eric Cheng, and YP Benny Yeung. “Design and analysis of switched-capacitor-based step-up resonant converters”. In: *IEEE Transactions on Circuits and Systems I: Regular Papers* 52.5 (2005), pages 943–948.
- [26] Cree. *CRD-60DD12N*. URL: <https://www.wolfspeed.com/crd-60dd12n>.
- [27] Laurens Mackay et al. “Optimal power flow for unbalanced bipolar DC distribution grids”. In: *IEEE Access* 6 (2018), pages 5199–5207.
- [28] Jackson John Justo et al. “AC-microgrids versus DC-microgrids with distributed energy resources: A review”. In: *Renewable and sustainable energy reviews* 24 (2013), pages 387–405.
- [29] Estefania Planas et al. “AC and DC technology in microgrids: A review”. In: *Renewable and Sustainable Energy Reviews* 43 (2015), pages 726–749.
- [30] Xiongfei Wang et al. “A review of power electronics based microgrids”. In: *Journal of Power Electronics* 12.1 (2012), pages 181–192.
- [31] Ambra Sannino, Giovanna Postiglione, and Math HJ Bollen. “Feasibility of a DC network for commercial facilities”. In: *Conference Record of the 2002 IEEE Industry Applications Conference. 37th IAS Annual Meeting (Cat. No. 02CH37344)*. Volume 3. IEEE. 2002, pages 1710–1717.
- [32] Hiroaki Kakigano, Yushi Miura, and Toshifumi Ise. “Low-voltage bipolar-type DC microgrid for super high quality distribution”. In: *IEEE transactions on power electronics* 25.12 (2010), pages 3066–3075.
- [33] Mohammad E Khodayar. “Rural electrification and expansion planning of off-grid microgrids”. In: *The Electricity Journal* 30.4 (2017), pages 68–74.
- [34] Longcheng Tan et al. “Effective voltage balance control for bipolar-DC-bus-fed EV charging station with three-level DC–DC fast charger”. In: *IEEE Transactions on Industrial Electronics* 63.7 (2016), pages 4031–4041.
- [35] Jackson Lago, Joabel Moia, and Marcelo L Heldwein. “Evaluation of power converters to implement bipolar DC active distribution networks—DC-DC converters”. In: *2011 IEEE Energy Conversion Congress and Exposition*. IEEE. 2011, pages 985–990.
- [36] Pit-Leong Wong et al. “Performance improvements of interleaving VRMs with coupling inductors”. In: *IEEE Transactions on Power Electronics* 16.4 (2001), pages 499–507.
- [37] Guangyong Zhu, Brent A McDonald, and Kunrong Wang. “Modeling and analysis of coupled inductors in power converters”. In: *IEEE transactions on Power Electronics* 26.5 (2010), pages 1355–1363.

- [38] Jong-Pil Lee et al. “Analysis and design of coupled inductors for two-phase interleaved DC-DC converters”. In: *Journal of power electronics* 13.3 (2013), pages 339–348.
- [39] Taewon Kang and Yongsug Suh. “Selection of Coupling Factor for Minimum Inductor Current Ripple in Multi-winding Coupled Inductor Used in Bidirectional DC-DC Converters”. In: *Journal of Power Electronics* 18.3 (2018), pages 879–891.
- [40] Power Supply Design Seminar. “Practical Magnetic Design: Inductors and Coupled Inductors”. In: (2012).
- [41] Robert W Erickson and Dragan Maksimovic. *Fundamentals of power electronics*. Springer Science & Business Media, 2007.
- [42] David Meeker. “Finite element method magnetics”. In: *FEMM* 4 (2010), page 32.
- [43] Abhishek Kumar Gupta and Ravi Saxena. “Review on widely-used MPPT techniques for PV applications”. In: *2016 International Conference on Innovation and Challenges in Cyber Security (ICICCS-INBUSH)*. IEEE. 2016, pages 270–273.

# APPENDICES

## APPENDIX A

### PICTURES OF THE MANUFACTURED CONVERTERS

*This appendix includes the photographs of all the constructed converters, with detailed explanation of the position of the most important parts.*

#### A.1 Voltage Balancing Converter

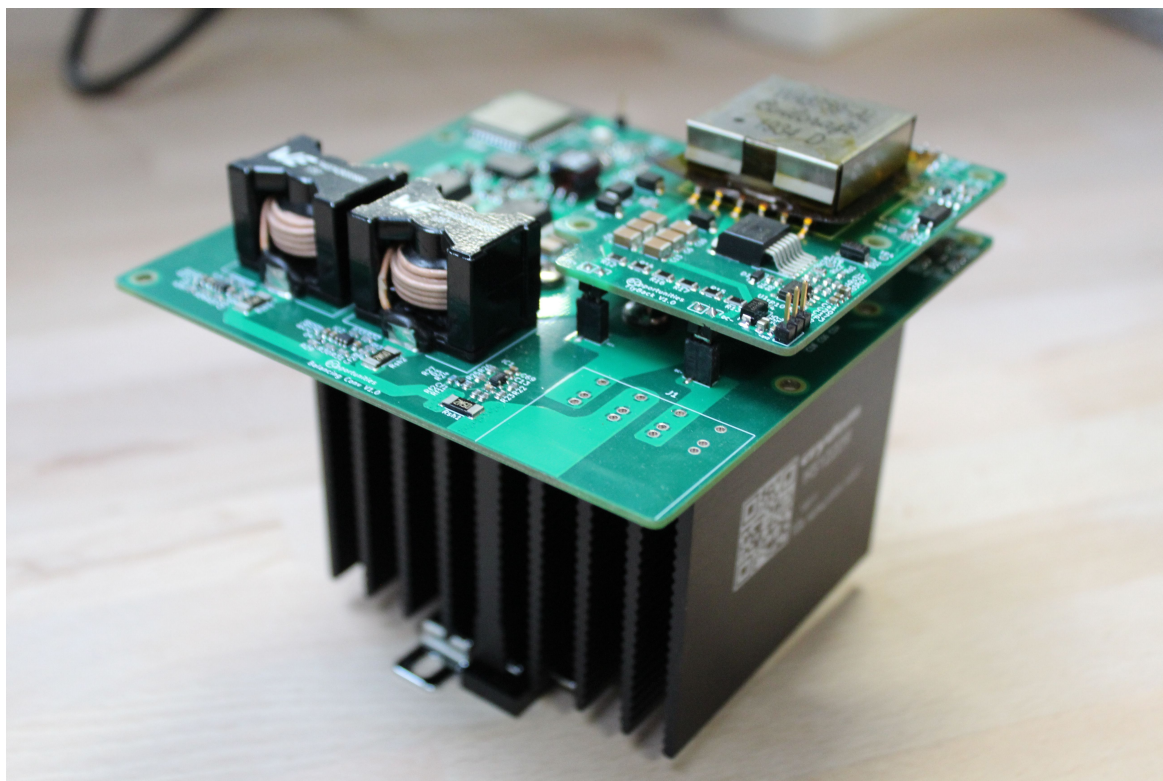


Figure A.1: The illustration of the Voltage Balancing Converter.

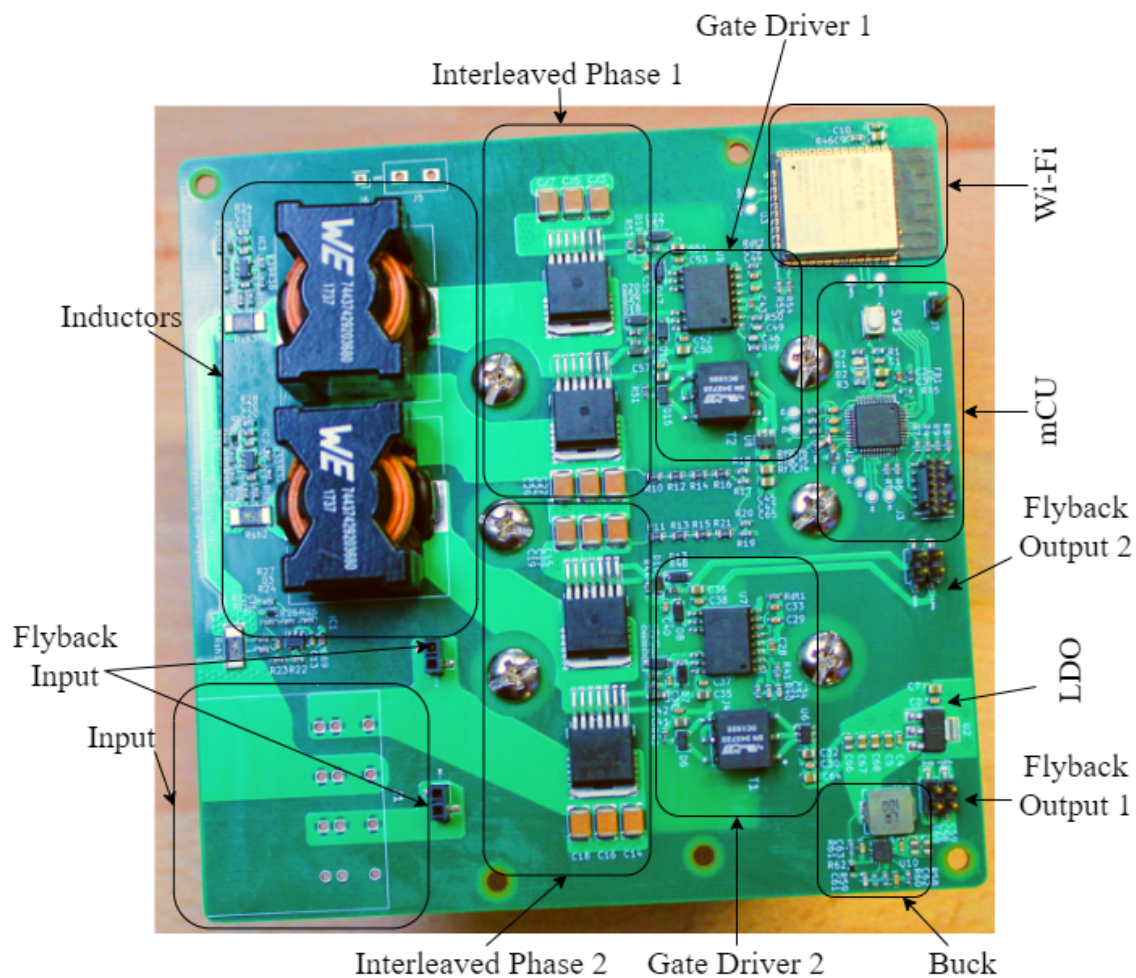


Figure A.2: The overview of the Voltage Balancing Converter.

## A.2 Maximum Power Point Tracking Converter

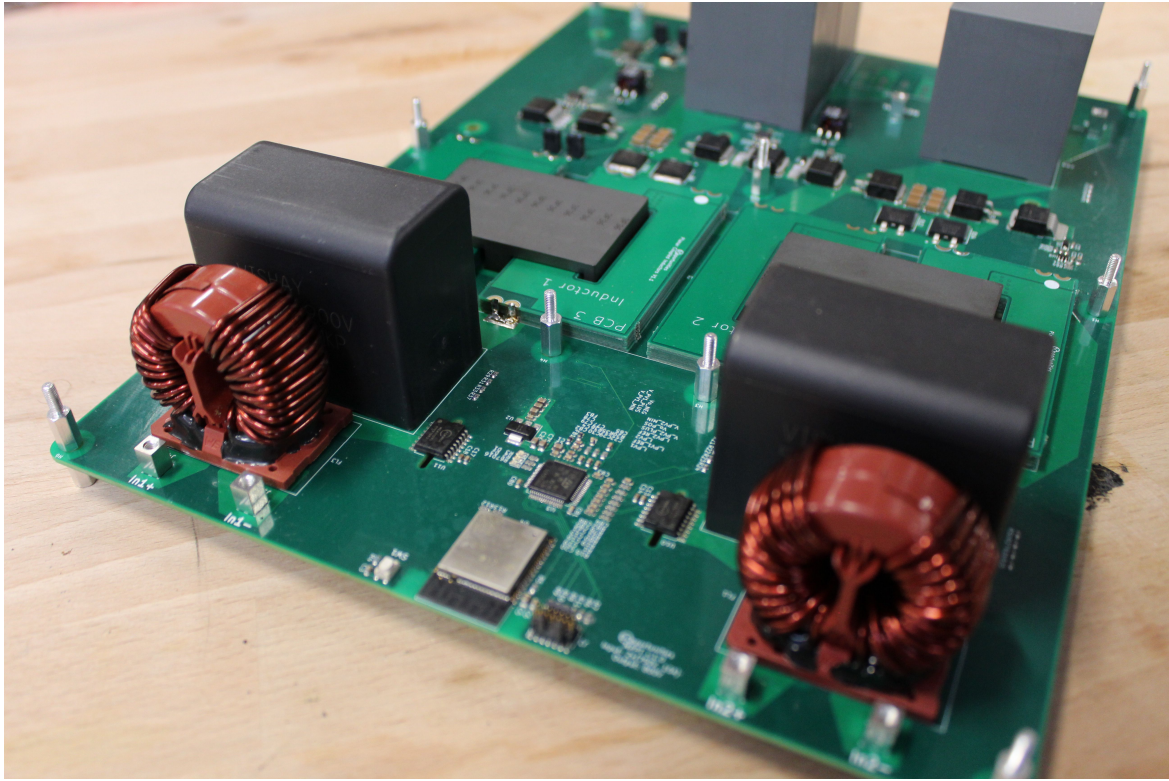


Figure A.3: The illustration of the MPPT Converter.

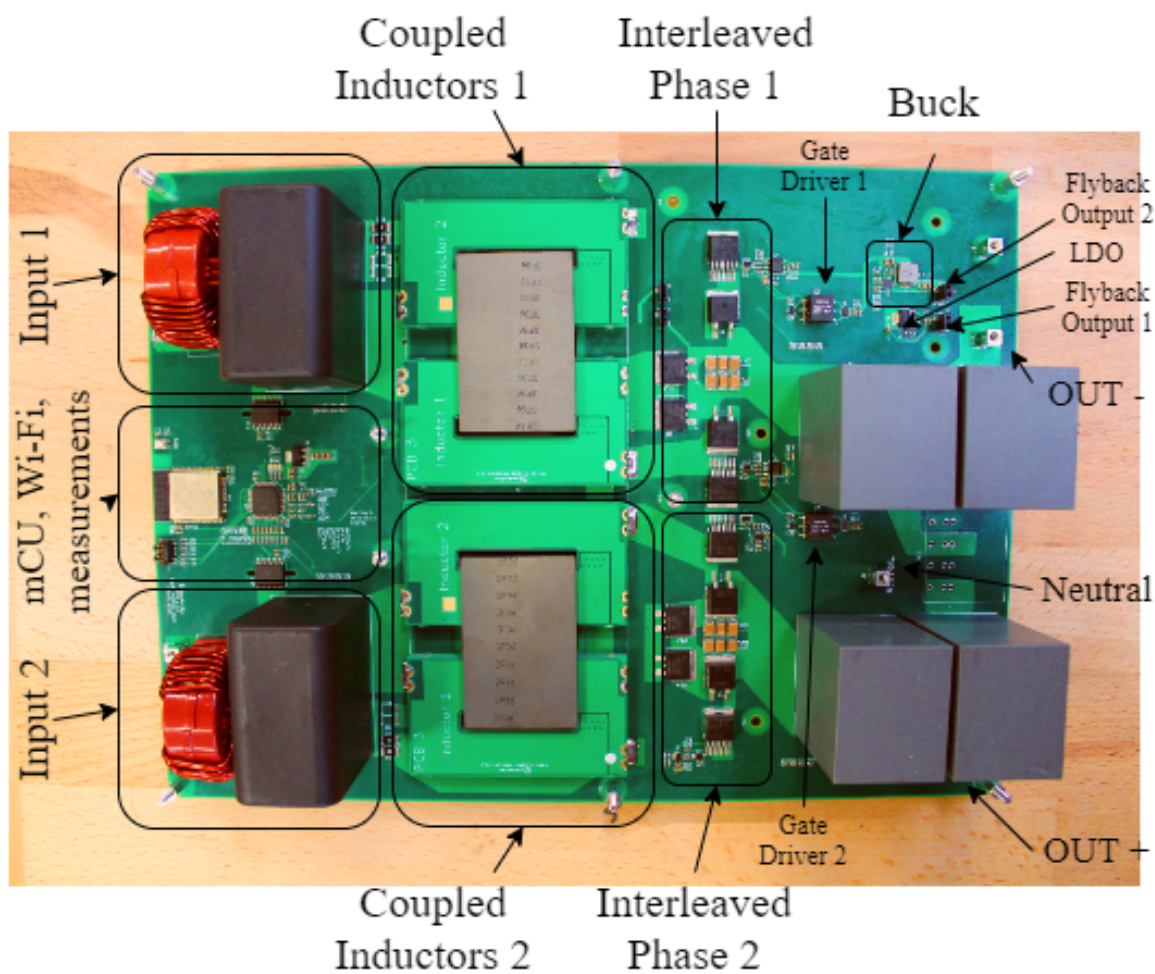


Figure A.4: The overview of the MPPT Converter.

### A.3 Flyback Converter v.1



Figure A.5: The illustration of the Flyback Converter v.1.

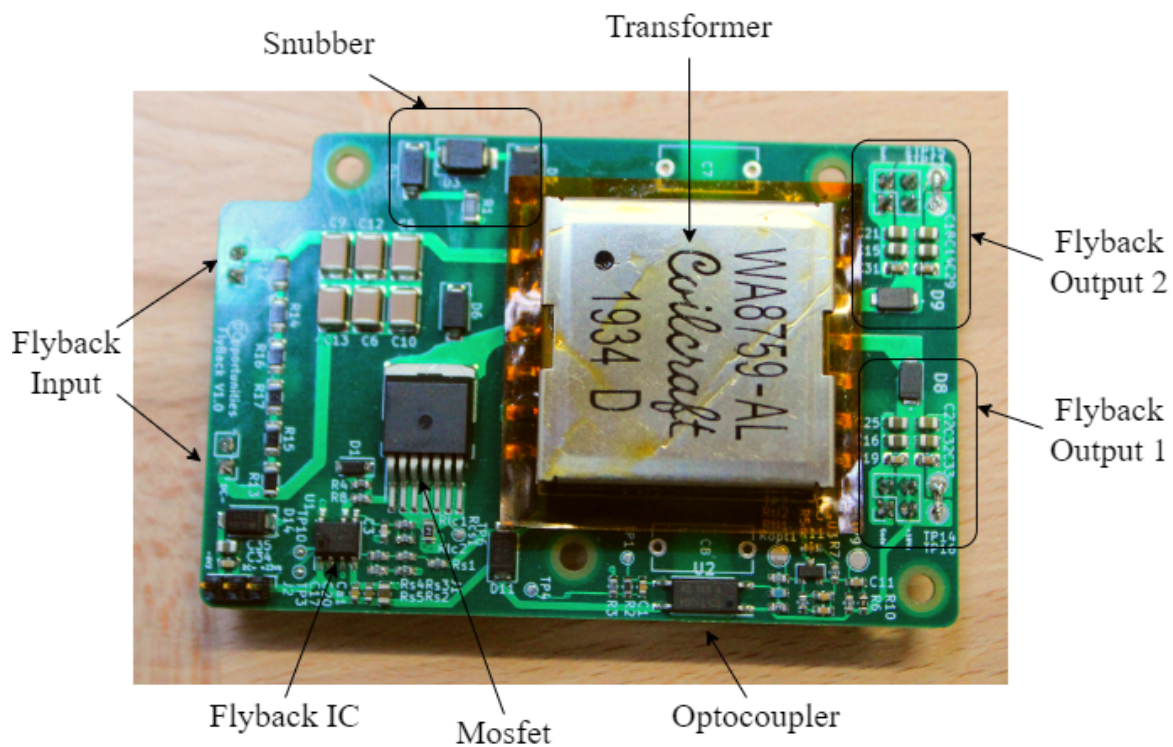


Figure A.6: The overview of the Flyback Converter v.1.

### A.4 Flyback Converter v.2



Figure A.7: The illustration of the Flyback Converter v.2.

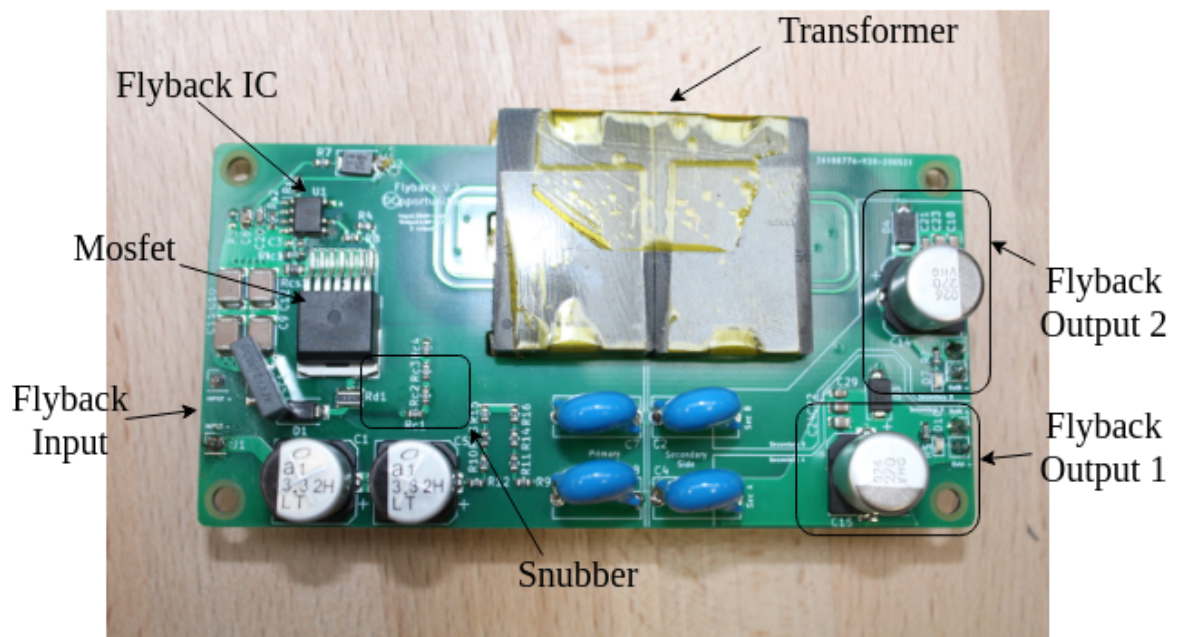


Figure A.8: The overview of the Flyback Converter v.2.

